

The Effect of Microstructure on the HEAC Behavior of Monel® K-500

A Thesis

Presented to
the faculty of the School of Engineering and Applied Science
University of Virginia

in partial fulfillment
of the requirements for the degree

Master of Science

by

Justin D. Dolph

May

2015

APPROVAL SHEET

The thesis
is submitted in partial fulfillment of the requirements
for the degree of
Master of Science


AUTHOR

The thesis has been read and approved by the examining committee:

Dr. James T. Burns

Advisor

Dr. Richard P. Gangloff

Dr. John R. Scully

Accepted for the School of Engineering and Applied Science:



Dean, School of Engineering and Applied Science

May
2015

The Effect of Microstructure on the HEAC Behavior of Monel[®] K-500

Abstract

Monel K-500 is a Ni-Cu-Al superalloy commonly used in marine applications due to its high corrosion resistance, high strength, and fracture toughness. This alloy is known to be susceptible to sub-critical hydrogen environment assisted cracking (HEAC) when immersed in seawater and exposed to cathodic polarizations. This has resulted in long time (10 year) service failures of Monel K-500 components during field use, suggesting significant sub-critical cracking. Previous work has quantitatively established the influence of cathodic polarization on the HEAC kinetics for a single lot of Monel K-500. The goal of this work is to determine the extent to which the HEAC behavior varies for Monel K-500 lots that meet alloy specification (QQ-N-286G); four materials were investigated and termed Tie Rod (TR) 1, TR 2, TR 3, and Allvac. TR 1, 2, and 3 were taken from engineering components from the field and Allvac is a virgin material lot.

First, fracture mechanics testing was performed to quantify the HEAC behavior of Monel K-500 from four different lots in various environmental conditions. Second, detailed characterization of the microstructure was completed to identify any lot-to-lot variations. Specifically, the grain size, yield strength, grain boundary impurity segregation, grain boundary character, crack deflection, and slip behavior were compared. Third, the quantitative HEAC parameters and microstructure characteristics from the previous two steps were coupled with results from a parallel study (executed by Prof. J.R. Scully at UVa) to quantify various aspects of the H-metal interaction. Finally, the micro-mechanical models were used to quantitatively evaluate how the observed changes in the microstructure may effect HEAC behavior.

Inert environment testing was completed and all materials showed similar behavior, assuring that differences in HEAC kinetics observed in charging environments are related to the material-hydrogen interaction. The HEAC kinetics for all materials were characterized at $-950\text{mV}_{\text{SCE}}$. No significant difference was observed in HEAC behavior between the four material lots at this potential. HEAC characterization in the near-threshold potential regime ($-850\text{mV}_{\text{SCE}}$) revealed slight variation in K_{TH} and da/dt_{II} between TR 1, TR 2, and TR 3. The Allvac material, on the other hand, did not suffer intergranular failure at this potential. Extensive

material characterization was focused on identifying the microstructural feature(s) present in Allvac, but not in TR 1, TR 2, or TR 3, that can explain the observed difference in HEAC susceptibility at $-850\text{mV}_{\text{SCE}}$.

It is concluded that the similarities in HEAC behavior across all four material lots observed at $-950\text{mV}_{\text{SCE}}$ is due to the high hydrogen concentrations achieved in the fracture process zone at such an aggressive potential. This was confirmed using micromechanical modeling. The small lot-to-lot differences in HEAC behavior observed between the tie rods at $-850\text{mV}_{\text{SCE}}$ appear to be due to variation in yield strength and grain size between the material lots. The variation in HEAC behavior between all material lots is observed to be independent of the fraction of low energy “special” boundaries and of the connectivity of high angle, random boundaries. No variation in crack deflection or slip behavior between the material lots was observed. The increased HEAC resistance in the Allvac material is shown to be a result of either (a) the decreased yield strength of Allvac and/or (b) less sulfur segregation at the grain boundaries in the Allvac material than in the three tie rods (supported by Auger depth profiling showing sulfur segregation in TR 2 not present in Allvac, a smaller bulk sulfur concentration in Allvac than in TR 1, TR 2, and TR 3, and by the smaller grain size of the Allvac material compared to the other material lots). Finally, micromechanical modeling is put forth that reasonably captures the effect of sulfur segregation on HEAC behavior in all four material lots.

Table of Contents

Abstract	i
List of Tables	vi
List of Figures	vii
1 Introduction	1
1.1 Introduction to Hydrogen Environment Assisted Cracking (HEAC)	1
1.2 HEAC Mechanism and Modeling	4
1.3 Metallurgy Effects on HEAC	7
1.3.1 Introduction to the Metallurgy of Monel K-500.....	8
1.3.2 Mechanical Properties	10
1.3.3 Grain Boundary Segregation	11
1.3.4 Hydrogen-Metal Interaction	12
1.3.5 Grain Boundary Character	12
1.3.5.1 Grain Boundary Misorientation	12
1.3.5.2 Grain Boundary Connectivity	14
1.3.5.3 Grain Size.....	15
1.4 Research Goals.....	18
2 Experimental Methods	18
2.1 Lot Materials	18
2.2 Fracture Mechanics Specimen Design	20
2.3 Fracture Mechanics Testing Protocol.....	21
2.4 Electrochemical Cell Design and the Electrochemical Environment	22
2.5 Crack Length Measurement	23
2.6 Fracture Mechanics Introduction	27
2.7 Fractography.....	29
2.8 Electron Backscatter Diffraction Mapping (EBSD).....	29

3	Results	33
3.1	Cracking Behavior.....	33
3.1.1	Inert Environment Testing.....	33
3.1.2	Cathodic Potential Testing.....	40
3.1.2.1	Testing in synthetic ASTM Ocean Water at -1000mV _{SCE}	40
3.1.2.2	Testing at -950mV _{SCE} Cathodic Polarization in 0.6M NaCl.....	43
3.1.2.3	Near-Threshold Cathodic Potential Testing.....	52
3.1.3	SSRT.....	59
3.2	Microstructure Characterization.....	63
3.2.1	Orientation Imaging Microscopy	63
3.2.2	Impurity Segregation at Grain Boundaries	66
3.2.3	Hydrogen Behavior in the Microstructure	67
4	Discussion	69
4.1	Pertinent HEAC Fracture Mechanics Testing Results	69
4.1.1	Effect of Calcareous Deposits on HEAC Kinetics	69
4.1.2	Lot-to-Lot HEAC Behavior Differences in Highly Cathodic Environment Testing	71
4.1.3	Lot-to-Lot HEAC Behavior Differences in Mildly Cathodic Environment Testing	73
4.2	Lot-to-lot Microstructure Variation and its Effect on HEAC Kinetics	73
4.2.1	Effect of Yield Strength	74
4.2.2	Effect of Grain Size	75
4.2.2.1	Effect of Crack Deflection	78
4.2.2.2	Effect of Slip Pile-up.....	80
4.2.3	Effect of Grain Boundary Connectivity.....	81
4.2.4	Effect of Impurities	88

4.2.4.1	Effect of Lot-to-Lot Variation in Sulfur Segregation on HEAC K_{TH}	90
5	Conclusions	93
6	References	97
A:	Testing Method Considerations	103
B:	Accelerated Side Cracking	122

List of Tables

Table 1.1: QQ-N-286G element composition standard for alloy Monel K-500.....	8
Table 2.1: Chemical composition analysis shows all materials satisfy the QQ-N-286 federal standard. The bulk compositions were determined by QUANT using ASTM E2594, E1019. The concentrations of S, P, Sn, and Pb were determined using trace element analysis by EAG using Glow Discharge Mass Spectrometry (GDMS).	19
Table 2.2: Average HRC material hardness measurements and the 95% confidence interval calculated from the measurements taken, measured yield strength, and the Ramberg-Osgood flow constants α and η . Yield strength and strengthening parameters were measured using tension testing specimens according to ASTM A370.....	20
Table 3.1: Average grain size for several heat treatments of aged Monel K-500 calculated from the IPF maps shown in Figure 3.17 according to ASTM E112-3. The margin of error for the 95% confidence interval in the grain diameter measurements is also given.	66
Table 4.1: (a) Typical D and S values taken from analysis of each material lot microstructure and (b) adjusted HEAC KTH for a deflected crack of angle θ_D in each material lot measured during fracture testing at -850mVSCE and -950mVSCE.	80
Table B.1: Testing matrix of SEN(T) specimens without painting the sides. An “X” denotes the test was run, an asterisk denotes the test was shortened due to the onset of accelerated side cracking. All tests run under cathodic protection were executed in 0.6M NaCl solution.	122
Table B.2: estimated crack growth rates for observed side cracking as well as the side crack initiation time and stress intensity for the main mode I crack at the start of side cracking.	129
Table B.3: Charging time to reach various hydrogen concentrations at a penetration depth of 87.23 μm predicted using Model A. A value of $5.0 \times 10^{-11} \text{ cm}^2/\text{s}$ was used for D_{eff}	131
Table B.4: The predicted hydrogen concentrations for penetration depths of 81 to 94 μm for a charging time of 105.685 hours using Model B. A value of $5.0 \times 10^{-11} \text{ cm}^2/\text{s}$ was used for D_{eff}	132
Table B.5: Comparison of hydrogen penetrations for two concentration levels predicted by Model A and Model B for a charging times of 105.685 hours and D_{eff} of $5.0 \times 10^{-11} \text{ cm}^2/\text{s}$	133

List of Figures

- Figure 1.1: The crack deflection geometry is described by the length of the straight segment S, the length of the deflected segment D, and the angle of deflection, θ_D 17
- Figure 2.1: Depiction of the bold surface covering used on most SEN(T) specimens during fracture testing. 23
- Figure 2.2: picture showing active and reference probe locations as well as the masking tape and lacquer covering used during fracture mechanics testing. 24
- Figure 2.3: da/dt vs elastic K for TR 1 at -950mVSCE executed with a slow K-rise of 0.33 MPa \sqrt{m} /hr. Shown are the initial measured da/dt data and the da/dt data after the shorting correction is applied. The linear log(da/dt) vs K fit used to implement the shorting correction is also shown. 27
- Figure 2.4: Example of an MCN (shown in red) with a 25 μ m grid spacing overlaid for connectivity analysis. More detail is given in Figure 4.6 and Section 4.2.3. 33
- Figure 3.1: Crack growth rate vs K_I for several aged Monel K-500 lots in inert environment (low humidity N₂). The tests were stressed at a constant dK/dt as shown in the legend. The vertical blue line separates two regimes of da/dt measurements. Left of the blue line, false da/dt data results from plasticity damage accruing at the crack tip. Right of the blue line, measured da/dt is shown for real crack growth due to microvoid coalescence 35
- Figure 3.2: SEM fractography (crack growth going left to right) of (a) Allvac Monel K-500 material lot (b) TR 1, (c) TR 2, (d) TR 3, (e) non-intergranular crack growth morphology in Allvac material and (f) non-intergranular crack morphology in TR 2 material during inert environment testing. 36
- Figure 3.3: Stable microvoid cracking region in Allvac Monel K-500 during inert environment testing executed at a dK/dt of 0.33 MPa \sqrt{m} 37
- Figure 3.4: (a) SEM fractography showing the matrix EDS locations used for reference comparisons to Figure 3.5 and (b) the EDS spectrum in Allvac material. Similar behavior is evident in the reference EDS measurements of the TR 2 matrix shown in (d), in the location shown in (c). 39
- Figure 3.5: (a) SEM fractography and (b) EDS spectrum showing titanium rich metal carbide located in the center of a microvoid in Allvac material. Similar behavior is evident in the

(c) SEM fractography and (d) EDS spectrum of similar carbides inside microvoids in TR 2 material. Identical microvoid morphology is evident in the other TR 1 and TR 3 as well..	40
Figure 3.6: Crack growth data of several tests carried out at -1000mV _{SCE} in ASTM artificial ocean water on the Allvac Monel K-500 material.	41
Figure 3.7: EDS analysis of calcium-rich (d, e, f, j, k, l) and magnesium-rich (g, h, i, m, n, o) deposits on SEN(T) specimen surfaces during testing of Allvac Monel K-500 material in ASTM artificial ocean water. A reference spectrum is shown in a, b, and c.	43
Figure 3.8: Results of fracture testing in 3.5 weight percent (0.6M) NaCl under a constant cathodic potential of -950mV _{SCE} . Loading was set to achieve a dK/dt rate of 0.33 MPa√m/hr. The dotted line shows the resolution limit associated with this ramp rate as measured in inert environment testing.	45
Figure 3.9: Macroscopic scale of (a) Allvac, (b) TR 1, (c) TR 2, and (d) TR 3 lots of Monel K-500 tested in 0.6M NaCl at -950mV _{SCE} . The crack growth occurred left to right, the area between the vertical blue lines is the crack growth that occurred during HEAC characterization testing.	48
Figure 3.10: Low magnification SEM images showing IG fracture due to HEAC in (a) Allvac, (b) TR 1, (c) TR 2, and (d) TR 3 material lots of Monel K-500 at -950mV _{SCE} in 0.6 M NaCl. Crack growth occurred left to right in all fractographs. On the TR 3 sample in Figure 3.10(d), corrosion product is present. (Footnote *)	50
Figure 3.11: SEM images showing slip lines on IG facets created during fracture testing of (a) Allvac, (b) TR 1, (c) TR 2, and (d) TR 3 material lots of Monel K-500 at -950mV _{SCE} in 0.6 M NaCl. Crack growth occurred left to right in all fractographs. Corrosion product is evident on Allvac and TR 3 fracture surfaces (Footnote *).	52
Figure 3.12: Results of fracture testing in 3.5 weight percent (0.6M) NaCl under a constant cathodic potential of -850mV _{SCE} . Loading was set to achieve a constant ramp rate of 0.33 MPa√m/hr. The dotted line shows the resolution limit associated with this ramp rate as measured in inert environment testing. The range of da/dt measured in inert (N ₂) environment testing is also indicated.	53
Figure 3.13: Macroscopic scale of (a) Allvac, (b) TR 1, (c) TR 2, and (d) TR 3 lots of Monel K-500 tested in 0.6M NaCl at -850mV _{SCE} . The crack growth occurred left to right, the area between the vertical blue lines is the crack growth that occurred during HEAC testing.	57

Figure 3.14: Crack growth data of Allvac and TR 2 material lots in inert environment and 0.6M NaCl at $-850\text{mV}_{\text{SCE}}$	58
Figure 3.15: Fractography of (a) Allvac, (b) TR 1, (c) TR 2, and (d) TR 3 at $-850\text{mV}_{\text{SCE}}$ in 0.6 M NaCl electrolyte revealing mixed IG/TG cracking associated with mild levels of HEAC in TR 1, TR 2, and TR 3 and ductile-like cracking in the Allvac material lot.....	59
Figure 3.16: SSRT fracture surfaces of aged Monel K-500 material lots in deaerated 0.6M NaCl; above images are (a) Allvac at $-850\text{mV}_{\text{SCE}}$, (b) TR 2 at $-850\text{mV}_{\text{SCE}}$, (c) Allvac at $-950\text{mV}_{\text{SCE}}$, (d) TR 2 at $-950\text{mV}_{\text{SCE}}$, (e) Allvac at $-1100\text{mV}_{\text{SCE}}$, (f) and TR 2 at $-1100\text{mV}_{\text{SCE}}$	63
Figure 3.17: Orientation imaging microscopy of the (a) Allvac, (b) TR 1, (c) TR 2, and (d) TR 3 material lots of aged Monel K-500.....	65
Figure 3.18: Grain boundary segregation data via Auger analysis on IG fracture surfaces of (a) Allvac and (b) TR 2 materials.....	67
Figure 4.1: SEM images for the fracture surface (top) and bold surfaces (bottom) of an Allvac SEN(T) specimen tested in ASTM artificial ocean water at $-1000\text{mV}_{\text{SCE}}$	70
Figure 4.2: Measured K_{TH} and model predicted (Equation 1) K_{TH} for HEAC versus applied potential for four aged Monel K-500 lots. The upward arrow indicates HEAC crack growth did not occur during testing.....	75
Figure 4.3: (a) K_{TH} and (b) da/dt_{II} at applied potentials of $-850\text{mV}_{\text{SCE}}$ and $-950\text{mV}_{\text{SCE}}$ and their relation to grain size.....	77
Figure 4.4: Grain boundary character of each material lot. Black lines are random, high angle boundaries. Red line are Sigma 3 boundaries.....	83
Figure 4.5: Map of $\Sigma 3$ boundaries in TR 1 used to calculate S_v with the test lines overlaid for analysis.....	84
Figure 4.6: Grain boundary character in each material lot studied given as (a) fraction of total grain boundary area per volume and (b) total grain boundary area per volume.....	85
Figure 4.7: The maximum connectivity network (MCN) of the random, high angle boundaries are shown in red for the (a) Allvac, (b) TR 1, (c) TR 2, and (d) TR 3 material lots. The images are overlaid with a $25\ \mu\text{m}$ grid, which was used to count N for the connectivity analysis.....	87

Figure 4.8: Atomic concentration depth profile on an IG facet of the TR 3 material lot showing extensive surface contamination, which hindered the investigation of impurity segregation along the grain boundaries in the material microstructures.	90
Figure 4.9: Measured K_{TH} and model predicted (Equation 22) K_{TH} for HEAC versus applied potential for four aged Monel K-500 lots accounting for yield strength and possible sulfur segregation differences. The upward arrow indicates HEAC crack growth did not occur during testing.	93
Figure A.1: da/dt vs plastic K for subsequent tests of Allvac at $-850mV_{SCE}$ executed with a slow K -rise ($0.33 MPa\sqrt{m/hr}$). Each test was run on the same sample.	105
Figure A.2: The fracture surface of multiple fracture mechanics tests run on a single Allvac SEN(T) sample in $0.6M NaCl$ at $-850mV_{SCE}$	105
Figure A.3: Fractography showing (a) macro-scale image and (b) ductile failure of Test 1 on Allvac at $-850mV_{SCE}$; also shown are (c) macro-scale and (d) high magnification images of intergranular failure of Test 2. The area outlined in red in (c) shows the IG failure that occurred during Test 3	106
Figure A.4: Schematic showing the difference in D_{SH} between a long crack and a short crack for the same applied K . The location of COD_{Max} , which is assumed to be constant, is shown by the vertical red line in the crack wake.	107
Figure A.5: Triangular model of the crack geometry, where $CMOD$ is the crack mouth opening displacement, Y is the distance between the fracture surfaces and is a function of the distance ahead of the crack tip, $d_{contact}$	108
Figure A.6: Measured da/dt data from two slow K -rise ($0.33 MPa\sqrt{m}$) tests done on two Allvac SEN(T) samples in $0.6 M NaCl$ at $-1000mV_{SCE}$ at short and long crack lengths (a) before and (b) after the applied linear shorting correction.	110
Figure A.7: D_{SH} calculated from crack depth and loading conditions during Test 1 (1.0 mm), Test 2 (2.9 mm), and Test 3 (7.2 mm) on one Allvac sample tested at $-850mV_{SCE}$, one Allvac sample tested at $-1000mV_{SCE}$ at short crack lengths (1.0 mm), and one Allvac sample tested at $-1000mV_{SCE}$ at long crack lengths (4.0 mm).	111
Figure A.8: Measured da/dt data from two slow K -rise ($1 MPa\sqrt{m}$) testing done in TR 3 material in inert N_2 environment on a short (1.1 mm) crack and a long (3.6 mm) crack. The residual humidity was below 2% for the test duration. The measured da/dt of tests on TR 1, TR 2,	

and Allvac materials when tested in inert environments at short crack lengths is also included.....	112
Figure A.9: Fractography of TR 3 in inert environment testing (a-c) at short crack lengths (1.1 mm) and (d-f) long crack length (3.6mm). The red circles in (c) point out embedded titanium carbides at the bottom of the microvoids.....	114
Figure A.10: (a) Plasticity at the crack tip calculated from loading conditions and crack length for two fracture mechanics tests on a single TR3 sample in inert, N ₂ environment and (b) its contribution to K _{Total}	116
Figure A.11: fracture surface for (a) short crack testing and (b) long crack testing of Allvac aged Monel K-500 material at -1000mV _{SCE} . The crack front after the precrack is outlined on both fracture surfaces.....	118
Figure A.12: C _{H-Diff} as a function of crack geometry at several applied potentials. The red dotted line indicates expected C _{H-Diff} values for a short crack length. The blue dotted line indicates expected C _{H-Diff} values at long crack lengths.....	120
Figure B.1: Fractography of a TR1 sample tested in 0.6M NaCl at -950mV _{SCE} . The area highlighted in yellow is where intergranular surface morphology is observed. The area in between the blue vertical lines signifies the section of normal intergranular crack growth.	123
Figure B.2: crack growth measurement of (a) TR 1 at -850mV _{SCE} for a painted and not painted specimen and (b) TR 1 at -950mV _{SCE} for a painted and not painted specimen. The non-painted specimens are truncated at the point where the side-cracking began.....	124
Figure B.3: Fractography of (a) TR2 at the crack tip near the center of the specimen width and near the specimen surface, (b) TR1, and (c) TR3 at -850mV _{SCE} with side masking implemented.....	126
B.4: C _{H-Diff} as a function of applied potential, E _{applied} established for the Allvac Monel K-500 material lot as a function of crack geometry described by x/G or x ² /G.....	128
Figure B.5: Hydrogen profiles from Dr. Crank's model for a semi-infinite plate with diffusion from both sides for an SEN(T) specimen 2.70 mm in thickness and (a) D _{eff} of 1.30x10 ⁻¹⁰ cm ² /s and (b) D _{eff} of 5.00x10 ⁻¹¹ cm ² /s.....	134
Figure B.6: (a) Equation B.4 previously fit to C _{H-Diff} and da/dt _{II} measurements on Allvac material with the estimated side crack growth kinetics shown by the blue rectangle and (b) the	

predicted range for da/dt using Equation B.4 for a small side crack is shown in the orange bracket while the red bracket shows the observed da/dt for the side cracks. Previously measured crack growth rates on the Allvac material is shown for reference [8]..... 138

Figure B.7: Proposed mechanism for the progression from (a) mode (I) crack growth dominated by constraint at the specimen center to (d) side cracking dominated by aggressive crack tip environment at the specimen edges. 141

Figure B.8: Hydrogen profile for the charged specimen if it were done at 20°C assuming D_{eff} values of (a) 1.3×10^{-10} cm²/s and (b) 5.0×10^{-11} cm²/s and at 70°C assuming D_{eff}^* values of (c) 1.39×10^{-9} cm²/s and (d) 5.35×10^{-10} cm²/s..... 143

Figure B.9: Fracture mechanics testing da/dt vs K_I results of uncharged Allvac and TR 2 samples and one precharged TR 1 sample at -1000mV_{SCE}..... 144

LIST OF SYMBOLS

AIDE	Adsorption-induced Dislocation Emission
EAC	Environment Assisted Cracking
FPZ	Fracture Process Zone
HEAC	Hydrogen Environment Assisted Cracking
HEDE	Hydrogen-enhanced Decohesion
HELP	Hydrogen-enhanced Localized Plasticity
IG	Intergranular
TG	Transgranular
γ'	Coherent Ni ₃ Al precipitates used for precipitate hardening in nickel superalloys
C_{H-Diff}	Concentration of hydrogen in the material in a stress-free zone
D_{eff}	Trap-affected diffusivity of hydrogen in the material

a	crack length
t	time
W	Specimen width
H	Hydrogen
σ_{YS}	Yield strength
ε	Strain
σ	Stress
K	Stress intensity
K_{TH}	Threshold stress Intensity for environmentally assisted cracking
da/dt	crack growth rate
da/dt _{II}	Stage-two crack growth rate
x_{crit}	Critical distance ahead of the crack tip for damage nucleation
C_{H-Crit}	Critical concentration of hydrogen necessary to cause failure at the grain boundary
$C_{H\sigma}$	Concentration of hydrogen in the fracture process zone at x_{crit}
C_L	Concentration of hydrogen in the lattice
σ_H	Hydrostatic stress
wppm	Part per million by weight
wt. pct.	weight percent
η_H	Hydrogen overpotential
EDS	Energy-Dispersive X-ray Spectroscopy

TDS Thermal Desorption Spectroscopy

OIM Orientation imaging microscopy

IPF Inverse Pole Figure

QQ-N-286G Federal specification for Monel K-500

1 Introduction

Monel K-500 is a Ni-Cu-Al superalloy commonly used in marine applications due to its high corrosion resistance, high strength, and fracture toughness. Long time (around 10 year) service failures of Monel K-500 components have been reported on North Sea oil and gas platforms, deep gas wells, and US Navy sea vessels [1-7]. In the deep gas wells, Monel K-500 components were exposed to hydrogen sulfide in sour gas. This led to failure due to sulfide stress cracking [4]. In cases of marine service failure, the Monel K-500 components were immersed in seawater and exposed to cathodic polarizations aimed at protecting adjacent carbon and low alloy steel structures. Subsequent failure analysis and previous laboratory testing suggests these failures were due to environment assisted cracking (EAC) [1, 2, 5-8]. This EAC failure morphology in Monel K-500 is largely intergranular (IG) with small amounts of transgranular (TG) [6, 8-11]. Prior work quantitatively established the influence of cathodic polarization on the EAC kinetics for a single lot of Monel K-500. This work coupled micromechanical damage models with a detailed empirical description of crack tip H-concentration to successfully interpret the observed dependence on cathodic polarizations pertinent to component service conditions [8, 12].

Since the QQ-N-286G specification governing Monel K-500 testing is a property driven document [13], the possibility of microstructure variation between lots of aged Monel K-500 exists. Slow sub-critical EAC cracking associated with long-life component failures and modern high fidelity quantitative characterization techniques that can to quantify crack growth kinetics suggest that fracture mechanics based modeling can be applied to enhance structural component design and management [8, 10, 14]. The current study will employ the methods developed and detailed in prior work [8, 12] to understand the degree of metallurgical differences present in material lots that satisfy the specification and how they influence the EAC susceptibility. The experimental and mechanistic understanding developed in this work will inform the extent to which metallurgical differences within QQ-N-286G specification need to be included in micro-mechanical and LEFM-based modeling.

1.1 Introduction to Hydrogen Environment Assisted Cracking (HEAC)

Previous studies of pure nickel and nickel alloys demonstrate they are susceptible to H-

embrittlement [8, 11, 15, 16]. Loading of high purity nickel specimens precharged with hydrogen via exposure to low pressure [15] or high pressure [16] hydrogen gas at elevated temperatures, demonstrated a transition from ductile microvoid coalescence to brittle IG cracking [15, 16]. This was attributed to segregation of internal hydrogen to the grain boundaries suggesting that hydrogen in the microstructure can cause a change in cracking behavior and fracture surface morphology. Fracture testing of nickel superalloy 718 (Ni-18Cr-18Fe-3Mo) single edge notched (SEN) specimens in chloride solution at potentials cathodic to the open circuit potential caused a transition in fracture morphology from microvoid cracking to a mixture of IG and TG cracking and decreased cracking threshold below what was measured in inert environment testing [11]. Furthermore, the amount of microvoid cracking and the threshold stress intensity continued to decrease with decreasing pH under otherwise constant conditions, signaling more severe embrittlement associated with environments that will produce higher levels of H [11].

Finally, previous fracture mechanics testing on a single material lot of Monel K-500 demonstrated exposure to 0.6M NaCl solution coupled with cathodic applied potentials below $-800 \text{ mV}_{\text{SCE}}$ causes IG cracking, decreased cracking thresholds, and increased crack growth kinetics compared to polarizations above $-750 \text{ mV}_{\text{SCE}}$ and inert environment testing where microvoid coalescence is observed [8]. Furthermore, increasingly cathodic potentials, lead to decreased threshold stress intensities and increased crack growth rates. The increasingly cathodic potentials were shown to correlate to higher concentrations of diffusible hydrogen at the crack tip, leading to increased local embrittlement [8]. In all systems studied and shown to be susceptible to HEAC, hydrogen embrittlement becomes more severe with (1) increased levels of H-charging or (2) in environments that will readily produce H at either the crack tip or the broad surface, and are characterized by an increased percentage of a brittle cracking morphology, lower cracking threshold, and /or increased crack growth rates compared to testing in the absence of hydrogen.

The effect of cathodic potential on the HEAC behavior in Monel K-500 in sodium chloride electrolyte has been established in the literature. Fracture mechanics testing of SEN samples showed that for increasingly cathodic levels of applied potential, the amount of IG cracking increases [8, 17, 18]. This behavior is consistent with the HEAC mechanism in that

increasingly cathodic potentials increase the over-potential for H production [8, 12, 19]. Thus, more hydrogen is available to migrate to the crack tip fracture process zone (FPZ), leading to increased hydrogen embrittlement [10]. This was demonstrated via an artificial crevice electrochemical analysis of Monel K-500, where increased diffusible H concentration (C_{H-Diff}) was measured at increasingly cathodic potentials for various crevice geometries [8]. The concentration of hydrogen at the maximum hydrostatic stress ahead of a crack tip, termed $C_{H\sigma}$, increases as C_{H-Diff} increases and intergranular fracture is enabled when $C_{H\sigma}$ reaches a critical concentration value, C_{H-Crit} [8, 10]. Therefore, there exists a threshold cathodic potential, termed the threshold potential, above which a sufficient C_{H-Diff} is not achieved to allow HEAC to occur. Previous work established the relationship between applied potential and hydrogen concentrations at the crack tip, quantified the threshold stress intensity for HEAC and da/dt_{II} , and accurately predicted the threshold potential for one material lot of Monel K-500, [8].

Of critical importance is the relative impact on the HEAC crack propagation from H production at the crack tip and at the bold surface away from the crack. Of these two hydrogen sources, the bold surfaces experience enhanced hydrogen production rates due to a larger over-potential compared to the crack tip [12]. The relative influence of each hydrogen source will depend on the testing duration, component/specimen geometry, hydrogen diffusivity, the potential and electrolyte of interest, and the loading rate. Prior research on Monel K-500 demonstrated the intensified, 3-dimensional stress state located at the crack tip dominates over the increased hydrogen production at bold surfaces during testing of 2.54 mm thick SEN(T) specimens, at loading rates of $0.33 \text{ MPa}\sqrt{\text{m}}$ and $1.1 \text{ MPa}\sqrt{\text{m}}$, in 0.6M NaCl, while being held at cathodic potentials between -700 mV_{SCE} and -1.1 mV_{SCE} [8]. They argued hydrogen produced at the bold surfaces had a secondary contribution to HEAC because of the long diffusion distance from the bold surface to the hydrogen damage sites in the FPZ (half the SEN(T) thickness). This was supported with hydrogen diffusion distance $2\sqrt{(D_{eff}t)}$ calculations, where D_{eff} is the effective diffusivity in Monel K-500 and t is time. Their analysis (using $1.3 \times 10^{-10} \text{ cm}^2/\text{s}$ as D_{eff}) suggested a maximum diffusion distance of 0.16 mm, much less than the half-thickness of the SEN(T) specimen [8]. In comparison, hydrogen produced at the crack must only diffuse to the location of maximum hydrostatic stress ahead of the crack tip (around $1 \mu\text{m}$) [8, 10]. In addition, SEM fractography of all IG surfaces showed uniform crack fronts with no enhanced growth near the bold surfaces, supporting the crack tip H uptake dominance over uptake at bold surfaces [8].

1.2 HEAC Mechanism and Modeling

Some proposed mechanisms for H-induced cracking include hydrogen-enhanced decohesion (HEDE), hydrogen-enhanced localized plasticity (HELP), and adsorption-induced dislocation emission (AIDE) [8, 10, 20, 21]. Other cracking mechanisms have been proposed, including cracking through/along a (Ni,Cu)_xH hydride which may form at 298 K with sufficiently high H concentrations (10 to 25 ppm) [20, 22, 23]. In this study, electron microscopy did not reveal the existence of a hydride phase or nano-scale cracking associated with cracking from these precipitates [8]. While the prominence of each damage mechanism in the HEAC of Monel K-500 remains controversial, recent TEM work supports a combination of HEDE and HELP [24]. Plastic damage accrued at the grain boundary leads to increased local stresses through work hardening. This in turns promotes H enrichment at the grain boundary due to increased H trapping in the dislocation substructure and H transport via dislocation motion [8, 24, 25]. The combination of increased stresses due to work hardening and increased H concentration (that decreases cohesion strength at the grain boundary) work together to promote intergranular fracture over transgranular fracture [8, 24, 25].

Two fracture mechanics parameters typically used to characterize HEAC of an alloy system are threshold stress intensity (K_{TH}) and stage-two cracking growth rate (da/dt_{II}). The K_{TH} is the stress intensities below which no HEAC is expected and the da/dt_{II} is an observed upper bound where further increases in K do not result in faster sub-critical crack growth. It has been proposed that this plateau is the result of a diffusion limitation of the hydrogen from the crack tip surface to the location of highest hydrostatic stress within the FPZ. Micromechanical models have been put forth to describe the K_{th} and da/dt_{II} based on the HEDE mechanism of final failure. Such models have been successfully applied to high strength steels and, more recently to Monel K-500 [8, 10, 26, 27].

The model of K_{TH} is shown in equation 1,

$$K_{TH} = \frac{1}{\beta'} \exp \left[\frac{(K_{IG} - \alpha C_{H\sigma})^2}{\alpha'' \sigma_{YS}} \right] \quad (1)$$

where β' [(MPa \sqrt{m})⁻¹] and α'' [MPa \cdot m] are constants from modeling of stresses at the crack tip, $C_{H\sigma}$ is the atom fraction concentration of hydrogen in front of the crack tip in the FPZ, K_{IG}

[MPa√m] is the intrinsic Griffith toughness (of the grain boundary for IG cracking), α [MPa√m(atom fraction of hydrogen)⁻¹] is a weighting factor defining how effective hydrogen is at lowering K_{IG} , and σ_{YS} [MPa] is the yield strength [26, 27]

For many high strength alloy-environment conditions, da/dt_{II} is rate limited by hydrogen diffusing to the FPZ approximately, a similar HEDE based micro-mechanical model has been proposed:

$$\left(\frac{da}{dt}\right)_{II} = \frac{4D_{eff}}{x_{crit}} \left(\operatorname{erf}^{-1} \left(1 - \frac{C_{H\sigma-crit}}{C_{H\sigma}} \right) \right)^2, \quad (2)$$

where D_{eff} is the effective diffusivity of hydrogen through the material and accounts for the presence of trap sites in the alloy, x_{crit} is critical distance in front of the crack tip where crack advance nucleates, and $C_{H\sigma-crit}$ is the critical concentration of hydrogen necessary to activate decohesion at x_{crit} [8, 10]. The parameter x_{crit} is on the order of one μm for many high strength alloys and is related to the position of maximum hydrostatic stress in front of the crack tip [8]. The two values chosen for D_{eff} for modeling in this project were $5.0 \times 10^{-11} \text{ cm}^2/\text{s}$ and $1.3 \times 10^{-10} \text{ cm}^2/\text{s}$ and were taken from previous hydrogen studies in Monel K-500 [12, 28]. Previous modeling using D_{eff} of $1.0 \times 10^{-10} \text{ cm}^2/\text{s}$ suggests an upper bound for da/dt_{II} of $1.7 \times 10^{-1} \mu\text{m}/\text{s}$, measured at a severe cathodic polarization (up to -1100 mV_{SCE}) where the ratio $C_{H\sigma-crit}/C_{H\sigma}$ is on the order of 0.1, and the inverse error function approaches 1. Further increases in cathodic potential were shown to only lead to small increases in da/dt_{II} [8].

The diffusible hydrogen concentration in the matrix, C_{H-Diff} , is the sum of hydrogen concentration in the lattice, C_L , and the concentration of reversibly trapped hydrogen at room temperature, C_{RT} [8, 12]. The hydrogen concentration at the point of maximum hydrostatic stress, $C_{H\sigma}$, in Equations 1 and 2 is related to C_{H-Diff} and can be calculated as

$$C_{H\sigma} = \left[C_L \frac{1 - C_{L\sigma}}{1 - C_L} \exp\left(\frac{\sigma_H V_H}{RT}\right) \right] \left[1 + \frac{1 - C_{RT}}{1 - C_L} \exp\left(\frac{E_B}{RT}\right) \right], \quad (3)$$

where $C_{L\sigma}$ is the hydrogen concentration in a stress enhanced lattice, E_B is the hydrogen trap binding energy of trap sites near the crack path, R is the gas constant, T is temperature, σ_H is the hydrostatic stress located a distance of x_{crit} ahead of the crack tip, and V_H is the partial molar

volume of hydrogen in a nickel lattice, $1.73 \text{ cm}^3/\text{mol H}$ [8]. The hydrostatic stress, σ_H is 3 to 20 times the yield strength of the alloy [29]. In this project, σ_H is assumed to be 12 times the yield strength, consistent with previous crack growth modeling and recent mechanism-based strain gradient plasticity modeling with an x_{crit} in the range of 100 to 1000 nm [8, 30]. The most influential trap sites in this alloy are γ' (Ni_3Al) precipitates, with a trap binding energy of $10.2 \text{ kJ/mol} \pm 4.4 \text{ kJ/mol}$ at a 95% confidence interval [12]. The volume fraction of γ' is expected to be 6-10 volume percent, and the precipitates are homogeneously distributed throughout the matrix [12, 31]. Metal carbides, such as TiC, are present in the material and have higher trap binding energies, but do not dominate hydrogen trapping behavior due to their low volume fraction, which was not resolvable in previous XRD analysis on aged Monel K-500 material [12]. In addition, the morphology and distribution of the metal carbides has been shown to be nearly independent of the heat treatment process [31]. Therefore, the consistency in titanium content found in all the material lots studied (shown in Table 2.1) justifies the assumption that there is a similar metal carbide volume fraction for all of the material lots.

Equation 3 can be simplified via three observations. First, previous researchers argue for potentials between $-1200 \text{ mV}_{\text{SCE}}$ and $-700 \text{ mV}_{\text{SCE}}$, the concentrations of hydrogen in the matrix, C_L and $C_{\text{H-Diff}}$, are much lower than one, justifying $1 - C_{\text{RT}} = 1 - C_L = 1$ [8]. This is supported by previously measured diffusible H atomic fractions in aged Monel K-500 at room temperature, which demonstrate C_L and C_{RT} are below 0.003 atomic fraction H[8]. Secondly, the binding energy of the reversible γ' trap site at room temperature is 10.2 kJ/mol . Inserting this into the binding energy term in Equation 3 demonstrates $\exp\left(\frac{E_B}{RT}\right)$ is much greater than 1. Therefore,

$1 + \frac{1 - C_{\text{RT}}}{1 - C_L} \exp\left(\frac{E_B}{RT}\right) \approx \frac{1 - C_{\text{RT}}}{1 - C_L} \exp\left(\frac{E_B}{RT}\right)$. These two simplifications lead to

$$C_{\text{H}\sigma} = \left[(1 - C_{L\sigma}) \exp\left(\frac{\sigma_H V_H}{RT}\right) \right] \left[C_L \exp\left(\frac{E_B}{RT}\right) \right]. \quad (4)$$

Third, for the potential range considered in this project, $C_{L\sigma}$ is between 0.05 and 0.10 atomic fraction H, making $1 - C_{L\sigma} \approx 1$ [8]. Also, by definition $C_{\text{H-Diff}}$ is equal to the second bracketed term in Equation 4. Therefore,

$$C_{H\sigma} = C_{H-Diff} \exp\left(\frac{\sigma_H V_H}{RT}\right). \quad (5)$$

The relationship between C_{H-Diff} and the overpotential for hydrogen production at the crack tip η_H was established using thermal desorption spectroscopy (TDS) on Allvac Monel K500 material to be

$$C_{H-Diff}(wppm) = -3.37 - 0.085 \eta_H (mV) [8]. \quad (6)$$

The relationship between C_{H-Diff} and applied potential was experimentally determined using artificial crevice testing coupled with the C_{H-Diff} vs η_H relationship to be

$$C_{H-Diff} = -52.5 - 0.0687 E_{app}, \quad (7)$$

where C_{H-Diff} is in wppm and E_{app} is the applied potential in mV_{SCE} [8]. Equation 7 allows for the determination of K_{TH} and da/dt_{II} as a function of applied potential. It also shows that C_{H-Diff} at the crack tip decreases as E_{app} increases and that hydrogen will enter the crack tip at all potentials less than -764mV_{SCE}. However, metallurgically different Monel K-500 lots may have a different relationship between C_{H-Diff} and E_{app} than what was determined for the Allvac material. This was demonstrated when similar analysis on another lot of Monel K-500 from Special Metals resulted in a C_{H-Diff} vs η_H relationship of

$$C_{H-Diff}(wppm) = -6.97 - 0.196 \eta_H (mV_{SCE}) [8]. \quad (8)$$

Comparison between Equation 6 and Equation 8 shows the lot from Special Metals adsorbs 2.3 times more hydrogen than the Allvac material at identical overpotentials. Such differences in the hydrogen uptake are related to metallurgical variation between the material lots [8]. This finding suggests a potentially significant effect of lot-to-lot variations in the H uptake, trapping, and/or diffusion behavior which may influence the HEAC behavior.

1.3 Metallurgy Effects on HEAC

The QQ-N-286G that governs production and purchase of age hardened Monel K-500 is a property driven specification; specifically, the material passes the specification as long as it exceeds the minimum required yield strength of 690 MPa, shows satisfactory corrosion resistance, and the alloy composition matches the specifications shown in Table 1.1 [13]. A

nominal final heat treatment for Monel K-500 components is: 16 hours at 866K, cool at 14K/hr to 755K, and air cool to room temperature [13], yielding γ' (coherent Ni₃Al) precipitates in a Ni-Cu solid solution matrix [31]. The γ' precipitates are coherent, spherical, and uniformly distributed throughout the matrix, allowing for significant precipitate strengthening [32]. The expected grain structure would be polycrystalline, isotropic grains with an average grain size on the order of tens of μm [12, 31].

Table 1.1: QQ-N-286G element composition standard for alloy Monel K-500.

Elements	Ni %	Cu %	Al %	Fe %	Mn %	Si %	Ti %	C %	Co %	S wppm	P wppm	Sn wppm	Pb wppm
QQ-N-286G Federal Spec.	>63.0	27.0-33.0	2.3-3.15	<2.0	<1.5	<0.5	0.35-0.85	<0.18	<0.25	<60	<200	<60	<60

While there is a suggested heat treatment included in the federal specification, any heat treatment may be used as long as the material passes the above criteria. As such, there is no explicit control over microstructure or higher-order materials properties (e.g. HEAC, fatigue, etc) to ensure consistency between material lots passing the QQ-N-286G federal specification.

The HEDE based models above provide a framework to quantitatively evaluate the effect of varying metallurgy between different lots of aged Monel K-500 on the HEAC behavior. From a damage mechanism perspective, such lot-to-lot difference could potentially influence hydrogen solubility, D_{eff} , crack tip stress behavior, K_{IG} , slip behavior, and the potency of hydrogen in embrittling the grain boundary. A difference in charging behavior has already been observed between two lots of Monel K-500 passing federal specification; specifically, different $C_{\text{H-Diff}}$ versus E_{app} relationships were observed [8, 12]. This implies that at the same applied potential each lot would contain a different $C_{\text{H-Diff}}$, which has been shown to affect $C_{\text{H}\sigma}$, K_{TH} , and da/dt_{II} through Equations 5, 1, and 2 respectively.

1.3.1 Introduction to the Metallurgy of Monel K-500

Nickel enjoy high solubility with other alloying elements, which has led to the development of several commercial Ni-based alloys. Copper and nickel share complete solid solubility while iron, cobalt, chromium, and molybdenum are soluble in nickel to various but significantly high concentrations [33]. The basic composition requirements for Monel K-500 are

given in Table 1.1. The FCC nickel (γ) matrix typically is strengthened by solution strengthening, carbide precipitation, and/or precipitation hardening. Solution strengthening in Monel K-500 is provided by iron and cobalt to some extent. Aluminum and titanium can also serve as solid solution strengtheners in nickel alloys, though in Monel K-500 these elements are precipitated out purposefully to form the γ' precipitate phase [32, 33]. Carbide precipitation is beneficial in that it can help control grain growth if they are precipitated along the grain boundaries [33]. The metal carbides present in Monel K-500 are large inclusions spread far apart from one another in the matrix, therefore do not provide significant strengthening to the alloy system [32]. Precipitation hardening leads to the most strengthening in the Monel K-500 alloy system [31-33]. Specifically, the γ' (Ni_3Al) intermetallic phase is precipitated extensively throughout the microstructure. This phase has an ordered $L1_2$ structure, with Ni on the faces and Al on the corners, and has a 1% or less mismatch with the nickel-copper matrix [33]. Alloy hardness and strength increase with volume of γ' and with γ' precipitate size. The particle size increases as a function of temperature and time, while the volume percent of γ' formed is a function of the amount of hardening elements present in the alloy composition, assuming the cooling rates are slow enough to allow complete precipitation of the γ' phase [33]. The primary γ' formers in Monel K-500 are aluminum and titanium.

Final heat treatment of Monel K-500 is focused on producing the appropriate γ' size distribution and percent volume to yield the desired characteristics. Desired γ' distributions are achieved by manipulating the alloy temperature within a range slightly below the γ' solvus, which is between 973 and 1023 K [31]. Two typical heat treatments to age harden Monel K-500 alloys are given in the federal QQ-N-286G standard. The first heat treatment is to heat the alloy to 866-880 K and hold that temperature for 8-16 hours, followed by a furnace cool to 755 K at 7-16 K/hr, and finished by air cooling [13]. The other heat treatment starts by holding at 866 K for 16 hours, followed by a furnace cool to 811 K and holding that temperature for 6 hours, followed by another furnace cool to 755 K with an 8 hour hold at that temperature, and ending with an air cool [13]. Often times the cooling rate, number of temperature holds, and holding temperatures are adjusted, yielding different γ' precipitate size distributions.

In nickel alloys, grain size is refined through cold working before annealing for the final age hardening heat treatment [33]. The variation in grain size evident in Figure 3.16 suggests

that the Allvac material was cold worked more than TR 1, TR 2, and TR 3 prior to aging. Usually, the grain diameter is kept on the order of tens of μm in diameter up to a maximum of 64 μm to yield a suitable combination of strength and ductility [33].

1.3.2 Mechanical Properties

Differences in crack tip hardening behavior would be reflected by differences in σ_{YS} and in the Ramberg-Osgood flow rule constants used in the J-integral analysis to account for specimen plasticity. Minimal influence of J-plastic was observed in severe cathodic polarization environments in prior testing on Monel K-500; however, plastic contributions would increase as cathodic polarization decreases, prior analysis showed up to a 25% increase above the elastic driving force for $K > 60 \text{ MPa}\sqrt{\text{m}}$ for testing in inert environment [8]. Differences in yield strength would lead to lot-to-lot variation in maximum stresses in the FPZ (σ_H). This would lead to different hydrogen concentrations, $C_{H\sigma}$, at the point of damage nucleation described by x_{crit} and affect the da/dt_{II} crack growth rates according to Equation 2 and lead to lot-to-lot variation in K_{TH} according to Equation 1. However, a direct comparison of K_{TH} is complicated due to the effects of other metallurgical differences possible between lots such as grain size, grain boundary character, and impurity segregation, which are known to also affect K_{TH} in nickel alloys and high strength steel [15, 16, 34-37]. Instead, differences in hardening would be better studied by tensile testing to directly measure the strain-load behavior to calculate σ_{YS} and the Ramberg-Osgood flow rule constants.

Differences in slip behavior between lots may also lead lot-to-lot variation in the measured HEAC kinetics. It has been suggested that the slip behavior is important and depends on the distribution and size of the γ' particles in the alloy [24, 32]. The γ' attributes will depend on the heat treatment and therefore may differ between material lots used in the field [31]. The slip behavior has been shown to correlate to slip traces on the grain boundary facets [24]. Therefore, large variation in γ' distribution would lead to obvious differences in slip trace height and/or density. A first order comparison of the slip behavior between material lots will be accomplished via SEM fractography to investigate any such obvious lot-to-lot variation in γ' distribution and size.

1.3.3 Grain Boundary Segregation

Segregation of certain elements such as S, P, Sn, or As are known to cause embrittlement at prior austenite grain boundaries in high strength steels and nickel based alloys [10, 34, 38]. The bulk sulfur content in Monel K-500 is kept very low to inhibit degradation of material properties. The federal specification calls for below 60 wppm sulfur concentration, though often sulfur concentrations below 10 to 20 wppm are achieved, as evident in Table 2.1 and the literature [8, 12, 39]. While sulfur segregation alone can lead to local embrittlement and IG fracture, simultaneous sulfur and hydrogen segregation may lead to the more damaging embrittlement than sulfur or hydrogen segregation alone, with the effects being at least additive [39-41]. This has been demonstrated in pure nickel, where an average atomic sulfur concentration at the grain boundary of $S/Ni = 0.10$ does not lead to IG fracture in the absence of hydrogen. However, coupling the same sulfur concentration with trace amounts of hydrogen leads to significant IG fracture [39]. Previous study on deuterium grain boundary segregation in pure Ni demonstrated S segregated on the grain boundaries increased the extent of deuterium segregation, suggesting a synergistic between S and H [42]. The presence of impurities such as S at the grain boundaries may lead to greater hydrogen concentrations by increasing the probability of hydrogen adsorption [43]. Other work on sulfur segregation in low strength Cr-Mo steel suggests co-segregation of sulfur and hydrogen leads to an increase in grain boundary embrittlement that was at least additive [44].

Differences in atomic grain boundary segregation, specifically sulfur and hydrogen, between material lots could detract from inherent strength of the boundary [4, 15, 28, 34, 38, 39]. From a modeling perspective the effect of this sulfur segregation on the inherent toughness of the GB would be captured by reducing K_{IG} via an additional term in Eqn. 21 that would describe the potency and concentration of sulfur at the grain boundary and potentially a higher potency of H (per atom fraction) if there is a more than additive effect of H and S segregation [8, 26]. An indirect measure of potential differences in grain boundary segregation can be achieved via trace elemental analysis that would unveil bulk impurity concentration differences between material lots. Extrapolation of such data to the degree of segregation is complicated by grain boundary orientation dependent binding energies and the inherent dependence of the density of segregation sites on the grain size. However, grain boundary segregation may be directly measured via Auger depth-analysis on grain boundary fracture surfaces.

1.3.4 Hydrogen-Metal Interaction

A companion study is investigating several aspects of the hydrogen-material interaction; including measuring the trap affected diffusivity, D_{eff} , the concentration of diffusible hydrogen, $C_{\text{H-Diff}}$, the total hydrogen concentration, $C_{\text{H-total}}$, and the trap binding energy of the γ' trap sites, E_B . The effect of D_{eff} is shown in Equation 2, da/dt_{II} is directly related to D_{eff} . The concentration of hydrogen in the FPZ, $C_{\text{H}\sigma}$, is directly related to $C_{\text{H-Diff}}$, as shown in Equation 5. Thus, an increase in $C_{\text{H-Diff}}$ would lead to an increase in da/dt at a constant applied K . Lot-to-lot variation in hydrogen trapping behavior, described by the trap binding energy, E_B , would also affect HEAC kinetics and is probed in a companion study. Previous study on one material lot of aged Monel K-500 asserts that the hydrogen trapping is dominated by the γ' precipitates [12]. The volume fraction of these precipitates are not expected to vary significantly between material lots passing federal specification [31]. Therefore, meaningful hydrogen trapping behavior variation is not likely, but still remains a possibility and warrants investigation.

The kinetics of the hydrogen evolution reaction (HER) are also to be measured for each material lot studied. Differences in HER kinetics may lead to different $C_{\text{H-Diff}}$ and $C_{\text{H-total}}$ between material lots, and contribute to different HEAC kinetics. Each of these factors may significantly contribute any lot-to-lot variation in the HEAC behavior and future work should consider these factors context of the mechanistic models as further data is available from this companion study.

1.3.5 Grain Boundary Character

The morphology of the HEAC cracking in Monel K-500 is largely intergranular, as such is it critical to investigate the character of the grain boundaries with respect to their (1) chemical composition, (2) the crystallographic orientation relationship between grains, and (3) grain size; each of which may be inter-related. Correlating changes in these characteristics with any lot-to-lot variations in HEAC behavior will provide insight into the governing mechanisms.

1.3.5.1 Grain Boundary Misorientation

Researchers have found that hydrogen embrittlement can be significantly reduced by reducing the fraction of random, high angle grain boundaries through the introduction of low energy grain boundaries termed “special” grain boundaries [16]. Special boundaries are low energy grain boundaries characterized by satisfactorily (below 15°) low misorientation angles

and/or coincident site lattice (CSL) boundaries. CSL boundaries are grain boundaries with particular angles of misorientation corresponding with a high fraction of common lattice points among to two grains at their boundary. There are several misorientation angles, θ , at which this occurs [45]. Each θ is coupled with a unique Σ number, corresponding to the reciprocal of the number of coincident lattice sites for that misorientation angle, and theoretical CSL orientations have been classified for cubic systems [46, 47]. For example, a θ of 60° corresponds to one third of the lattice points in two adjacent cubic systems aligning. Therefore, this boundary is termed a $\Sigma 3$ boundary [46]. Misorientation angles that do not relate to coincident lattice sites are termed random angle boundaries, which have been associated with higher grain boundary energies when θ is larger than 15° [37, 48]. The effect of grain boundary orientation on the HE behavior is controversial and has been attributed to either (1) increased H-concentrations associated with higher energy trap sites along random, high angle boundaries [48, 49], (2) high angle boundaries serving as preferential sites for impurity segregation [37, 39] and/or (3) increased hydrogen diffusion along high angle, random grain boundaries.

Regarding the first mechanism, random, high angle boundaries are known to have higher local stress, interfacial energy, and strain levels than “special” low energy grain boundaries due to the increased misorientation and dislocations necessary to accommodate such misorientations [37, 49]. The local stresses and dislocations along the grain boundary serve as trap sites and attract hydrogen to the boundary, leading to increased hydrogen concentrations along the interface compared to the grain interior [16, 37, 48, 49]. Jothi, Croft, and Brown investigated hydrogen concentration as a function of misorientation angle at the grain boundary via computational modeling on bi-crystal nickel. They found maximum hydrogen concentrations occurred on grain boundaries with misorientation angles between 15° and 45° [49]. Lower interfacial energy, which is associated with “special” boundaries, results in less hydrogen diffusing to those boundaries and makes them more resistant to HEAC than random, high angle boundaries [16, 37].

Regarding the second mechanism, grain boundary character affects impurity segregation by a similar mechanism, which has been shown to be lower at “special” grain boundaries than at random, high angle boundaries. This was demonstrated, when lower sulfur and bismuth segregate coverage in copper was measured at special grain boundaries compared to random

angle boundaries [50-52]. Sulfur is known to embrittle grain boundaries in nickel alloys [16, 39, 53], potentially increase the potency of hydrogen in embrittling the grain boundaries [39], and intrinsically decrease the ductility of the alloy [16, 54], justifying the desire to replace high energy random grain boundaries with low energy special boundaries through grain boundary engineering (GBE). Recently, resistance to sulfur segregation induced IG fracture was improved by Kobayashi et al. in high purity nickel using GBE to lower the connectivity of the random angle boundaries in the alloy [53]. A similar trend of decreased HEAC susceptibility with increasing fraction of special grain boundaries is expected in Monel K-500.

Regarding the third mechanism, recent research suggests that grain boundaries serve as preferential sites for both trapping and enhanced diffusion depending upon the character of the grain boundary [36, 49, 55]. Increasing hydrogen diffusion, D_{eff} , and solubility have been observed in nickel bicrystals and polycrystals with increasing fraction of random, high angle grain boundaries with misorientation angles larger than 15° [36, 49, 55]. In the same studies, low energy grain boundaries, consisting of low-angle grain boundaries and “special” boundaries (Σ 3- Σ 29), either have lower hydrogen solubility [49] or act as weaker traps at room temperature compared to random, high angle grain boundaries [55]. This leads to higher local hydrogen concentrations at the random, high angle boundaries than at the “special” boundaries. Thus, the HEAC resistance can be improved by lowering the fraction of susceptible random, high angle boundaries in the microstructure.

1.3.5.2 Grain Boundary Connectivity

Regardless of the controlling mechanism, there is significant evidence that increasing the number of special boundaries into a microstructure is an effective method of increasing HEAC resistance [16, 37, 49, 53, 54]. This GBE approach to improving HEAC behavior is predicated on reducing the availability of a susceptible grain boundary path for HEAC; specifically, eliminating or reducing the connected high angle grain boundary path. Previous researchers have found that HEAC susceptibility, as well as susceptibility to other intergranular phenomena, can be controlled by decreasing the percentage of random high angle boundaries in the system. [37, 54, 56]. For example, the intergranular stress corrosion cracking (IGSCC) of sensitized stainless steel is known to increase significantly when the percentage of random high angle boundaries exceeds 23% [37]. Similarly, Somerday et. al. showed that lowering the fraction of

random angle boundaries from 65% to 38% by number in Nickel 201 tensile specimens improved resistance to HEAC cracking. Specifically, the 38% random boundary specimens resulted in less IG cracking and higher fracture toughness though IG fracture was not completely prevented [16]. These works suggest that variation in grain boundary character between Monel K-500 lots passing the QQ-N-286G federal specification may result in different HEAC behavior between the material lots. Detailed quantification and analysis of the connectivity of the 3D grain boundary path ahead of an advancing crack is non-trivial, such efforts will be discussed further in the Discussion.

1.3.5.3 Grain Size

The effect of grain size on the HE behavior of various alloys has been reported. Threshold stress intensities for HEAC in a Fe-Ni-Co γ' strengthened superalloy, IN903, increased from 30 to 41 MPa \sqrt{m} as the grain size increased from 23 to 172 μm when stressed in high pressure hydrogen gas [35]. Subsequent testing on the same alloy in a separate study showed similar improvement in HEAC resistance with increasing grain size until an IG to TG transition was revealed as the grain size increased above 100 μm . The transition was caused by a change in cracking mechanism from HEAC to strain based slip band cracking [57]. A similar trend of increasing threshold stress intensity with increasing grain size was also seen in IN 718, a Ni-Fe-Cr alloy [11] and in pure nickel [36]. However, increasing grain size does not always correlate to improved HEAC resistance. For one, the threshold stress intensity was determined to be independent of grain size for a Fe-3.5Ni-1.7Cr-0.3C alloy for grain sizes ranging from 40 μm to 500 μm [34]. Understanding the effect of grain size on HEAC behavior is complicated due to the other material parameters being altered with changing grain size; specifically, the yield strength, impurity coverage on the grain boundaries, and projected crack path are likely affected by grain size in Monel K-500.

The yield strength relationship on grain size is described as:

$$\sigma_{YS} = M(\sigma_0 + k_y \cdot d^{-n}), \quad (9)$$

where M is the Taylor orientation factor, σ_0 is the friction stress, d is the grain diameter, k_y is the unpinning constant at the yield point, and n is a material dependent constant [58]. The parameters M, σ_0 , k_y , and n are material constants. Equation 9 was originally developed for mild steels, with $n= 1/2$, by Hall and Petch [59, 60]. This equation, called the “Hall-Petch equation”

has been used to characterize grain size and yield strength relationships for various alloys. Specifically, studies on nickel [61] and aged Monel K-400 (64.7 Ni 31.96 Cu 2.1 Fe 1.05 Mn, 0.11Si 0.05 Al 0.03C 0.003S wt. pct.) [58] determined n values of 1/2 and 1 respectively, suggesting slightly different yield strength versus grain size behavior between pure nickel and nickel superalloys. A general trend of increasing yield strength with decreasing grain size is expected in Monel K-500. Therefore, grain size variation, which is not accounted for in the QQ-N-286-G specification, would lead to variation in yield strength [13]. However, in this alloy, the yield strength is dependent upon the γ' size and distribution, making grain size a secondary effect on yield strength [32]. Still, grain size may lead to variation in HEAC threshold stress intensity by slightly influencing the yield strength.

Grain size may also affect the extent of impurity coverage along the grain boundaries. Impurities such as S [39], Sn [43], and Sb [43], which segregate to the grain boundaries during heat treatment, are known to increase the potency of hydrogen embrittlement. In the case of sulfur, this embrittlement is compounded since sulfur embrittles the grain boundaries itself [39]. A change in the grain size leads to a change in the area per volume of grain boundaries in the microstructure. Specifically, decreasing the grain size increases the area per volume of grain boundaries in the material. Prior researchers assert that, for a given quantity of impurity in the alloy, decreasing the grain size leads to lower impurity concentrations along the grain boundary due to the increased area per volume of grain boundaries [62, 63]. Thus, material lots with small grain size should be more resistant to HEAC than alloys with large grain size, assuming the bulk impurity concentrations between the alloys are the same. Such an occurrence would be reflected in the HEAC modeling. An increase in grain size may lead to an increase in impurity concentration at the grain boundary, thus the embrittling potency of hydrogen in the material; which would increase α (Eqn. 1). According to Equation 1, this would lead to a decrease in K_{TH} .

There may also be increasing crack deflection with increasing grain size, leading to decreased mechanical driving forces for crack extension. Crack deflection has been previously studied in aluminum alloys and nickel super alloys, where increased fatigue cracking thresholds and decreased crack growth rates in the slow cracking (less than 10^{-6} mm/ cycle) regime was attributed to increased crack deflection from mode I cracking associated with increasing grain size [64-67].

Assuming (1) the deflected crack trajectory is the same across the entire specimen thickness, (2) the crack driving force for each segment in the deflected crack is the weighted average of the effective stress intensity for the deflected segment, D , and the straight segment, S , and (3) the effects of prior deflections in crack path are negligible once the crack grows away from the points of prior deflections yields

$$K_{def} = K \frac{D \cos^2\left(\frac{\theta_D}{2}\right) + S}{D + S}, \quad (10)$$

where K_{def} is the effective linear elastic stress intensity for the deflected crack, K is the linear elastic stress intensity if the crack were straight and D , S , and θ_D are defined as in Figure 1.1 [66]. Typical D , S , and θ_D values in each material lot microstructure will be measured via EBSD mapping to analyze this potential effect on the measured HEAC threshold stress intensities. Large grain size could lead to high degrees of crack deflection for intergranular cracking associated with HEAC resulting in a tortuous crack path, while small grain size would imply little crack deflection, facilitating HEAC kinetics. In reality, the degree of crack deflection will be randomized across the entire specimen thickness. Thus, high degrees of crack deflection may be present at some areas of the crack front while little crack deflection may be occurring in other areas of the crack front. This means Equation 10 gives the maximum stress intensity reduction possible due to crack deflection.

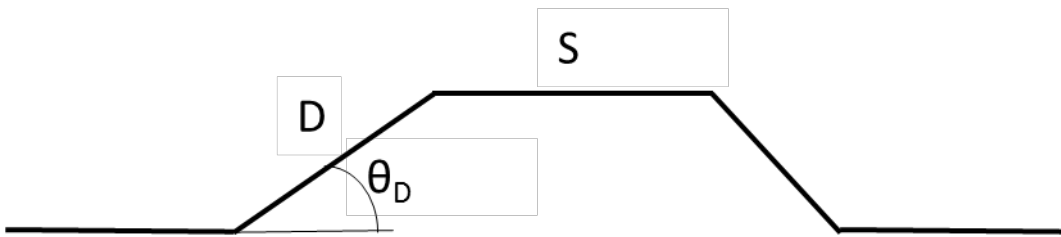


Figure 1.1: The crack deflection geometry is described by the length of the straight segment S , the length of the deflected segment D , and the angle of deflection, θ_D .

Understanding the relationship between grain size and HEAC susceptibility is complicated by the dependence of several intrinsic material properties (fraction of “special” boundaries, extent of impurity segregation to the grain boundaries, and crack path connectivity) and extrinsic influences on the mechanical driving force, each of which may alter the HEAC

behavior. A thorough comparison of microstructure parameters between different lots of Monel K-500 is needed to determine which metallurgy characteristics are important and the magnitude of their effect on HEAC kinetics in this alloy system.

1.4 Research Goals

The overarching aim of this research is to determine and understand the extent to which the HEAC behavior varies for Monel K-500 lots that meet specification QQ-N-286G. First, fracture mechanics testing will be performed to quantify the HEAC behavior of Monel K-500 from several different lots at various environmental conditions pertinent to component application environments. Second, detailed characterization of the microstructure will be performed to identify any lot-to-lot variations. Specifically, the grain boundary impurity segregation, grain boundary character, crack deflection, and slip behavior will be compared. Third, the quantitative HEAC parameters and microstructure characteristics from the previous two steps will be coupled with results from a parallel study (executed by Prof. J.R. Scully at UVa) to quantify various aspects of the H-metal interaction. Finally, the micro-mechanical models (Equations 1 and 2) will be used to quantitatively evaluate how the observed changes in the microstructure may relate to the resulting HEAC behavior.

2 Experimental Methods

2.1 Lot Materials

Selected materials were harvested from tie rods roughly one foot long and two inches wide, which did not fail during field use on U.S. Navy vessels; the components are termed Tie Rod 1 (TR 1), Tie Rod 2 (TR 2), and Tie Rod 3 (TR 3). Each tie rod experienced an unknown range of field exposure and varying (unknown) levels and durations of cathodic protection during service. A 15.9 mm diameter bar of virgin material was also acquired from ATI Allvac. Of note, the tie rod specimens were tested in the as-received conditions. A companion study suggests that H-charging that occurred during field service lead to a total internal H-concentration, $C_{H-total}$, on the order of 5 wppm which is similar to the expected levels of H-production at the testing conditions of interest, where previous work established 6 wppm at the crack tip at $-850mV_{SCE}$ for the Allvac material lot [8, 68]. The effects of the precharged hydrogen is discussed in more detail in Appendix B. However, it should be noted that fracture

testing in inert environment on as-received tie rod material did not show H-enhanced IG cracking due to the precharged H-content. Chemical composition analysis, shown in Table 2.1, determined the Allvac and TR 3 material lots satisfy the federal QQ-N-286 standard, while TR 1 and TR 2 contain more C than allowed by the specification. The bulk compositions were determined by QUANT using ASTM E2594, E1019. The concentrations of S, P, Sn, and Pb were determined using trace element analysis by EAG using Glow Discharge Mass Spectrometry (GDMS).

Table 2.1: Chemical composition analysis shows all materials satisfy the QQ-N-286 federal standard. The bulk compositions were determined by QUANT using ASTM E2594, E1019. The concentrations of S, P, Sn, and Pb were determined using trace element analysis by EAG using Glow Discharge Mass Spectrometry (GDMS).

Elements	Ni wt %	Cu wt %	Al wt %	Fe wt %	Mn wt %	Si wt %	Ti wt %	C wt %	Co wt %	S wppm	P wppm	Sn wppm	Pb wppm
Allvac	66.12	28.57	2.89	0.80	0.81	0.08	0.45	0.166	<0.01	1.6	92.0	2.4	2.1
TR #1	65.55	29.18	2.86	0.93	0.67	0.044	0.47	0.22	0.011	3.1	55.0	1.2	2.4
TR #2	64.66	30.15	2.73	0.69	0.73	0.094	0.45	0.20	0.044	11.0	71.0	6.9	2.5
TR #3	64.88	30.48	2.64	0.65	0.74	0.086	0.46	0.137	0.045	12.0	74.0	6.8	2.4
QQ-N-286G Federal Spec.	>63.0	27.0- 33.0	2.3- 3.15	<2.0	<1.5	<0.5	0.35- 0.85	<0.18	<0.25	<60	<200	<60	<60

The Allvac material lot was hot finished and age hardened as follows: 16 hours at 866K, cool at 14K/hr to 755K, and air cool to room temperature [8, 13]. The exact heat treatment of TR 1, TR 2, and TR 3 are unknown but they are solution heat treated and aged. The Rockwell C hardness (HRC) values are shown in Table 2.2; the higher HRC correlates to higher yield strengths and likely reflects changes in the γ' character. The strengthening behavior of each material can be described by Ramberg-Osgood equation:

$$\varepsilon_T = \frac{\sigma_T}{E} + \alpha \frac{\sigma_0}{E} \left(\frac{\sigma_T}{\sigma_0} \right)^n, \quad (11)$$

where, σ_T is the applied stress, E is Young's Modulus, σ_o is the yield strength, ϵ_T is the applied strain, α is a dimensionless constant, and n is the strain-hardening exponent [69]. Baseline material properties were previously established for Allvac: Ramberg-Osgood constants of $\alpha = 0.39$ and $\eta = 20$, Young's Modulus (E) of 185,700 MPa, and yield strength ($\sigma_o = \sigma_{YS}$) of 786 MPa (for a 0.2 percent offset) [8]. (These constants are assumed to be the same for TR 1, TR 2, and TR 3 during the J-integral analysis since these data were not available at the time of the testing. Little influence is expected for severe cathodic polarizations where minimal influence of J-plastic was observed in prior testing Monel K-500. Errors would increase for inert testing where prior work showed up to a 25% increase about the elastic driving force for $K > 60 \text{ MPa}\sqrt{\text{m}}$ [8]). The strengthening behavior of TR 1, TR 2, and TR 3 are given in Table 2.2.

Table 2.2: Average HRC material hardness measurements and the 95% confidence interval calculated from the measurements taken, measured yield strength, and the Ramberg-Osgood flow constants α and η . Yield strength and strengthening parameters were measured using tension testing specimens according to ASTM A370.

	Allvac ATI	TR #1	TR #2	TR #3
Average Hardness (HRC)	(32±0.5)	[35.4±0.5]	(34.1±0.4)	(31.83±0.5)
Yield Strength (MPa)	786	898	795	793
α	0.39	0.39	0.39	0.37
η	20	18	22	23

2.2 Fracture Mechanics Specimen Design

Single edge micro notch tensile (SENT) specimens were excised from the Allvac round bar and TR 1, TR 2, and TR 3 marine components. The gauge section of the Allvac samples measured 10.6 mm in width (W), and 2.54 mm in thickness (t). The TR 1, TR 2, and TR 3 SEN(T) specimens were 12.5 mm in width and 2.54 mm in thickness to maximize the number of specimens available from the stock components. Mode I loading was done in the longitudinal direction of the round rod/tie rod and cracking was done in the radial/transverse direction. An initial notch of $200 \pm 10 \mu\text{m}$ was placed at the halfway point in the test gauge portion of the SEN(T) specimens using electrical discharge machining (EDM).

2.3 Fracture Mechanics Testing Protocol

Fracture mechanics testing was done using MTS hydraulic test frames coupled with computer software allowing real-time crack length measurements (described below). Clevis grips allows free rotation of the SEN specimen, complying with boundary conditions assumed in the K solution calculated from the physical crack length [70]. The system is designed to allow for in-situ K analysis, permitting the use of stress-intensity controlled testing.

A fatigue precrack regime was selected to provide a sharp crack suitable for testing as the EDM notch has a round, wide edge. The precrack regime used involves two stages. The goal of the first stage is to initiate a crack at the base of the EDM notch, nominally 0.2 mm in length. A constant maximum load of 12.455 kN and minimum load of 1.2455 kN (correlating to a K_{max} of 12.7 MPa \sqrt{m} and an R of 0.1) were applied at a frequency of 0.1 Hz used to initiate the crack and extend the crack to a total depth of 0.4 mm, including the EDM notch. The constant load method results in a K-rise to 0.4mm, ending in a maximum ΔK (the difference between the maximum K, K_{max} , and minimum K, K_{min}) of around 13.5 MPa \sqrt{m} , where K_{max} was 15 MPa \sqrt{m} . This method was chosen to speed up the precrack procedure. The second stage is a K-shed to a K_{max} of 13.5MPa \sqrt{m} at 1.00 mm. Throughout the precrack an R value of 0.1 was used, resulting in a final ΔK of 12.15 MPa \sqrt{m} . At this ΔK , very slow cracking on the order of 10^{-9} to 10^{-8} mm/cycle was normally reached. Also, this K_{max} was below expected HEAC threshold stress intensity values of 15 to 20 MPa \sqrt{m} established in previous work on the Allvac material lot [8].

One critical part of the final K-shed protocol is to ensure the change in K_{max} occurs over a sufficient change in crack lengths so that load-history effects do not affect the measured crack growth during the fracture mechanics testing. A fatigue protocol can be described using

$$K_{max,final} = K_{max,initial} \left(\exp \left(C(a_{final} - a_{initial}) \right) \right), \quad (12)$$

where, C is a constant that describes the change in K_{max} over a given period of crack growth. Current efforts mimicked previous testing on Monel K-500 by using a C of -0.4 mm^{-1} [8].

Fracture mechanics testing was done in K-control at a K ramp rate of 0.33 MPa \sqrt{m} /hr. During a typical test, this corresponds to a loading rate of 5×10^{-5} kN/s and a grip velocity of 2×10^{-6} mm/s before cracking begins. Once significant crack rates are achieved, the required load

to ensure a constant K ramp rate will no longer be linear since the load required to achieve a desired K decreases with increasing crack length. Through in-situ crack length measurements and applied stress intensity calculation the loading system changes the loading rate every five seconds to achieve the desired K ramp rate. Three tests during inert environment testing were run at $1.00 \text{ MPa}\sqrt{\text{m/hr}}$ to limit test duration. All tests done in hydrogen charging environments were carried out at $0.33 \text{ MPa}\sqrt{\text{m/hr}}$.

2.4 Electrochemical Cell Design and the Electrochemical Environment

The electrochemical environment was maintained within a cylindrical, Plexiglas, three electrode cell attached about the SEN(T) specimen designed to allow simultaneous cathodic polarization in 0.6M NaCl and tensile loading. Polarization was achieved via a potentiostat, cylindrical platinum counter electrode surround the SEN(T) specimen, and standard calomel electrode (SCE). A floating ground potentiostat was used as the specimens were grounded through the grips. Most SEN(T) specimens were covered using 470 electroplating tape, a 3M[®] product, and a butyl rubber compound (Micro XP-2000 Stop-off Lacquer) as shown in Figure 2.1 to prevent transition away from mode I cracking during testing, discussed further in Appendix B. A 1mmx8mm window, corresponding to an a/W of around 0.7, was left open along the projected crack path to avoid changing crack tip chemistry during testing.

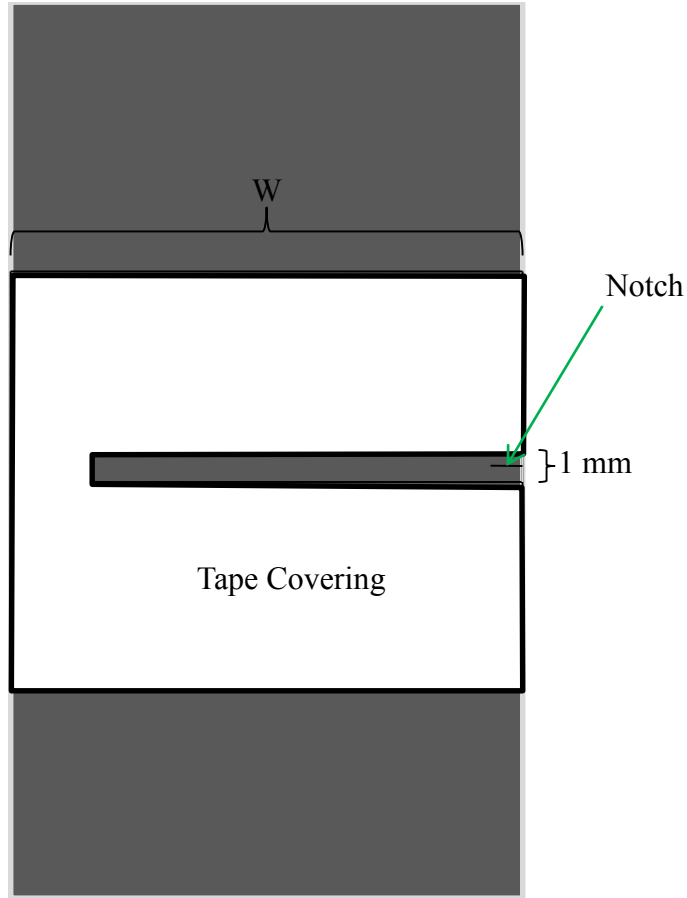


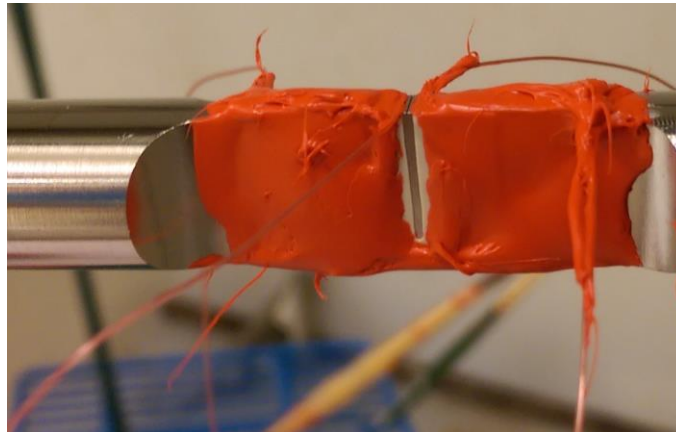
Figure 2.1: Depiction of the bold surface covering used on most SEN(T) specimens during fracture testing.

The majority of tests were executed in 0.6M NaCl, with a pH of 6.0. During a typical test, the pH at would increase up to between 6.2 and 6.5, with greater pH increases coinciding with increasingly cathodic applied potentials. One test was executed in ASTM artificial ocean water to investigate the effects of calcareous deposits and heavy metal constituents in the solution on HEAC kinetics for Monel K-500.

2.5 Crack Length Measurement

The crack length, a , was measured in situ via the direct current electrical potential difference (dcPD) test method [8, 14, 71, 72]. A constant direct current of 4.000 plus/minus 0.005 A was used to create a potential difference across the crack opening, which is measured by two Alume^l® wire probes placed within 0.5 mm on either side of the crack mouth [14]. This potential is normalized to account for resistance changes due to effects such as temperature

change via a reference probe, which is spaced as far apart as the electrochemical cell allows, 28 mm apart. As shown in Figure 2.2, the inner probes, located closest to the crack mouth, and reference probes, located at either end of the specimen test gauge, are covered by lacquer to provide stability and prevent detachment of the probe wires during testing.



(a)



(b)

Figure 2.2: picture showing active and reference probe locations as well as the masking tape and lacquer covering used during fracture mechanics testing.

The initial potential prior to testing is normalized to a reference crack length, normally chosen to be the optically measured notch depth achieved during EDM notching prior to fatigue precracking. The potential is measured every 5 seconds and converted to crack length in mm via Johnson's equation [71]. For each dcPD measurement, 50 potentials are recorded, the current polarity is then inverted, followed by 50 additional potential readings. These readings are then averaged and that average is reported. The entire process takes 2.5 seconds. These parameters were determined using the Edisonian approach to provide optimal crack length resolution and

minimum data acquisition times. The resolution of the measured potential was $0.1\mu\text{V}$ corresponding to $0.5\mu\text{m}$ of crack extension. Since the exact length of the EDM notch cannot be measured sufficiently until the fracture surface is created, the reference crack length used to calibrate the dcPD system during testing is slightly incorrect, on the order of 0.1 mm . This is overcome via a post-test correction, where a new reference potential associated with the crack length at the end of the precrack measured from the fracture surface via SEM image analysis. This is very reliable since the fracture surface morphology created during fatigue crack growth looks very different than the IG morphology associated with HEAC. With the improved reference potential and crack length, dcPD crack length measurements and those crack length measurements taken from SEM fractography agreed within 5 percent of the visual crack length measurement at the end of the test, where the maximum difference in crack length measurements would occur.

The crack growth rate (da/dt) was calculated for a given time, t by determining the slope of the $a-t$ data. A second order polynomial was fitted to 7 data points centered at the time of interest. The slope of the tangent line is then da/dt . This process is repeated for every $a-t$ data point and then averaged, yielding reliable da/dt data throughout the test entirety. The da/dt measurement resolution was hampered by two issues unique to this alloy and its environment. First, localized plasticity at the crack tip resulted in measured dcPD increases during periods of non-crack growth. As detailed in a subsequent section and in prior work this plasticity served as the basis for establishing a K dependent resolution limit below which potential drop due to plasticity cannot be distinguished from real crack advance; this resolution limit is reported on each data plot [8]. Secondly, when cathodically polarized, the insulating surface film is not stable. In this situation, crack wake contact can lead to electrical shorting, thus skewing the relationship between the measured potential and the true crack length [8]. For example, during the initial stages of the test the crack wake contact decreases as the crack opening increases with increasing load, this results in an increase in dcPD measurements despite there being no true crack growth.

The results of a single experiment on TR 1 at an aggressive cathodic potential of $-950\text{mV}_{\text{SCE}}$ are shown in Figure 2.3. The initial decrease in da/dt with rising K in the $10\text{ MPa}\sqrt{\text{m}}$ to $13\text{ MPa}\sqrt{\text{m}}$ regime is the result of decreasing electrical contact between fracture surfaces as

the K rises, which leads to increasing voltage across the crack opening. This phenomenon is termed “shorting” and has been reported and discussed in prior work [8, 14]. The decreasing $\log(da/dt)$ data acquired during significant crack wake contact were fit as a linear function of K using data analysis software, and subtracted from the measured da/dt . The resulting modified da/dt shown in Figure 2.3 is now associated with real crack growth and increased electrical resistance of the crack, which increases as the plasticity damage at the crack tip increases (previously mentioned). Before K_{TH} , the corrected da/dt conforms to expected HEAC behavior. Similar corrections were applied whenever shorting was observed unless otherwise specified. The shorting is discussed further in Appendix A.

The da/dt_{II} rates are defined as the crack growth rate where the kinetics reach a plateau, where crack growth is semi-constant with rising K . The crack growth data in Figure 3.7 and Figure 3.11 show the onset of da/dt_{II} crack growth occurs before a K of $60 \text{ MPa}\sqrt{\text{m}}$. Thus, the measured da/dt at this K value is da/dt_{II} . K_{TH} is the minimum stress intensity sufficient to cause HEAC cracking. This is the point at which the measured da/dt exceeds the resolution limit (defined in a later section), allowing K_{TH} values to be read directly off the da/dt vs K scatter plots.

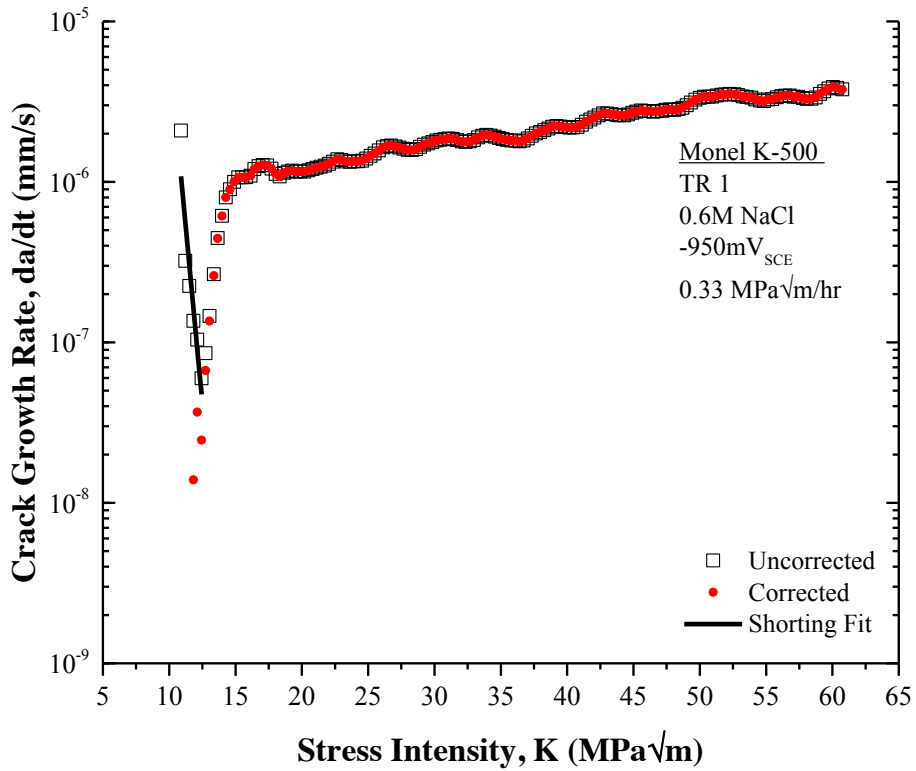


Figure 2.3: da/dt vs elastic K for TR 1 at -950mV_{SCE} executed with a slow K-rise of 0.33 MPa√m/hr. Shown are the initial measured da/dt data and the da/dt data after the shorting correction is applied. The linear log(da/dt) vs K fit used to implement the shorting correction is also shown.

2.6 Fracture Mechanics Introduction

The mechanical driving force for crack extension is given by the stress intensity factor, K [69]. The mathematical solution for elastic stress intensity during Mode I loading of an SEN(T) specimen as a function of load and physical crack length is given as

$$K = \sigma \sqrt{\pi a} F\left(\frac{a}{W}\right) \quad (13)$$

where a is the crack length, σ is the applied stress away from the crack tip, and $F(a/W)$ is a function of crack length and specimen width accounting for the geometric effects of the crack presence on the stress field [70]. A numerical solution for $F(a/W)$ for SEN(T) specimens under

tensile loading is [70]

$$F\left(\frac{a}{W}\right) = \sqrt{\frac{2W}{\pi a} \tan\left(\frac{\pi a}{2W}\right)} \frac{0.752 + 2.02\left(\frac{a}{W}\right) + 0.37\left(1 - \sin\left(\frac{\pi a}{2W}\right)\right)^3}{\cos\left(\frac{\pi a}{2W}\right)}. \quad (14)$$

The load is directly measured using a calibrated load cell and the crack length is measured in real time using the dcPD method. Computer software allows for real-time stress intensity control (K-control) via a load-K calculation feedback loop executed every five seconds.

While the test was controlled using the elastic parameters only, post-test analysis was performed to account for specimen plasticity. The total elastic plastic driving force, K_I , is calculated using the equation

$$K_J = \sqrt{(J_{Elastic} + J_{Plastic})E'} = \sqrt{\left(\frac{K^2}{E} + J_{Plastic}\right)E'}, \quad (15)$$

where E' is equal to E in plane stress condition and $E/(1-\nu^2)$ in plane strain conditions and ν is Poisson's ratio [17]. Testing condition imply plane strain, supported by previous three-dimensional finite element analysis and studies on high strength steels, aluminum alloys, and nickel alloys using similar SEN specimen designs [8, 10, 73, 74]. The plastic contribution to J at the crack tip is

$$J_{Plastic} = \frac{\alpha \sigma_0^2}{E} a \frac{(W-a)}{W} h_1(n, a/W) \left(\frac{P}{P_0}\right)^{n+1}, \quad (16)$$

where h_1 is a geometric and hardening function, P is load, α and n are the afore-mentioned Ramberg-Osgood flow rule constants and were determined to be 0.39 and 20 respectively for the Allvac material, and P_0 is the limit load for net plastic deformation in the remaining ligament [75]. The h_1 for a free-rotating SEN specimen was defined using a sixth order polynomial fit to discrete values, excluding negative h_1 values [8, 75]. Since h_1 and $J_{Plastic}$ are functions of α and n , $J_{Plastic}$ may differ lot-to-lot if the Ramberg-Osgood hardening behavior changes lot-to-lot; this subtlety is not captured in the current analysis but is expected to be a secondary effect. P_0 is

given by

$$P_0 = \beta \left(\sqrt{1 + \left(\frac{a}{W-a} \right)^2} - \left(\frac{a}{W-a} \right) \right) (W-a) B \sigma_0, \quad (17)$$

where β is 1.455 for plane strain and B is thickness [69].

2.7 Fractography

Fractography was acquired with an FEI Quanta 650 Scanning Electron Microscope and an FEI Quanta 200 Scanning Electron Microscope (SEM). The FEI Quanta 650 SEM Handbook claims a lateral resolution ranging from 3.0 to 10.0 nm depending on viewing conditions for the FEI Quanta 650 SEM, and is similar for the FEI Quanta 200 SEM [76-78]. The fracture surfaces were removed from the SEN specimens after breakage occurred and rinsed with deionized water to remove any chlorides. The flat gauge section of the SEN(T) specimen that now contains the fracture surface was then removed from the round, threaded portion to allow for easy storage and sample mounting in the SEM. Both the fracture surfaces and remaining threaded stubs were sonicated in acetone and methanol for five to ten minutes to remove cutting oil and stored in a desiccator.

2.8 Electron Backscatter Diffraction Mapping (EBSD)

Orientation imaging microscopy (OIM) was completed using the electron backscatter diffraction (EBSD) capabilities of the FEI Quanta 650 SEM at 30 kV with a 5 nA probe current. The samples for EBSD were extracted from sample material remaining after fracture mechanics testing and were mechanically polished down to 0.10 μm diamond suspension followed by vibratory polishing on 0.05 μm alumina suspension. The scans were run at a 0.5 μm step distance for each backscatter pattern reading; thus, each pixel in the resulting maps represents a square of 0.5 μm wide in real space. This dimension was chosen to ensure at least 11 steps for the smallest grains observed. Such conditions produce OIM data with angular resolution below one degree and better than 2 μm resolution on grain size measurements [79].

The resulting OIM maps were then analyzed using EBSD post-processing software called Tango purchased from Oxford Instruments. Such OIM data can provide insight into various

microstructure features, such as average grain size, grain boundary character, analysis of lattice strain in each grain, texture, phase analyses, etc. [79]. The specific data analysis executed on the OIM data depends upon the microstructural feature of interest and the material being studied. In this project, the grain boundary character and average grain size were extracted from the OIM data. Any set of orientation data will include non-indexed data points. Additionally, the local orientation inside each grain will vary pixel to pixel due to differences in local dislocation structures. Such variation in the data must be accounted for.

During data acquisition, an electron beam interacts with the surface and diffracts. From this diffraction pattern, termed the Kikuchi pattern, the crystallographic orientation can be determined [79]. This is done at each 0.5 μm step and recorded. However, near grain boundaries and phase boundaries, the electron beam interaction volume may contain multiple grains/phases, resulting in the detection of multiple diffraction patterns. In this case the software analyzes and records the orientation of the strongest diffraction signal [79]. However, at some locations the separate diffraction patterns may become indistinguishable. Additionally, other locations in the microstructure might contain surface defects such as pits or scratches, resulting in poor pattern quality that is not usable. Such scenarios are impossible to completely prevent, but should be limited as much as possible since they lead to non-indexed data points (or pixels) in the OIM map. During post processing, the non-indexed data points are given the orientation of neighboring pixels.

The orientation variation due to the creation of dislocation networks is resolvable in OIM data and are present in the grains since the specimens were extracted from fracture mechanics samples after loading [80]. While such data are useful when analyzing the local strain inside each grain, it is not useful when characterizing grain boundary character. Similar variation near the location of titanium-carbide impurities was also observed. Variation in grain boundary orientation inside each grain complicates grain boundary character and connectivity analyses by introducing very small (0.5 to 1 μm) false CSL segments in grain boundaries otherwise determined to be a high angle, random boundary everywhere else along the grain boundary. This was observed most often at the intersection between a CSL boundary and a high angle, random boundary or when the crystallographic orientation for that pixel was not indexed correctly, due to either a very small surface defect from imperfect polishing or possibly the detector is detecting

backscatter from another phase in the matrix, such as a titanium carbide precipitate. This adversely affected the grain boundary connectivity analysis, which was done by counting neighboring pixels. In order to overcome this problem, the orientation of each grain was averaged using the Tango software.

The grain boundary character in each material lot was determined. Low energy “Special” boundaries were considered to be grain boundaries of low misorientation (less than 15°) and CSL boundaries of $1 < \Sigma < 29$, consistent with other studies [16, 47-49, 53]. Grain boundaries of misorientation angles below 5° were not included in the study as the vast majority of these misorientations were found inside the grain as opposed to across grain boundaries. Since HEAC in Monel K-500 causes IG cracking, misorientations inside each grain are of secondary interest to this project. The total area per volume of special boundaries and random, high angle boundaries are reported.

The connectivity of any microstructure feature can be quantified using the box-counting method [53]. A trace of the random, high angle boundary network can be acquired from the OIM micrograph data. Then, the maximum conductivity network (MCN) can be extracted. In order to find the MCN, first the Tango EBSD post analysis software is used to show only random, high angle boundaries in black. Two data points were considered connected if they were adjacent or one pixel apart. In real space, this relates to a spacing of 0.5 μm and was chosen so that a single non-indexed data point along the grain boundary would not affect the connectivity analysis. In addition, 0.5 μm is smaller than x_{crit} , which was previously determined to be 1 μm [8, 10]. Thus, a crack advancing along a random, high angle grain boundary would not be affected if it encountered a 0.5 μm short “Special” boundary since it would be shorter than x_{crit} . A custom computer program is used to find the longest path of connected black pixels in the photos and highlight that path in red. This red path is the MCN. The MCN is then overlaid with a square grid, each box of side length η . For this analysis, side lengths of 12.5, 25, and 50 μm were chosen for η . An example of an MCN with the grid overlaid is shown in Figure 2.4. The number of boxes containing part of the MCN, $N(\eta)$ is then counted; this process is then repeated for the other box sizes. The fractal dimension of the MCN, D_R , is defined as,

$$D_R = -\frac{\log[N(\eta)]}{\log[\eta]} \quad [53]. \quad (18)$$

Note that increasing fractions of special boundaries will decrease D_R [53]. Thus, a high D_R reflects greater connectivity of the random, high angle grain boundaries, enabling a quantitative comparison of random, high angle grain boundary connectivity across all the microstructures studied. The calculated D_R values for the Monel K-500 lots are to be reported, where η ranged from 12.5 μm to 50 μm . This range of values was chosen to be close to the range of grain sizes evident in the microstructures of all material lots studied. Identical reasoning was successfully employed in previous fractal analysis studies [53, 81]. Theoretically, the minimum usable box size is slightly larger than the smallest fractal element length, since decreasing the box size further does not reveal new elements to be revealed and counted [81]. In this study, the smallest element length is the upper bound for considering two pixels to be connected used when identifying the MCN, 1 μm . Below this minimum length, the relationship between $\log(N)$ and $\log(\eta)$ becomes nonlinear since the number of boxes containing fractal elements (red pixels) is dependent upon the spacing of the boxes used rather than the nature of the MCN being studied, introducing error into the D_R calculation [81]. The box size range of 12.5 to 50 μm used in this study ensures accurate D_R measurements.

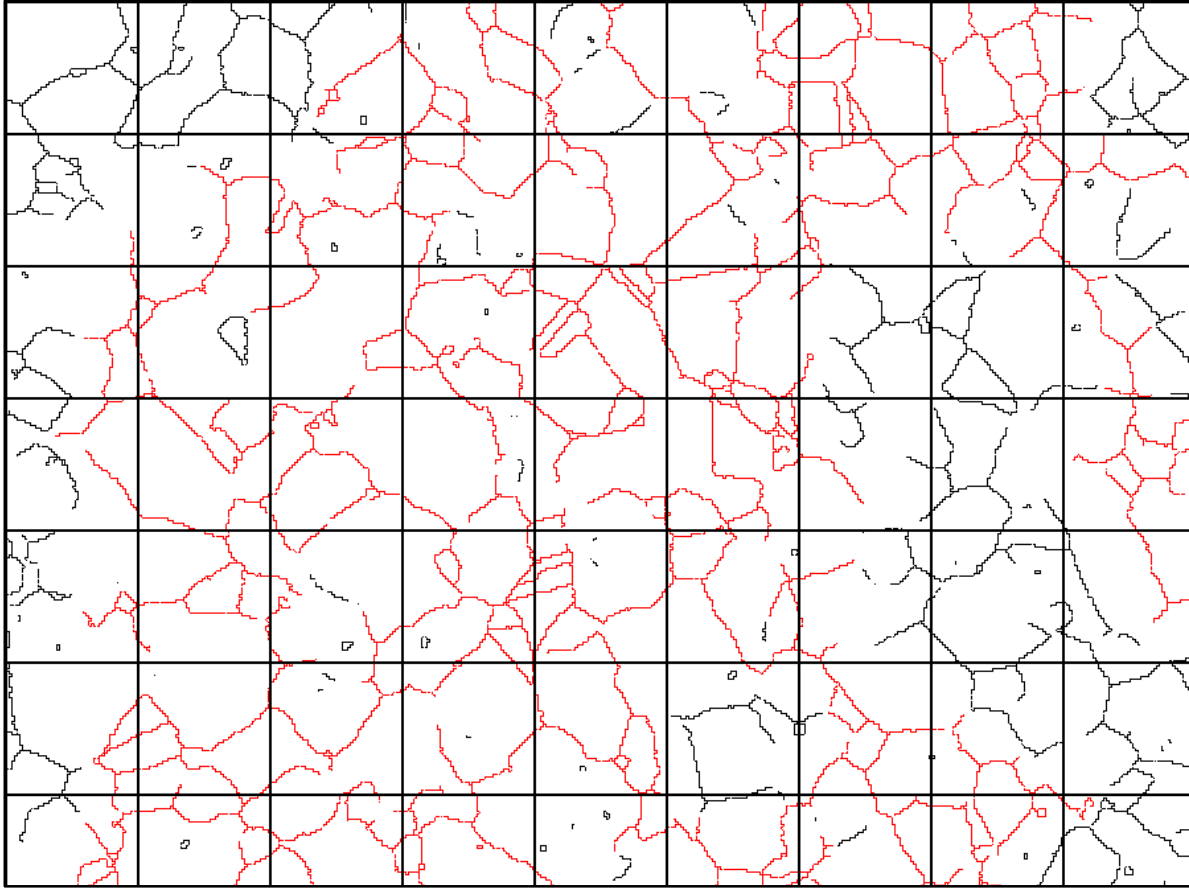


Figure 2.4: Example of an MCN (shown in red) with a 25 μm grid spacing overlaid for connectivity analysis. More detail is given in Figure 4.6 and Section 4.2.3.

3 Results

3.1 Cracking Behavior

3.1.1 Inert Environment Testing

The da/dt versus K_I results for Allvac, TR1, TR2 and TR3 tested in a dry nitrogen gas environment are shown in Figure 3.1. The nitrogen gas environment was chosen to lower the residual humidity in the cell chamber. A humidity probe was inserted in the cell and monitored manually throughout the testing duration. The flow of nitrogen gas to the cell was manually set with each reading to raise, lower, or maintain the humidity in the cell chamber appropriately. In this way, a target residual humidity below 10 percent was maintained for the test duration.

The da/dt velocity versus stress intensity data indicate two regimes of behavior in each

material lot studied. First, at low K_J ($10 < K_J < 35 \text{ MPa}\sqrt{\text{m}}$) dcPD rises with K_J , producing da/dt measurements ranging from 0.4 nm/s to 2.0 nm/s. In this region, the rise in potential is interpreted to be due to increasing crack tip plasticity accrued as the load is increased monotonically to achieve higher K values. Increasing crack tip plasticity increases the local resistivity, thereby increasing the potential measured by the dcPD setup. This effect cannot be accounted for using remote-reference probe normalization since the reference probes are not sensitive to the local area about the crack tip. This interpretation is consistent with similar false crack growth observed in high strength steels, where SEM microscopy confirmed that no crack extension was associated with the measured da/dt values at low K and inert environments [72 in 10].

The false crack growth data for a dK/dt of $0.33 \text{ MPa}\sqrt{\text{m/hr}}$ in the initial regime are fit to establish the resolution limit for the alloy:

$$da/dt_{\text{limit [mm/s]}} = 1.12 \times 10^{-9} K_J + 8.28 \times 10^{-8}, \quad (19)$$

where K_J is in $\text{MPa}\sqrt{\text{m}}$, these values are consistent with previously reported limits for Monel K-500 [8]. The level of false dcPD rise due to the crack tip plasticity is expected to be independent of loading rate; as such, the resulting resolution limit on da/dt should scale linearly with the applied dK/dt . This is confirmed by inert testing results at a K -rate of $1 \text{ MPa}\sqrt{\text{m/hr}}$, where the plasticity induced growth rates increase by roughly 3-fold over the $0.33 \text{ MPa}\sqrt{\text{m/hr}}$ data. In the $1 \text{ MPa}\sqrt{\text{m/hr}}$ case, before cracking is occurring, the same unit of plastic damage (described the change in K) is accomplished in a third of the time relative to testing at $0.33 \text{ MPa}\sqrt{\text{m/hr}}$. Thus, the resolution limit for the testing at the faster K -rate is given by tripling the intercept (8.28×10^{-8}) in Equation 19. In Figure 3.1, the upper resolution limit shown is for testing done at a K -rate of $1 \text{ MPa}\sqrt{\text{m/hr}}$ and the lower limit resolution shown is for testing done at a K -rate of $0.33 \text{ MPa}\sqrt{\text{m/hr}}$. The appropriate resolution limit value is reported in the remaining data plots.

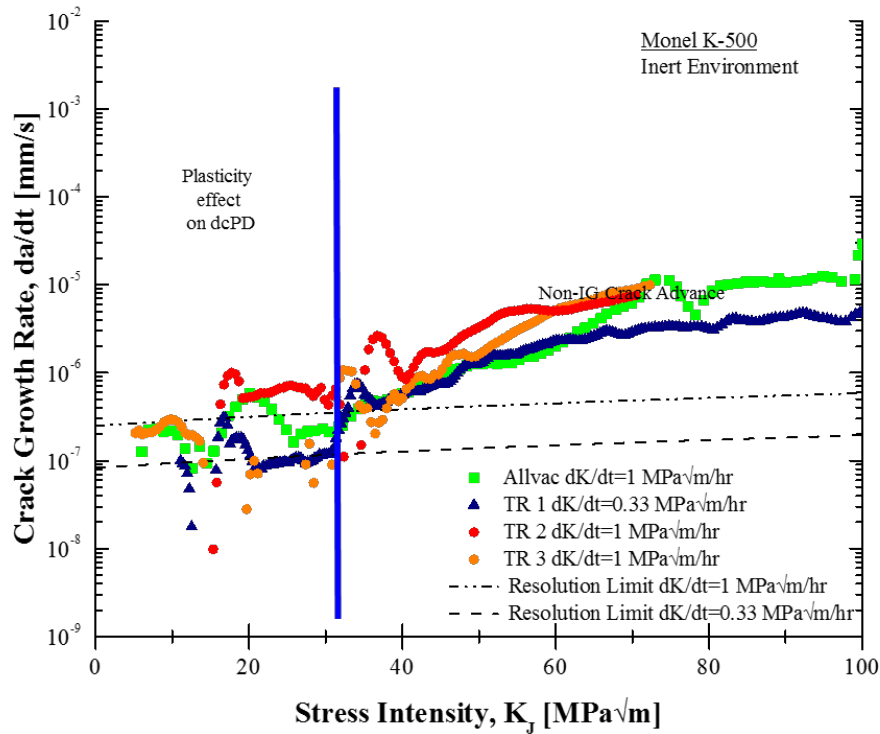
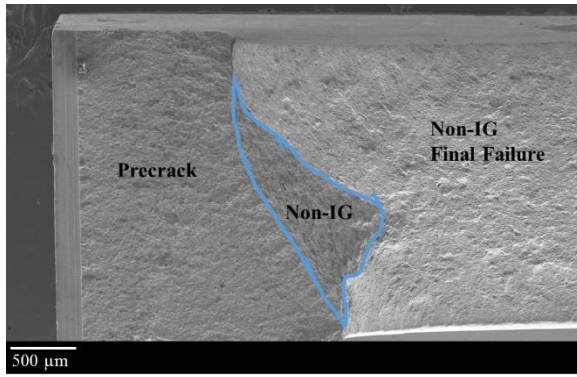
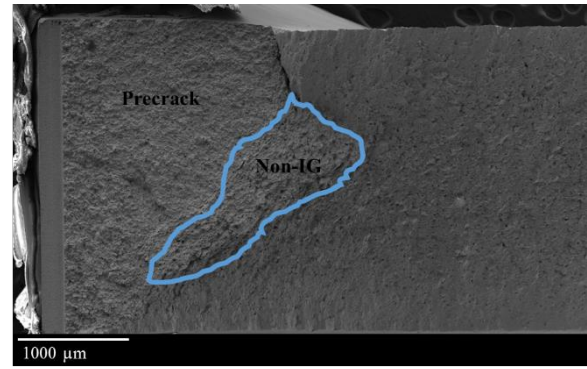


Figure 3.1: Crack growth rate vs K_I for several aged Monel K-500 lots in inert environment (low humidity N_2). The tests were stressed at a constant dK/dt as shown in the legend. The vertical blue line separates two regimes of da/dt measurements. Left of the blue line, false da/dt data results from plasticity damage accruing at the crack tip. Right of the blue line, measured da/dt is shown for real crack growth due to microvoid coalescence

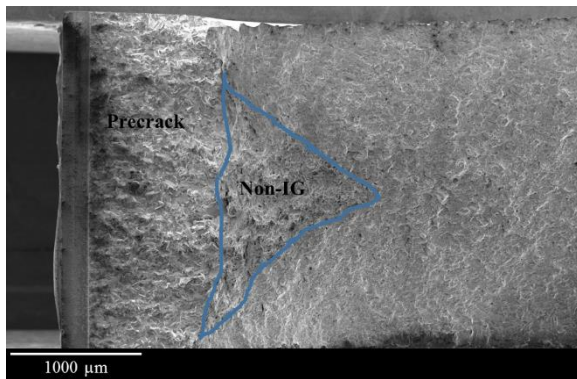
The second regime of crack growth normally occurred after a K_I of $35 \text{ MPa}\sqrt{\text{m/hr}}$, showing da/dt above the resolution limit. SEM fractography shown in Figure 3.2 revealed non-intergranular crack advance in the central portion of the SEN(T) fracture surface. This crack advance was surprising as it occurs well below the reported K_{IC} values for Monel K-500, which ranged from 198 to $340 \text{ MPa}\sqrt{\text{m}}$ [8]. This crack behavior was also observed well below K_{IC} in previous Monel K-500 testing in open air and at low levels of cathodic protection [8]. Such cracking occurred in all materials when tested in inert environments.



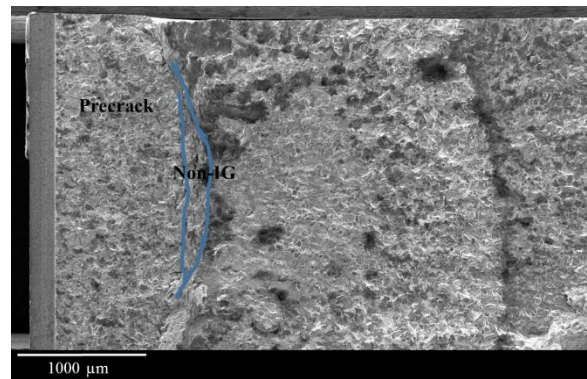
(a)



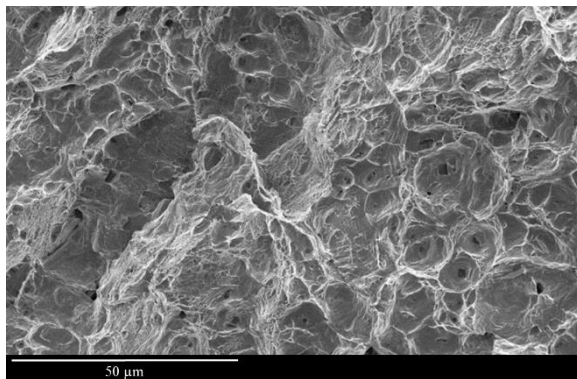
(b)



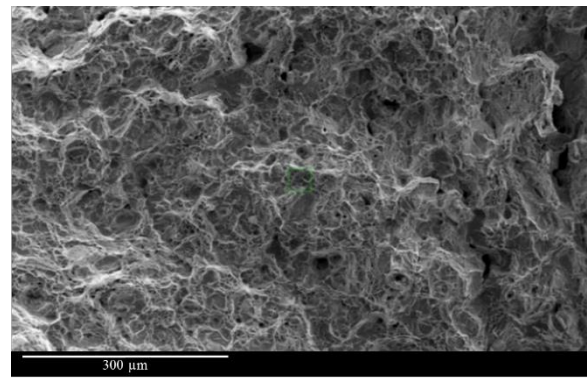
(c)



(d)



(e)



(f)

Figure 3.2: SEM fractography (crack growth going left to right) of (a) Allvac Monel K-500 material lot (b) TR 1, (c) TR 2, (d) TR 3, (e) non-intergranular crack growth morphology in Allvac material and (f) non-intergranular crack morphology in TR 2 material during inert environment testing.

Fractography in the region of stable microvoid cracking shown in Figure 3.2 (e) and (f) shows the presence of microvoids similar to those associated with final ductile failure of this

alloy and is similar to those seen in other studies on Monel K-500 [8, 31, 69]. The size of the microvoids did not vary between material lots, with microvoids typically being tens of micrometers in diameter. Figure 3.3 and Figure 3.2 shows the microvoids in this region are distinct from the rapid ductile failure that occurred after testing to break the specimen completely. The microvoids during the stable microvoid cracking appear deeper than those in the region of final failure. However, portions of final failure occurred at a 45° angle, as expected from final failure of a ductile material while the stable microvoid cracking occurred on the same plane as the fatigue precrack (perpendicular to the loading axis). Thus, the deeper appearance of the microvoids during the stable crack growth below K_{IC} may be an artifact of the fracture surface orientation in the SEM. Nonetheless, the stable crack growth is distinct from the final ductile rupture that occurred at the end of the test.

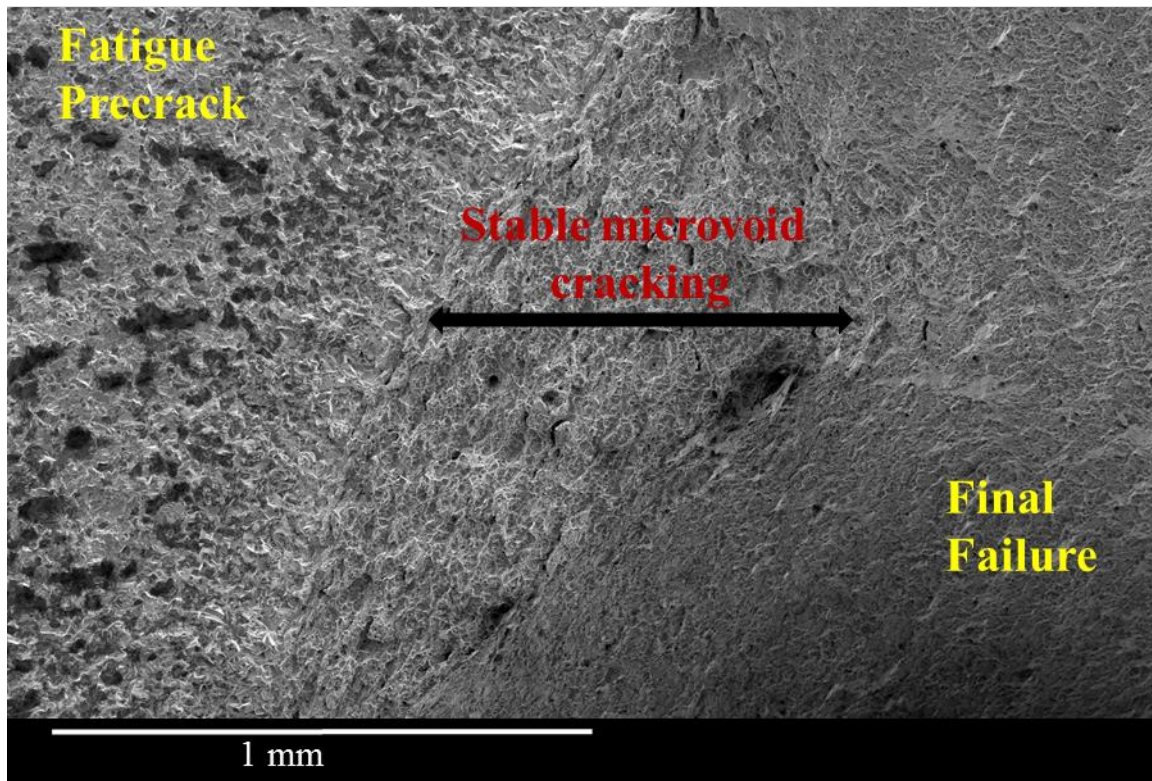


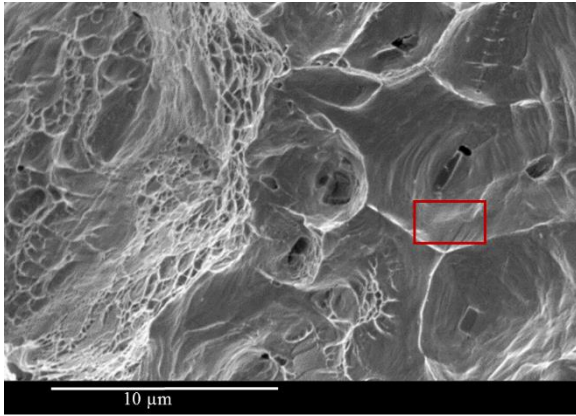
Figure 3.3: Stable microvoid cracking region in Allvac Monel K-500 during inert environment testing executed at a dK/dt of $0.33 \text{ MPa}\sqrt{\text{m}}$.

High resolution SEM and EDS, shown in Figure 3.4 and Figure 3.5, was carried out on TR 2 and Allvac materials to investigate the microvoid cracking well below K_{IC} . These two

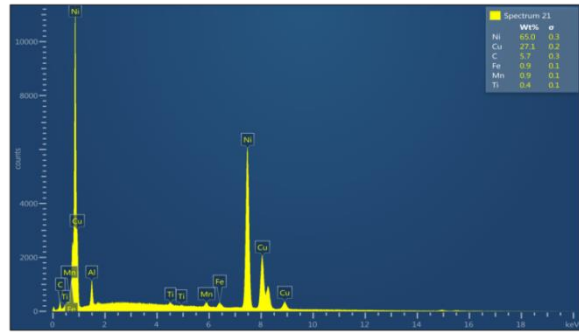
materials were chosen because their corresponding crack growth kinetics during the stable microvoid cracking exhibited the most lot-to-lot variation.

Titanium rich metal carbides were identified via EDS spectroscopy at the bottom of every large microvoid, with larger metal carbides correlating to larger microvoid size in both TR 2 and Allvac materials, and are shown in Figure 3.4 and Figure 3.5. The EDS profiles of the matrix material yield elements compositions similar to those in Table 2.1 aside from slightly elevated carbon levels being measured in the EDS analysis. This is likely due to (a) surface contamination from exposure to the atmosphere after testing or (b) the EDS detecting the carbon in the nearby titanium carbide precipitates. Other elements besides titanium and carbon are present in the EDS profiles of the precipitates in Figure 3.5 since the interaction volume of the electron probe is larger than the particles under investigation. However, the EDS spectra in Figure 3.4 and Figure 3.5 clearly show the titanium and carbon levels are significantly higher in the particles than in the alloy matrix.

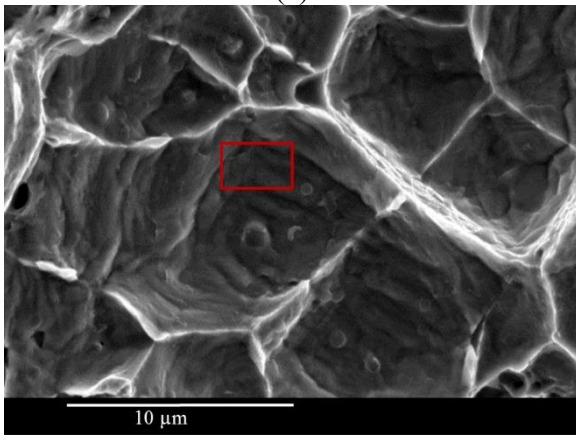
Previous work on the microstructure of Monel K-500 also found titanium rich metal carbides present throughout the microstructure, on the order of a couple μm in size [6, 31, 32]. The consistent presence of embedded metal carbides at the bottom of the microvoids suggests they play an important role in this slow, steady crack growth observed well below K_{IC} . Such crack has been observed in a previous Monel K-500 study in inert N_2 environment and cathodic potentials above $-750\text{mV}_{\text{SCE}}$, though a clear understanding of the transgranular cracking mechanism well below K_{IC} was not presented and is still not fully understood [8]. The prominent role of the titanium rich metal carbides is consistent with microvoid coalescence nucleated at the metal carbide-matrix interfaces.



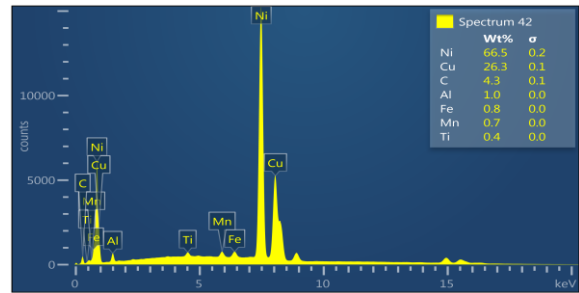
(a)



(b)

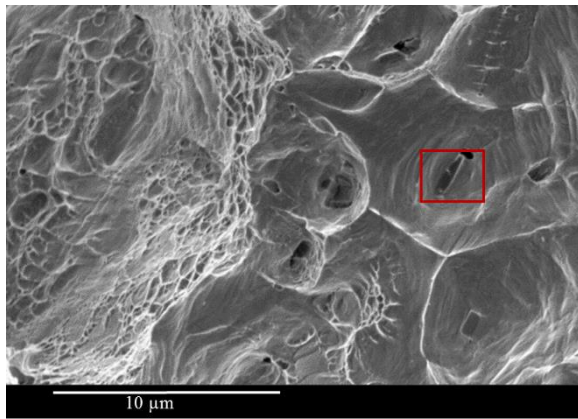


(c)

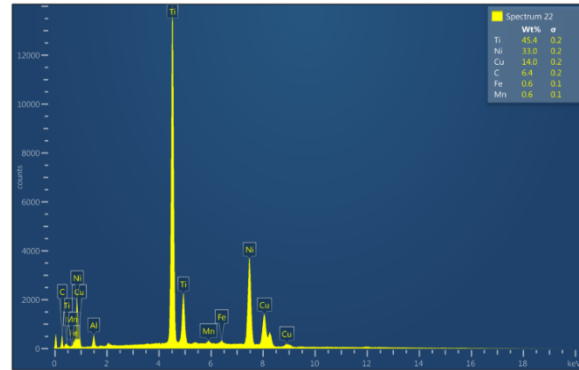


(d)

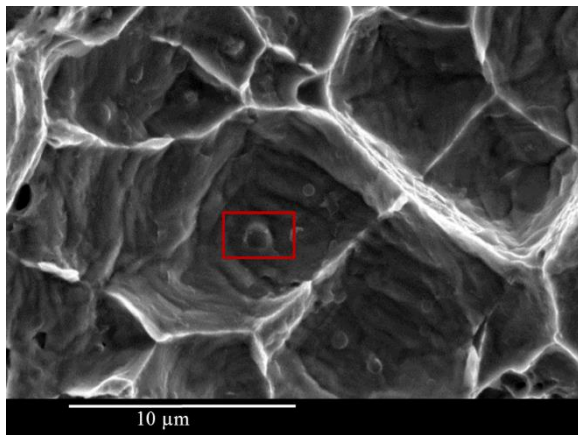
Figure 3.4: (a) SEM fractography showing the matrix EDS locations used for reference comparisons to Figure 3.5 and (b) the EDS spectrum in Allvac material. Similar behavior is evident in the reference EDS measurements of the TR 2 matrix shown in (d), in the location shown in (c).



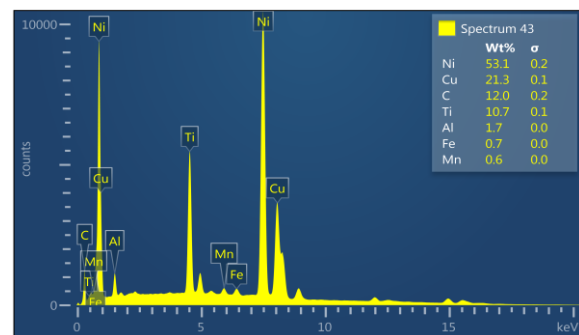
(a)



(b)



(c)



(d)

Figure 3.5: (a) SEM fractography and (b) EDS spectrum showing titanium rich metal carbide located in the center of a microvoid in Allvac material. Similar behavior is evident in the (c) SEM fractography and (d) EDS spectrum of similar carbides inside microvoids in TR 2 material. Identical microvoid morphology is evident in the other TR 1 and TR 3 as well.

3.1.2 Cathodic Potential Testing

3.1.2.1 Testing in synthetic ASTM Ocean Water at $-1000\text{mV}_{\text{SCE}}$

Crack growth kinetics may be hampered by the nucleation and growth of calcareous deposits during fracture mechanics testing. In previous fatigue studies, fatigue resistance of several steels improved in seawater compared to testing under identical cathodic polarization in NaCl. This was attributed to calcareous deposits forming in the crack leading to significant crack closure [82]. Similarly, for the H-embrittlement of stainless steel, calcareous deposit formation created a barrier on the surface of SSRT duplex stainless steel alloy specimens that

caused a decrease in hydrogen embrittlement damage when the potential was lowered to potentials below $-1200\text{mV}_{\text{SCE}}$ [83]. Furthermore, tensile testing of several iron-nickel alloys while under cathodic protection revealed decreased hydrogen embrittlement due to the formation of calcareous scales that formed readily on the surface [84]. In order to investigate the effect of calcareous deposit formation on the HEAC kinetics of Monel K-500, tests were executed at $-1000\text{mV}_{\text{SCE}}$ on the Allvac material lot in ASTM artificial ocean water and 0.6M NaCl.

The results in Figure 3.6 shows testing in ASTM ocean water lead to significantly slower cracking from $20\text{ MPa}\sqrt{\text{m}}$ to $50\text{ MPa}\sqrt{\text{m}}$, effectively delaying the onset of Stage II crack growth. However, da/dt_{II} did not change significantly between testing in 0.6M NaCl and ASTM ocean water, with values of $1.07 \times 10^{-5}\text{ mms/s}$ and $8.2 \times 10^{-6}\text{ mm/s}$ respectively.

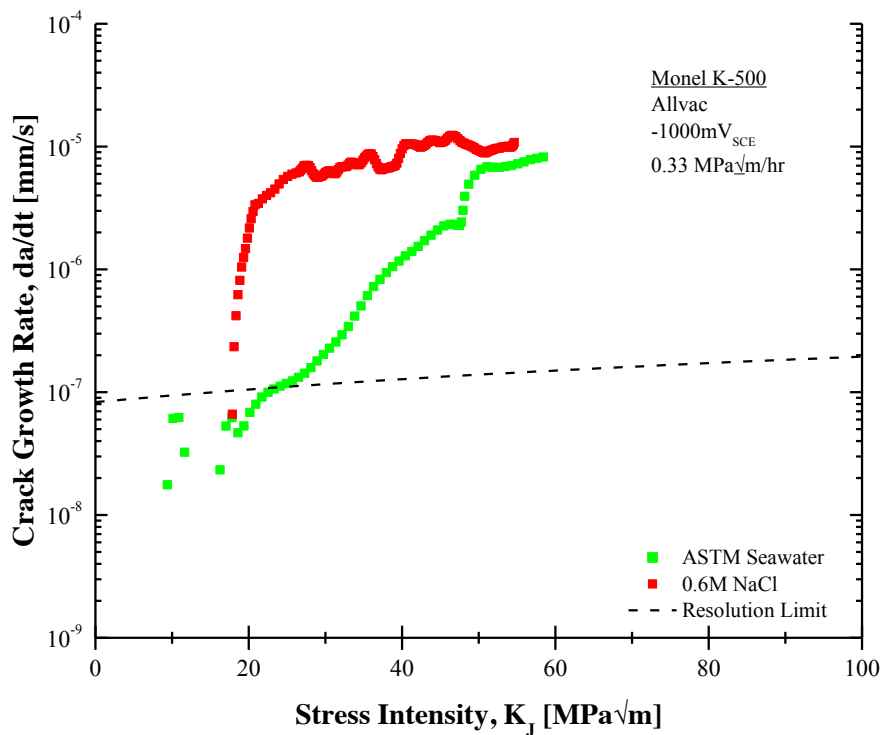
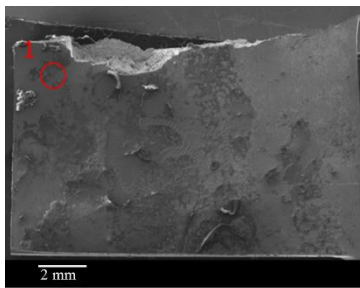


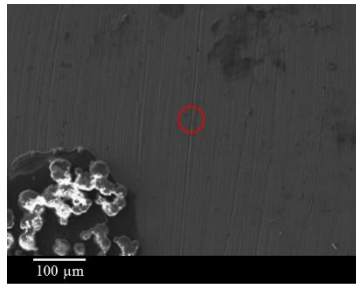
Figure 3.6: Crack growth data of several tests carried out at $-1000\text{mV}_{\text{SCE}}$ in ASTM artificial ocean water on the Allvac Monel K-500 material.

EDS analysis was carried out on several deposits formed on the broad sides of the SEN(T) specimens during testing in ASTM artificial ocean water, the locations selected for

analysis are circled in red in Figure 3.7, with both the macro location shown on the SEN(T) specimen bold surface and a higher magnification image showing the deposit size and shape. Deposits were selected for analysis in order to encompass the full range of deposit structures observed. The analysis shows the deposits are calcareous and magnesium deposits, similar to deposits formed on several other alloy systems during exposure to ocean water [82-84]. The reference EDS spectrum in Figure 3.7 (a, b, and c) show Ni and Cu contents close to what was measured in chemical analysis of the Allvac material in Table 2.1. The error in the EDS composition analysis of the reference material is likely due to the inclusion of Cl and Ca and the exclusion of common alloying elements such as Al, C, Ti, etc. during EDS analysis.



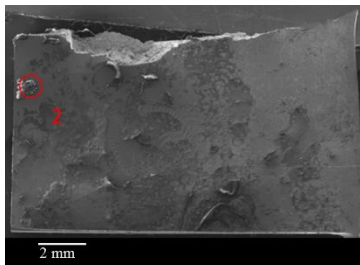
(a)



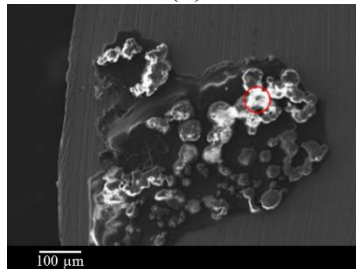
(b)

Element	Wt%	At%
Cl	0	0
Ni	68	69
Ca	0	0
Cu	32	30
Total	100	100

(c)



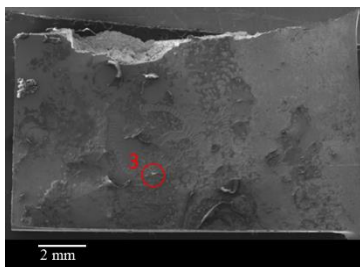
(d)



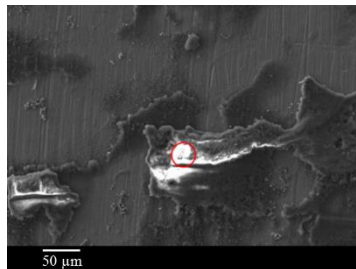
(e)

Element	Wt%	At%
Cl	0	0
Ni	1	1
Ca	97	98
Cu	2	1
Total	100	100

(f)



(g)



(h)

Element	Wt%	At%
Cl	1	1
Ni	3	1
Ca	1	0
Cu	1	0
O	30	41
Mg	64	57
Total	100	100

(i)

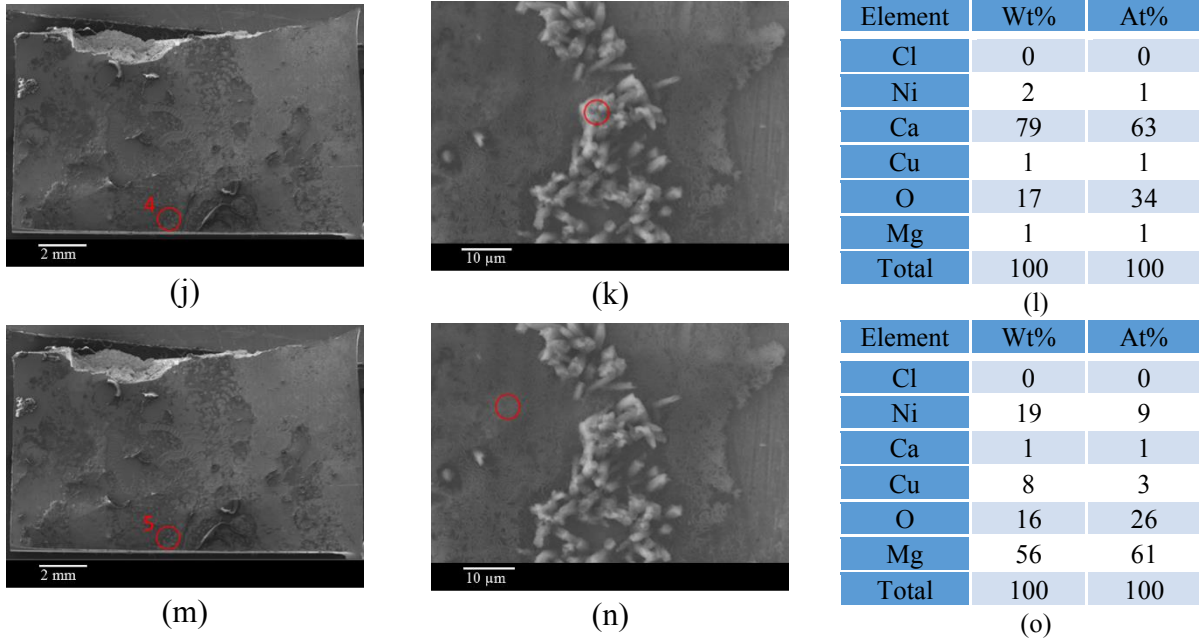


Figure 3.7: EDS analysis of calcium-rich (d, e, f, j, k, l) and magnesium-rich (g, h, i, m, n, o) deposits on SEN(T) specimen surfaces during testing of Allvac Monel K-500 material in ASTM artificial ocean water. A reference spectrum is shown in a, b, and c.

3.1.2.2 Testing at $-950\text{mV}_{\text{SCE}}$ Cathodic Polarization in 0.6M NaCl

Fracture mechanics testing results showing the HEAC behavior for each of the Monel K-500 material lots tested in 0.6 M (3.5 weight percent) NaCl and cathodically polarized to $-950\text{mV}_{\text{SCE}}$ are presented in Figure 3.8. All material lots show similar da/dt_{II} crack growth rates of 6.74×10^{-6} mm/s, 3.44×10^{-6} mm/s, 2.53×10^{-6} mm/s, and 4.05×10^{-6} mm/s for Allvac, TR 1, TR 2, and TR 3 respectively, measured at a K of $60 \text{MPa}\sqrt{\text{m}}$. These growth rates are lower than the da/dt_{II} growth rates of $1.9\text{-}2.3 \times 10^{-5}$ mm/s reported at $-1000\text{mV}_{\text{SCE}}$ and 1.1×10^{-5} mm/s reported at $-900\text{mV}_{\text{SCE}}$ in previous work on the Allvac material [8]. It remains unclear why the da/dt_{II} for the Allvac material measured in this work at $-950\text{mV}_{\text{SCE}}$ are lower than those reported at $-1000\text{mV}_{\text{SCE}}$ and at $-900\text{mV}_{\text{SCE}}$ in the literature for the same Allvac material. However, this is may be an effect of (a) the side masking used in this project that was not present in the previous work or (b) different loading rates at the end of the test.

The possible effects of the masking are not well understood and are discussed in more detail in Appendix B. In this project, da/dt_{II} was measured at a K_{J} of $60 \text{MPa}\sqrt{\text{m}}$ while being loaded according to a dK/dt of $0.33 \text{MPa}\sqrt{\text{m/hr}}$ protocol. In contrast, da/dt_{II} was taken in the

previous work at a K_I of 50 MPa \sqrt{m} while being loaded according to a dK/dt of 1.1 MPa \sqrt{m}/hr [8]. Prior research has shown that active, slow rising K protocols are more damaging than step-hold protocols, where the concurrent crack tip straining and H uptake associated with the slow rising K lead to lower K_{TH} and higher da/dt_{II} measurements [8, 85]. This was attributed to greater accumulation of crack tip plasticity in the slow rising K protocol than in the K step protocol. A similar effect may be evident between the da/dt_{II} measurements in this project taken at the slower dK/dt and the higher da/dt_{II} in previous work measured at a faster dK/dt . The higher dK/dt may lead to greater accumulation of plasticity at the crack tip resulting in the higher da/dt_{II} measurements. However, the effect of dK/dt and crack tip strain rate on the HEAC of Monel K-500 has not yet been quantified and determining the cause of discrepancies in da/dt_{II} measurements between this project and the literature is outside the scope of this project.

The TR 1, TR 2, TR 3, and Allvac material lots also had K_{TH} values of 13, 18, 19, and 29 MPa \sqrt{m} respectively, suggesting Allvac is more resistant to HEAC than TR1, TR2, and TR3 at this potential. These threshold stress intensities are similar to those previously reported on the Allvac material of 16-20 MPa \sqrt{m} at -1000mV $_{SCE}$, 30 MPa \sqrt{m} at -934 mV $_{SCE}$, and 19 MPa \sqrt{m} at -900mV $_{SCE}$ [8].

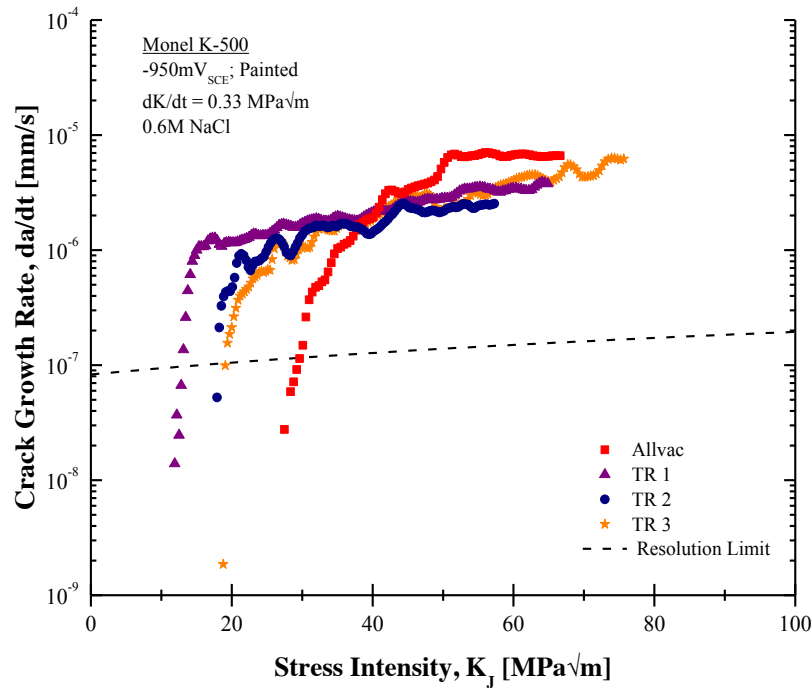


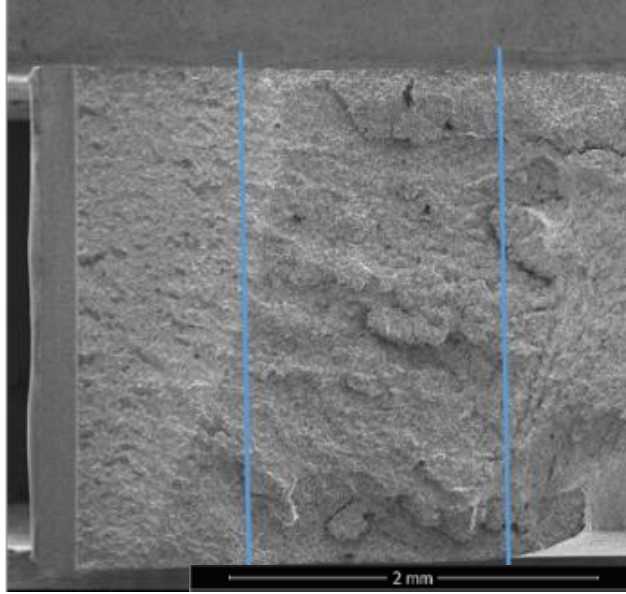
Figure 3.8: Results of fracture testing in 3.5 weight percent (0.6M) NaCl under a constant cathodic potential of $-950\text{mV}_{\text{SCE}}$. Loading was set to achieve a dK/dt rate of $0.33\text{ MPa}\sqrt{\text{m/hr}}$. The dotted line shows the resolution limit associated with this ramp rate as measured in inert environment testing.

Fractography, shown in Figure 3.9 revealed full intergranular cracking due to hydrogen embrittlement in all materials studied. The typical fracture surface contained a smooth section where the EDM notch was placed along one edge of the SEN(T) specimen. This was followed by a section of TG crack growth involving faceted slip band cracking typical of fatigue crack growth in this alloy. A section of IG crack growth then followed, the area of crack growth contained between the two blue vertical lines, which occurred during HEAC testing. Finally, a section of ductile failure is evident as the specimen was pulled apart to break the sample after HEAC fracture mechanics testing.

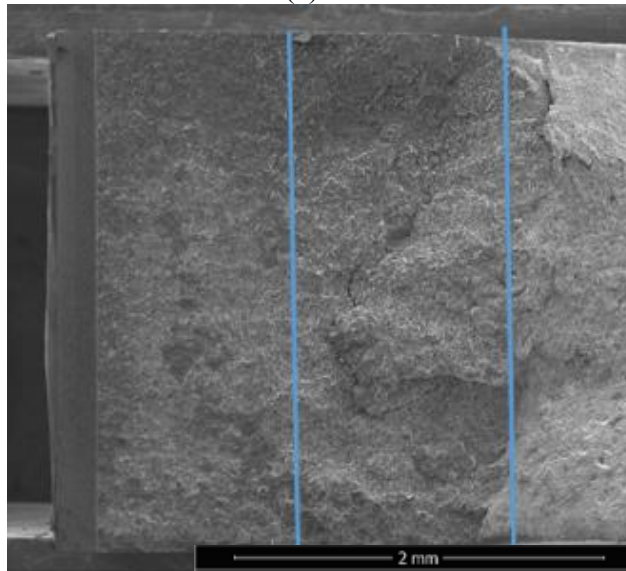
Higher magnification fractography of each fracture surface (each at roughly a K of $40\text{ MPa}\sqrt{\text{m}}$) shown in Figure 3.10 revealed complete IG cracking with only small sections of TG cracking evident in the Allvac material in Figure 3.10 (a). All the images are taken at the same magnification, as shown by the scale bars, thus the different grain facet size in each material reflect differences in grain size between material lots and are readily apparent in Figure 3.10. A

more complete analysis of the grain size differences is given in Section 3.2.1.

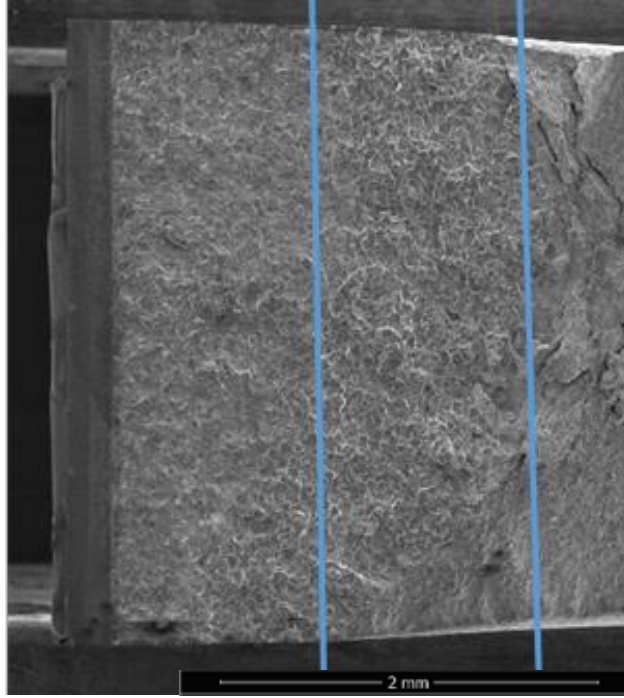
It has been suggested that the slip behavior depends on the distribution and size of the γ' particles in the alloy [24, 32]. The γ' attributes will depend on the heat treatment and therefore may differ between material lots used in the field, which may lead to variation in dislocation cell structures that develop beneath the grain boundary facets during straining [24, 31]. The dislocation cell structures have been shown to loosely correlate to slip traces on the grain boundary facets, which can be viewed in the SEM on the fracture surface, allowing for a first-order comparison of the γ' distribution and size between the material lots [24]. Comparison of the slip traces on the IG facets in each material lot is shown in Figure 3.11. The slip traces indicate several slip systems were active during straining in all material lots, as evident by slip traces going in multiple directions on the IG facets. Similar slip trace densities and slip step heights were also observed in all materials, suggesting similar dislocation cell structures are present beneath the grain facets across all materials. This rough macro-scale analysis revealing slip trace similarities present amongst all materials suggest large differences in γ' size and distribution are not present between the material lots. This is supported by the similar Ramberg-Osgood hardening coefficients measured for each material in Table 2.2, since the hardening behavior in the alloy system is mostly governed by the γ' size and distribution as well [32]. A complete comparison of the γ' character in each material lot would require study at higher magnification, using transmission electron microscopy, which is currently outside the scope of this work. However, the slip trace analysis and similarities in Ramberg-Osgood hardening coefficients suggest there is likely not large variation in γ' character between the material lots in this study.



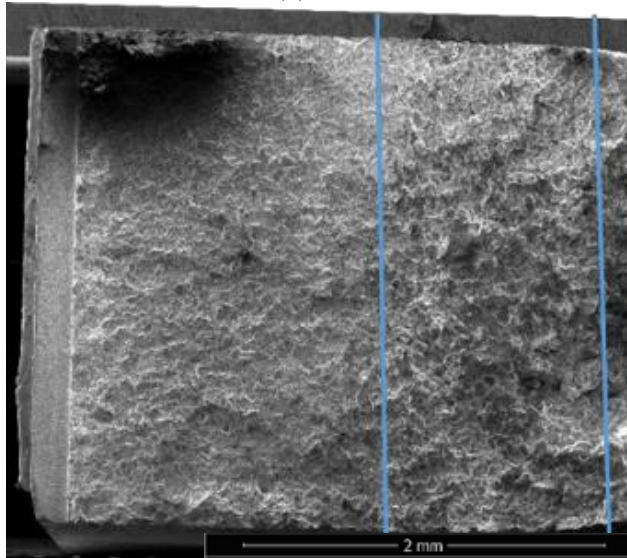
(a)



(b)

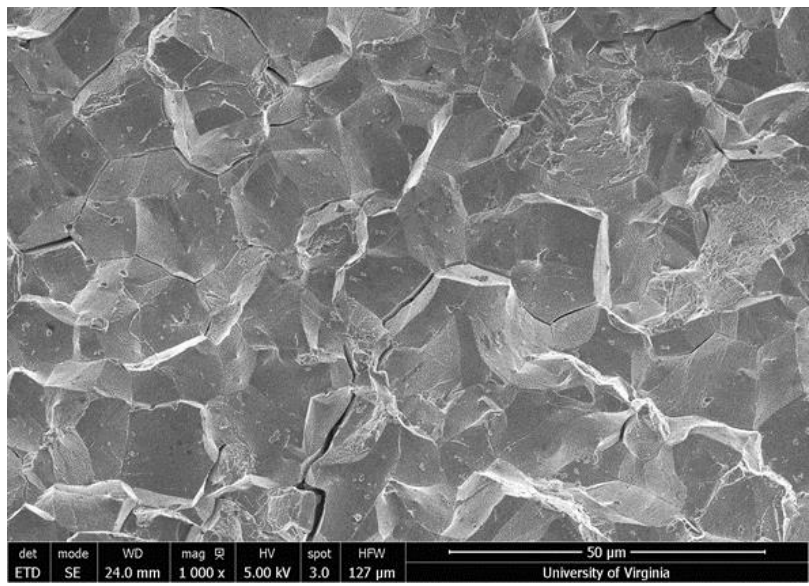


(c)

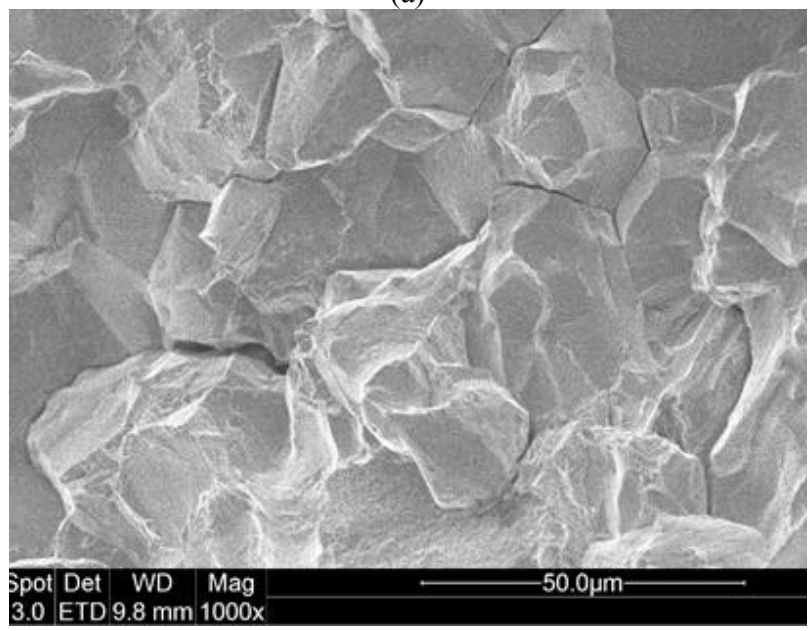


(d)

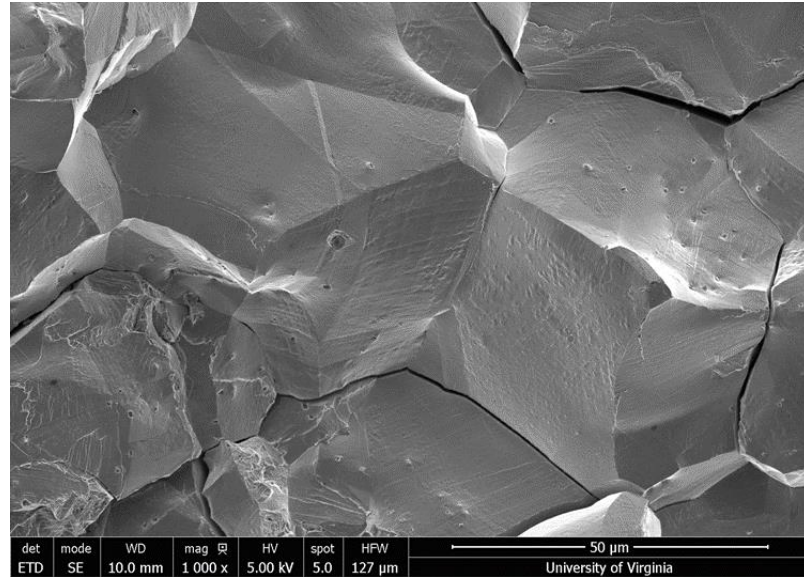
Figure 3.9: Macroscopic scale of (a) Allvac, (b) TR 1, (c) TR 2, and (d) TR 3 lots of Monel K-500 tested in 0.6M NaCl at $-950\text{mV}_{\text{SCE}}$. The crack growth occurred left to right, the area between the vertical blue lines is the crack growth that occurred during HEAC characterization testing.



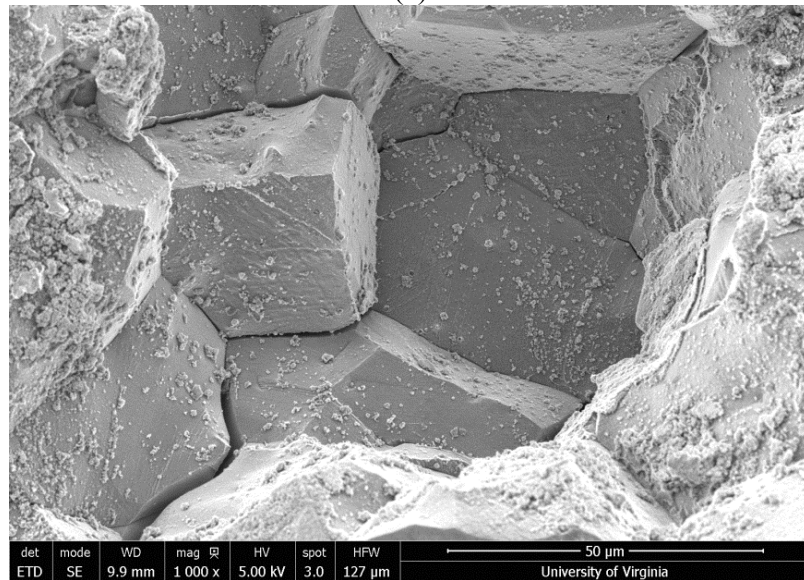
(a)



(b)



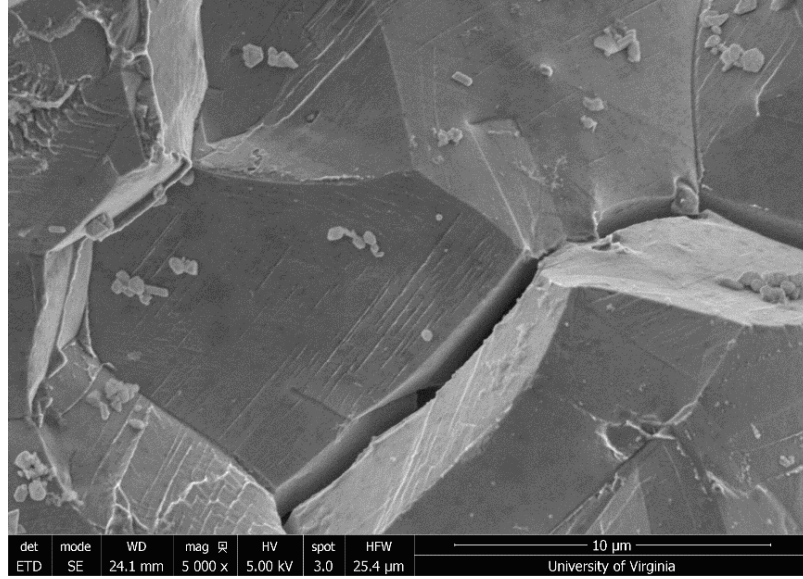
(c)



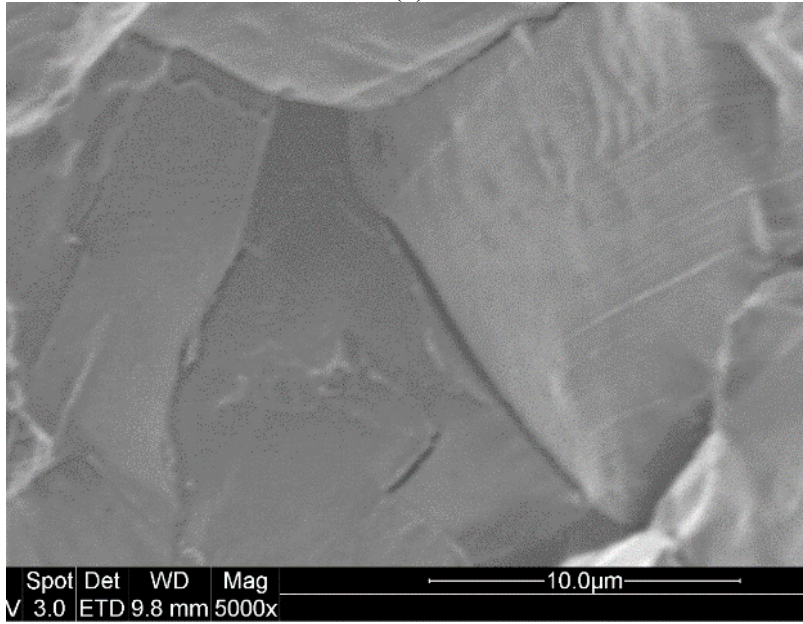
(d)

Figure 3.10: Low magnification SEM images showing IG fracture due to HEAC in (a) Allvac, (b) TR 1, (c) TR 2, and (d) TR 3 material lots of Monel K-500 at $-950\text{mV}_{\text{SCE}}$ in 0.6 M NaCl. Crack growth occurred left to right in all fractographs. On the TR 3 sample in Figure 3.10(d), corrosion product is present. (Footnote *)

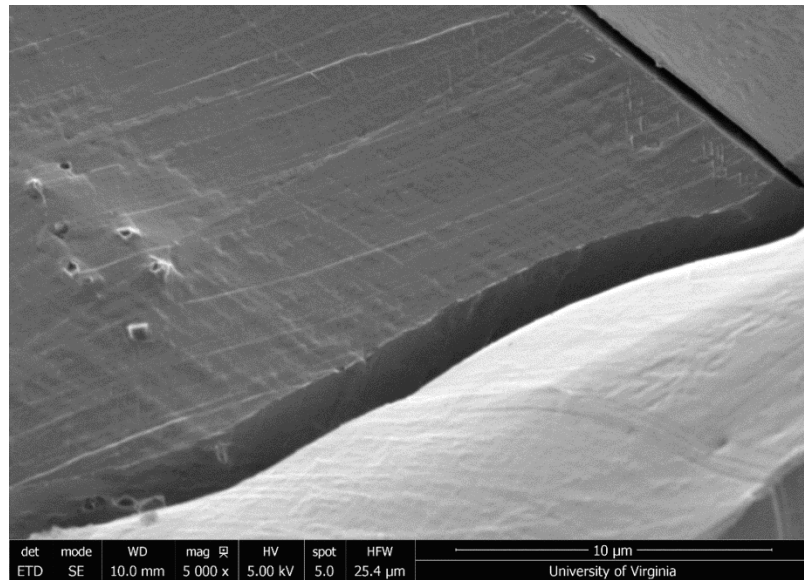
* Corrosion product is present on the fracture surface of TR 3 tested at $-950\text{ mV}_{\text{SCE}}$. This is due to subsequent fatigue protocols and HEAC fracture mechanics characterization tests run on the same sample after the first HEAC test was complete in an attempt to increase the testing matrix. In order to limit the charging of the specimen, subsequent fatigue protocols were run at open circuit potential. This fatigue protocol was necessary to recreate a sharp crack and limit the load history effects of the previous test run on the sample. However, this led to the corrosion of the fracture surface and much of the surface is covered in corrosion products, as evident in Figure 3.10 and Figure 3.11. Similarly, corrosion product is evident on the Allvac fracture surface in Figure 3.11, though to a smaller extent as it was subjected to open circuit potential for a smaller amount of time than the TR 3 sample surface.



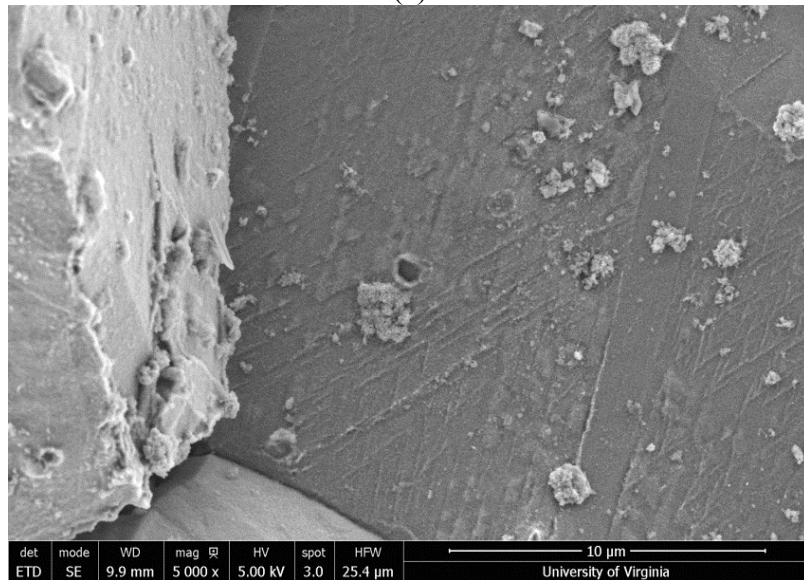
(a)



(b)



(c)



(d)

Figure 3.11: SEM images showing slip lines on IG facets created during fracture testing of (a) Allvac, (b) TR 1, (c) TR 2, and (d) TR 3 material lots of Monel K-500 at $-950\text{mV}_{\text{SCE}}$ in 0.6 M NaCl . Crack growth occurred left to right in all fractographs. Corrosion product is evident on Allvac and TR 3 fracture surfaces (Footnote *).

3.1.2.3 Near-Threshold Cathodic Potential Testing

Prior research established the effect of applied potential on the HEAC behavior of the Allvac material; the results showed no HEAC cracking over a full range of K up to $90\text{ MPa}\sqrt{\text{m}}$ at a polarization of $-750\text{ mV}_{\text{SCE}}$ and a mixture of slow IG/TG cracking at $-800\text{ mV}_{\text{SCE}}$. These data

suggest a threshold for IG HEAC between -750 and -800 mV_{SCE}; consistent with artificial crevice electrochemical testing on the Allvac lot of Monel K-500 results suggesting a drastic decrease in crack tip H-production at -764 mV_{SCE} [8]. Metallurgy based variations in the HEAC behavior are likely to be most prevalent at polarizations near this threshold due to the lower level of C_{H-diff}. As such, the HEAC kinetics were established in this near-threshold potential range (-850mV_{SCE}) in 0.6M NaCl for each of the material lots of interest and are reported in Figure 3.12.

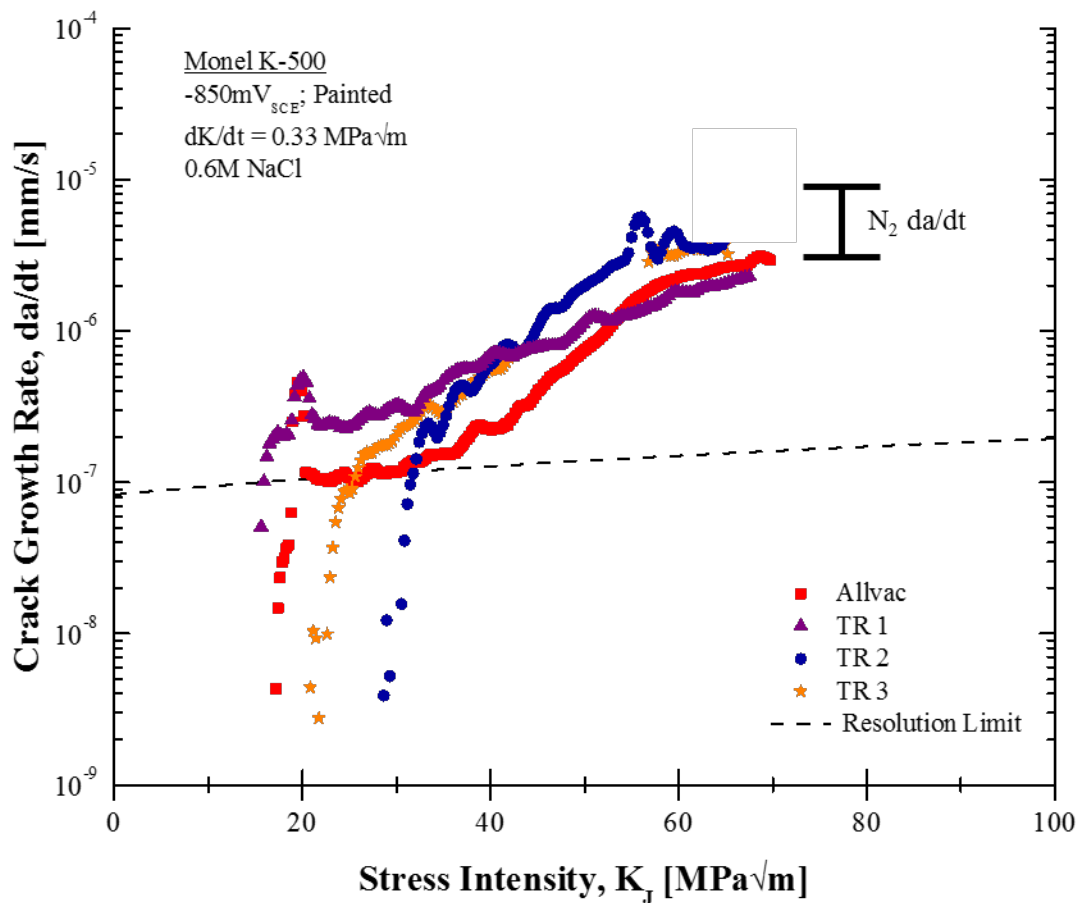


Figure 3.12: Results of fracture testing in 3.5 weight percent (0.6M) NaCl under a constant cathodic potential of -850mV_{SCE}. Loading was set to achieve a constant ramp rate of 0.33 MPa√m/hr. The dotted line shows the resolution limit associated with this ramp rate as measured in inert environment testing. The range of da/dt measured in inert (N₂) environment testing is also indicated.

The TR1, TR 2, and TR 3 material lots all had similar da/dt_{II} crack growth rates of 1.8×10^{-6} mm/s, 4.4×10^{-6} mm/s, and 3.2×10^{-6} mm/s at a K of $60 \text{ MPa}\sqrt{\text{m}}$ with K_{TH} values of 16, 32, and $26 \text{ MPa}\sqrt{\text{m}}$ respectively. These measured da/dt_{II} crack growth rates are similar to those measured previously in the literature, where values of 3.7×10^{-6} mm/s and 2.5×10^{-6} mm/s were reported during testing in 0.6M NaCl at -850 mV_{SCE} at a K of $50 \text{ MPa}\sqrt{\text{m}}$ for the Allvac material lot [8]. The measured K_{TH} values for TR 1 and TR 3 were lower than the $38 \text{ MPa}\sqrt{\text{m}}$ and $41 \text{ MPa}\sqrt{\text{m}}$ measured for the Allvac material at -850 mV_{SCE} [8]. Macro-scale fractography in Figure 3.13 shows the crack front shape and regions of crack growth in each fracture test at -850 mV_{SCE} . The typical fracture surface contained a smooth section where the EDM notch was placed along one edge of the SEN(T) specimen. This was followed by a section of TG slip-based crack growth typical of fatigue crack growth in this alloy formed during the precrack protocol before HEAC characterization testing. A section of IG/TG crack growth then followed, the area of crack growth contained between the two blue vertical lines, which occurred during HEAC testing. Finally, a section of ductile failure is evident as the specimen was pulled apart to break the sample after testing. Note in Figure 3.13 (a) that the crack advance in the Allvac material occurred only in the center of the specimen, similar to what was observed during inert environment testing. In contrast, Figure 3.13 (b-d) shows the crack advance in TR 1, TR 2, and TR 3 tended to occur homogeneously along the entire crack front. This suggests a different crack growth behavior occurred in Allvac than in TR 1, TR 2, or TR 3.

Fractographic analysis was carried out on each material (roughly at a K of $40 \text{ MPa}\sqrt{\text{m}}$) to investigate the different crack growth behavior observed between the Allvac and tie rod materials during testing at -850 mV_{SCE} . The TR 1, TR 2, and TR 3 fracture surfaces in Figure 3.15 (b-d) consisted mostly of IG facets characteristic of IG cracking due to HEAC with areas of ductile failure associated with TG cracking. The mixed transgranular and intergranular morphologies on the fracture surface is consistent with prior testing and is characteristic of HEAC cracking in the near threshold potential regime for the Monel K-500 alloy [8].

While the growth rate data in Figure 3.12 suggest slightly higher K_{TH} and similar da/dt_{II} for Allvac (specifically, crack growth rate of 2.3×10^{-6} mm/s at $60 \text{ MPa}\sqrt{\text{m}}$ with no crack growth until $31 \text{ MPa}\sqrt{\text{m}}$), the fractographic analysis in Figure 3.15 (a) shows no indication of IG HEAC. Rather, the fracture surface showed ductile failure characteristic of the microvoid cracking

observed during inert environment testing, shown in Figure 3.2, Figure 3.4, and Figure 3.5. The potential at which this transition in crack growth mechanism occurs in the Allvac material is lower than what was reported during previous testing, which showed IG/TG cracking associated with mild HEAC at $-850\text{mV}_{\text{SCE}}$ and $-800\text{mV}_{\text{SCE}}$, and saw non-IG ductile crack growth at $-750\text{mV}_{\text{SCE}}$ [8]. The transition in cracking mechanism is attributed to a decreasing $C_{\text{H}\sigma}$ as the potential becomes less cathodic. Previous work on the Allvac material identifies a threshold potential of $-770\text{mV}_{\text{SCE}}$ above which HEAC is not expected due to a low $C_{\text{H}\sigma}$, with the precise potential likely varying lot-to-lot with small differences in Monel metallurgy [8]. In this project, the transition from HEAC to non-IG ductile cracking occurred in the Allvac material at $-850\text{mV}_{\text{SCE}}$, suggesting that small differences in the experimental setup are altering the position of the threshold potential, leading to significant changes in cracking mechanism since testing is being completed near the threshold potential for the Allvac material.

The root causes of the different Allvac behavior at $-850\text{mV}_{\text{SCE}}$ between testing in this project and in previous work remain elusive. However, two testing protocol differences that stand out are (a) the presence of the side masking and (b) the dK/dt protocol. The side masking reduces the amount of hydrogen produced on the bold surface. However, either specimen flank along the projected crack path (the window in the masking was 1 mm tall and ran 70% of the specimen width) was left uncovered in order to prevent altering the crack tip chemistry between the masked and unmasked testing. If the presence of the masking on the bold surfaces is leading to the difference in cracking behavior observed between this project and previous work, then that would suggest hydrogen produced 0.5 mm away from the cracking plane contributes to the hydrogen concentration at the crack tip during testing. Modeling of bulk hydrogen charging, discussed in detail in Appendix B, suggest a hydrogen concentration 0.1 % of the surface hydrogen concentration is achieved 0.2 mm into the specimen at the end of the test. Thus, if hydrogen produced 0.5 mm away from the crack path is getting into the FPZ, which must be occurring if the presence of the masking is altering the cracking behavior, then some mechanism for enhanced hydrogen diffusion must be present in this alloy system.

Regarding the possible effect of the dK/dt protocol, testing in this project and in previous work used a dK/dt of $0.33\text{MPa}\sqrt{\text{m/hr}}$ in the K regime between 10 and $44\text{MPa}\sqrt{\text{m}}$ [8]. In the previous work the dK/dt was then increased to $1.10\text{MPa}\sqrt{\text{m/hr}}$ until test completion, while in the

present project a dK/dt of $0.33 \text{ MPa}\sqrt{\text{m/hr}}$ was used for the entire test duration [8]. The HEAC K_{TH} is expected to be between 10 and $30 \text{ MPa}\sqrt{\text{m}}$, while the non-IG crack growth is observed to start at a K around $30 \text{ MPa}\sqrt{\text{m}}$ if it occurs. Thus, in either case, the dK/dt protocol is same between this project and the previous work at the onset of cracking, whether that cracking is HEAC or non-IG ductile crack growth. Therefore, the dK/dt protocol differences are not expected be the cause of the different threshold potentials observed in the Allvac material lot.

The ductile fracture surface morphology in the Allvac material is similar to what is observed in inert environment testing, as shown in Figure 3.2. Both surfaces contain microvoids tens of microns in size. A comparison of the crack growth rates measured in electrolyte while charged at -850mV_{SCE} and in inert environment testing is shown in Figure 3.14. The crack growth rates measured at -850mV_{SCE} are lower than what was measured in inert environment up to a K of $55\text{MPa}\sqrt{\text{m}}$. This may be due to the faster strain rate used in the inert environment testing ($1.10 \text{ MPa}\sqrt{\text{m/hr}}$) compared to the near threshold potential testing ($0.33 \text{ MPa}\sqrt{\text{m/hr}}$). Before the onset of crack growth, the faster strain rate would increase the contribution of local plasticity damage accrued at the crack tip (governed by the applied K) in a given amount of test duration. Essentially, the same change in K would be applied in less time for the increased dK/dt rate associated with the inert environment testing. This would lead to a higher measured da/dt for reasons given in Section 3.1.1 up to a K of around $35 \text{ MPa}\sqrt{\text{m}}$. Between a K of $35 \text{ MPa}\sqrt{\text{m}}$ and $55 \text{ MPa}\sqrt{\text{m}}$, the crack growth data between the inert environment test and the test at -850mV_{SCE} merge, possibly implying a decreasing effect of the dK/dt rate on the measured da/dt . Above a K of $55 \text{ MPa}\sqrt{\text{m}}$, the crack growth rates between the two conditions are similar. This suggests that the ductile crack growth was not enhanced by the presence of hydrogen in the FPZ from the presence of cathodic polarization. Detailed material characterization is performed to investigate the higher HEAC resistance in Allvac and the differences between TR 1, TR 2, and TR 3; this is presented in Section 4.2.3.

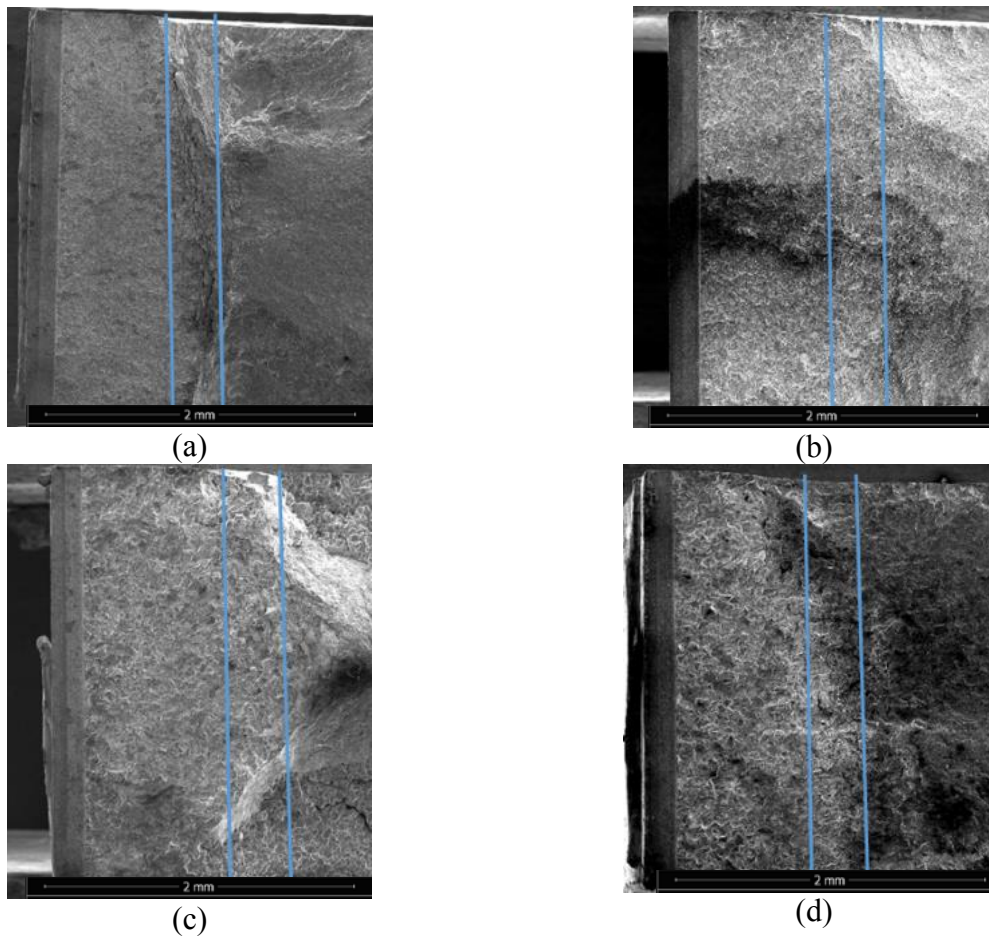


Figure 3.13: Macroscopic scale of (a) Allvac, (b) TR 1, (c) TR 2, and (d) TR 3 lots of Monel K-500 tested in 0.6M NaCl at $-850\text{mV}_{\text{SCE}}$. The crack growth occurred left to right, the area between the vertical blue lines is the crack growth that occurred during HEAC testing.

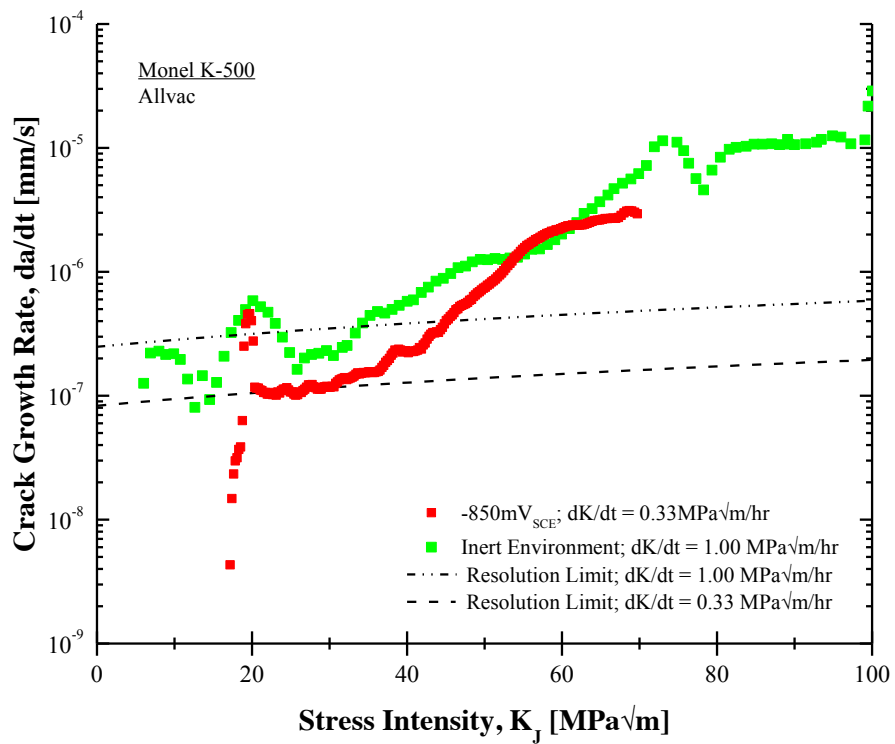


Figure 3.14: Crack growth data of Allvac and TR 2 material lots in inert environment and 0.6M NaCl at -850mV_{SCE}.

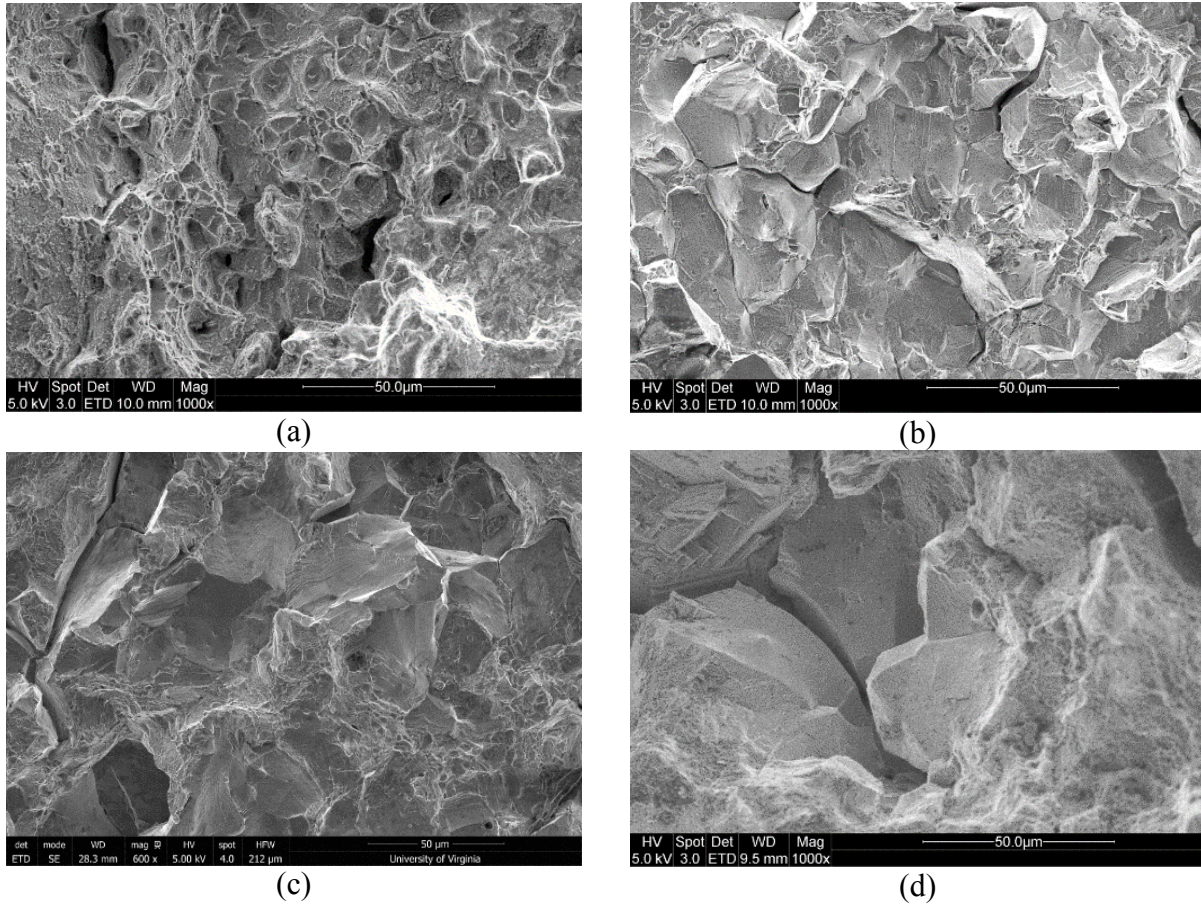


Figure 3.15: Fractography of (a) Allvac, (b) TR 1, (c) TR 2, and (d) TR 3 at $-850\text{mV}_{\text{SCE}}$ in 0.6 M NaCl electrolyte revealing mixed IG/TG cracking associated with mild levels of HEAC in TR 1, TR 2, and TR 3 and ductile-like cracking in the Allvac material lot.

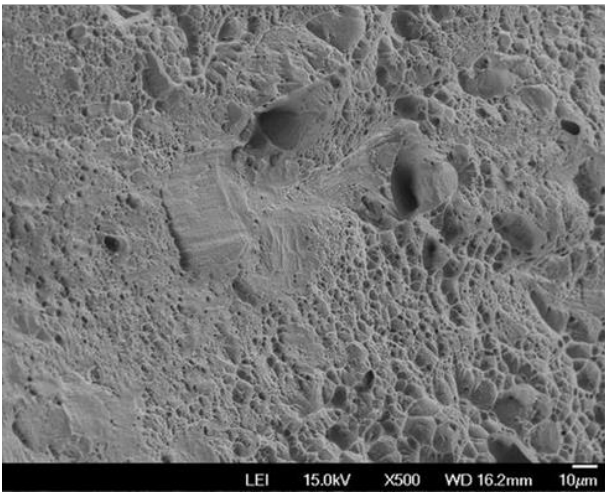
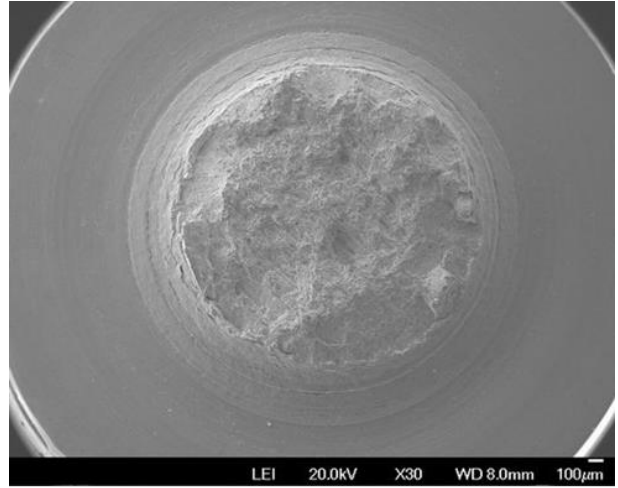
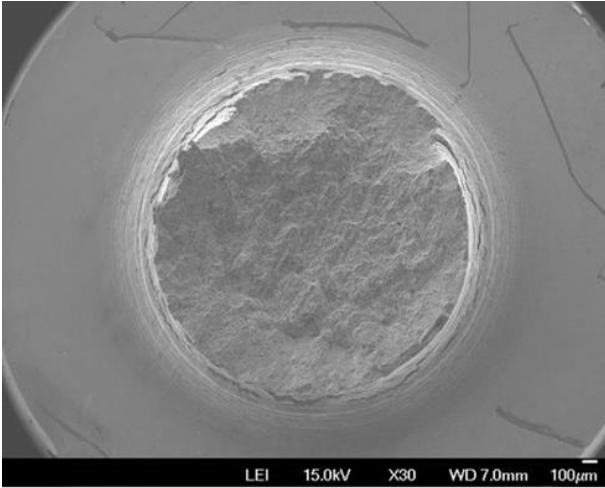
The ductile failure of Allvac at $-850\text{mV}_{\text{SCE}}$ observed in this project highlights that the Allvac material is more resistant to HEAC than TR 1, TR 2, and TR 3. Other evidence presented below also points to increased HEAC resistance in the Allvac material over the three tie rods.

3.1.3 SSRT

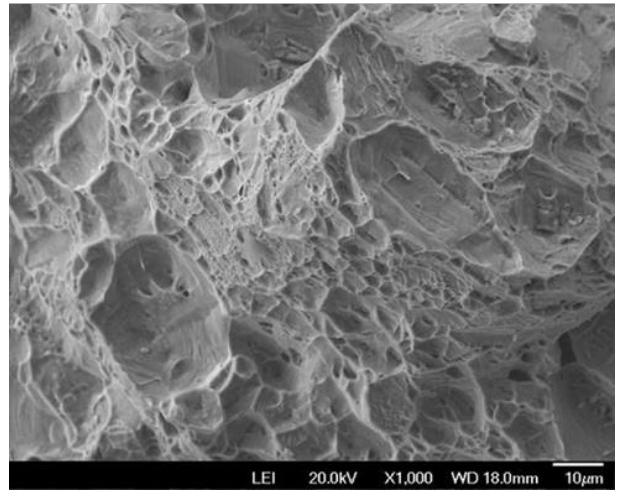
In a companion project, Dr. Hung and Dr. Scully (University of Virginia) performed Slow Strain Rate Testing (SSRT) (ASTM G129) on Allvac and TR 2 material after 24 hours charging in deaerated 0.6M NaCl $-850\text{mV}_{\text{SCE}}$, $-950\text{mV}_{\text{SCE}}$, and $-1100\text{mV}_{\text{SCE}}$. The minimum specimen diameter at the point of failure was 2.4 mm. The tests were run at a cross head speed of 6.33×10^{-6} mm/s. The specimens were exposed to the same environment and potentials during

the testing. Figure 3.16 shows both the macro view of each fracture surface and a high magnification view near the edge of the fracture surface where hydrogen is expected to have diffused into the material for each material and applied potential in the test matrix. The resulting fracture surfaces in Figure 3.16 (a and b) show ductile failure occurred in either material at $-850\text{mV}_{\text{SCE}}$. Both the Allvac and TR 2 fracture surfaces in Figure 3.16 (e and f) show extensive IG failure occurred at $-1100\text{mV}_{\text{SCE}}$. Most importantly, Figure 3.16 (d) shows a small number of IG facets were observed on TR 2 at $-950\text{mV}_{\text{SCE}}$ while Figure 3.16 (c) shows only ductile failure occurring in the Allvac test sample under the same cathodic potential. This further supports the observation from Figure 3.15 and Figure 3.12 that Allvac exhibits greater HEAC resistance as compared to TR 2.

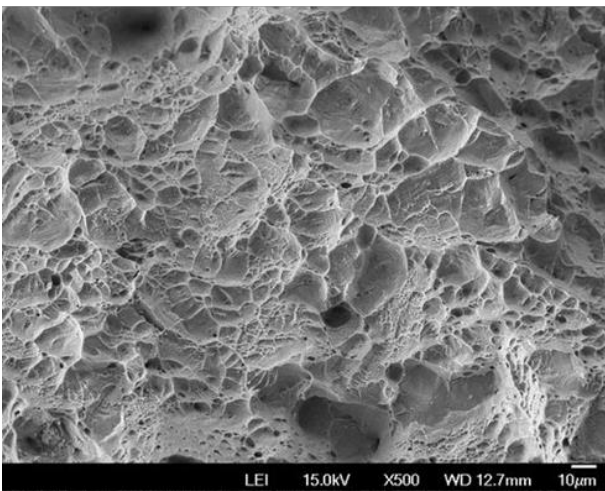
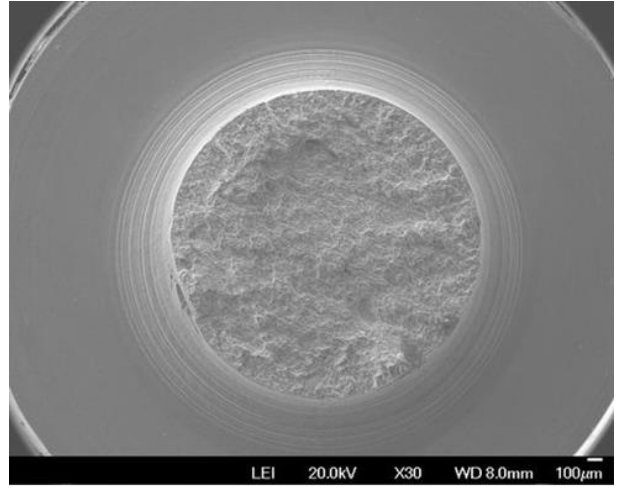
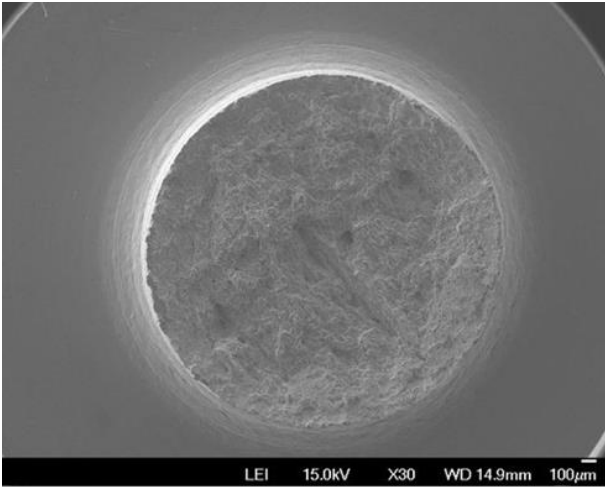
It is not surprising that the potential of $-950\text{mV}_{\text{SCE}}$ at which ductile crack growth occurs in the Allvac material and mild HEAC occurs in the TR 2 material during SSRT testing does not correlate to the potential of $-850\text{mV}_{\text{SCE}}$ established in the fracture mechanics testing. The SSRT specimens do not have a crack like the SEN(T) specimens. This affects the hydrogen behavior since there is (a) no amplification of the hydrogen concentration and (b) a different charging environment. For the SSRT specimen, there is no amplification of the hydrogen concentration associated with the presence of the crack (no C_{H_2}) since there is no crack in the specimen before the onset of failure. Thus, higher bulk hydrogen concentrations are needed to cause HEAC. More hydrogen charging, and therefore a higher applied potential, is necessary to observe HEAC in a SSRT specimen than a SEN(T) specimen. However, both the SSRT and fracture mechanics testing results indicate greater HEAC resistance in the Allvac material compared to the three tie rods.



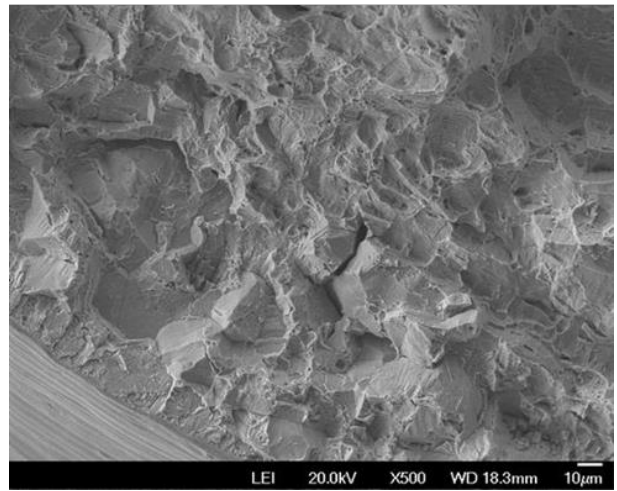
(a)



(b)



(c)



(d)

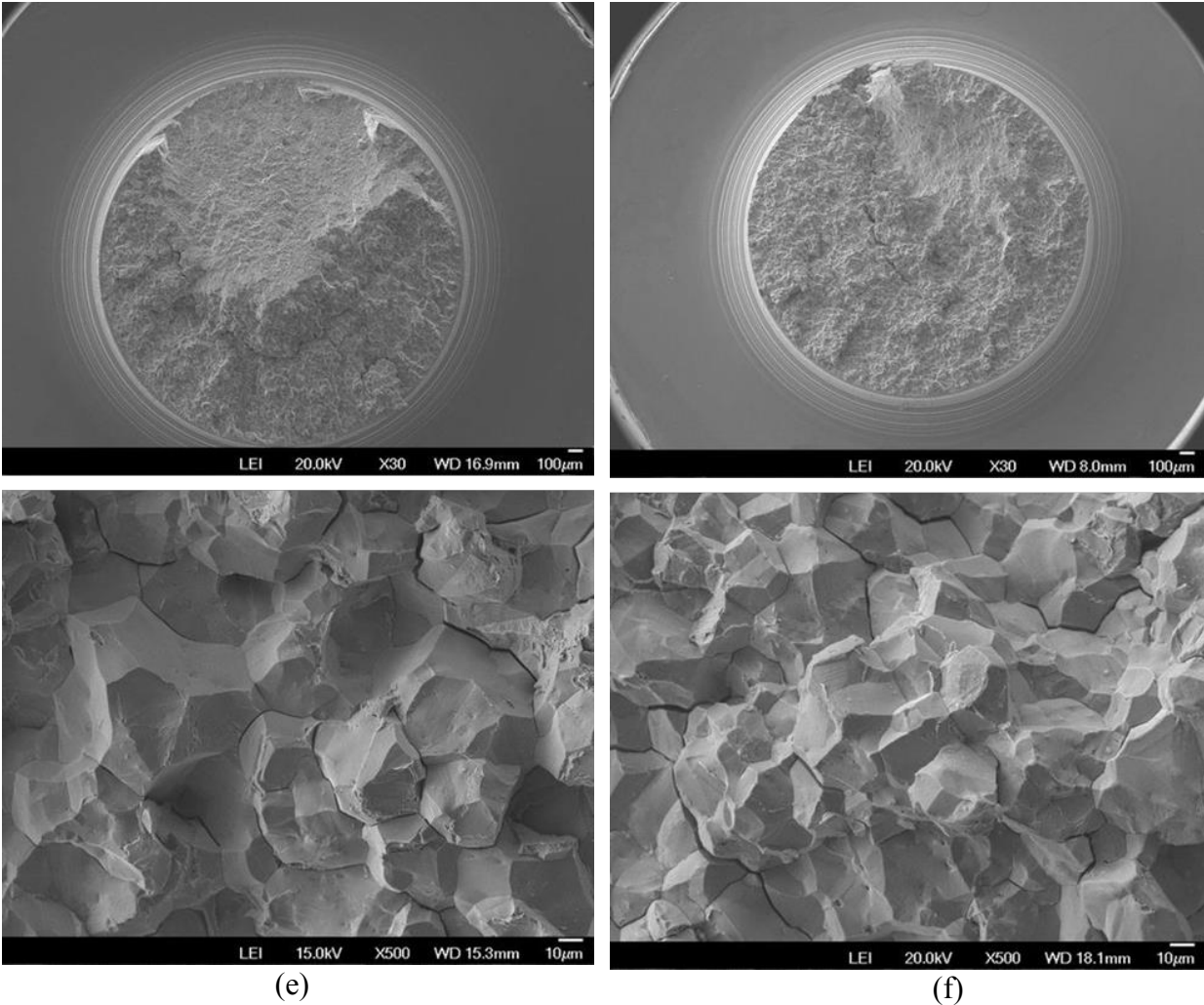


Figure 3.16: SSRT fracture surfaces of aged Monel K-500 material lots in deaerated 0.6M NaCl; above images are (a) Allvac at $-850\text{mV}_{\text{SCE}}$, (b) TR 2 at $-850\text{mV}_{\text{SCE}}$, (c) Allvac at $-950\text{mV}_{\text{SCE}}$, (d) TR 2 at $-950\text{mV}_{\text{SCE}}$, (e) Allvac at $-1100\text{mV}_{\text{SCE}}$, (f) and TR 2 at $-1100\text{mV}_{\text{SCE}}$.

3.2 Microstructure Characterization

Detailed microstructure characterization was done in order to investigate why the Allvac material lots was more resistant to HEAC than TR 1, TR 2, and TR 3. Specifically, the grain size, grain boundary character, alloy composition, impurity content, and impurity distribution were studied.

3.2.1 Orientation Imaging Microscopy

Orientation imaging microscopy (OIM) was completed on each material lot. Sample material was taken from SEN(T) specimens far away from the test gauge. One surface of these samples was then polished, as described in Section 2.8. The crystallographic information of each

grain in a small area (a 225x338 μm rectangle) representative of the overall microstructure was analyzed, as described in Section 2.8, using the electron backscatter diffraction (EBSD) capabilities of the FEI Quanta 650 SEM at 30 kV with a 5 nA probe current. From this analysis, Inverse Pole Figure (IPF) maps were created using analysis software, shown in Figure 3.17. The average crystallographic orientation in each grain is shown by the color of the grain, using the triangle legend in Figure 3.17. The color corresponds to the crystallographic axis normal to the sample surface. For example, a blue grain has the $\langle 111 \rangle$ pole perpendicular to the sample surface [79].

The grain size variation between the material lots is immediately apparent in the IPF maps in Figure 3.17. Using these maps, the average grain size for each material was determined using ASTM E112-3. The average grain size in the Allvac is shown in Table 3.1 to be approximately one-half the grain size of TR 1, TR 2 and TR 3. In all materials, the grains are isometric in shape, with one to four twin boundaries inside each grain. The orientation of each grain appears random, resulting in an isotropic microstructure overall.

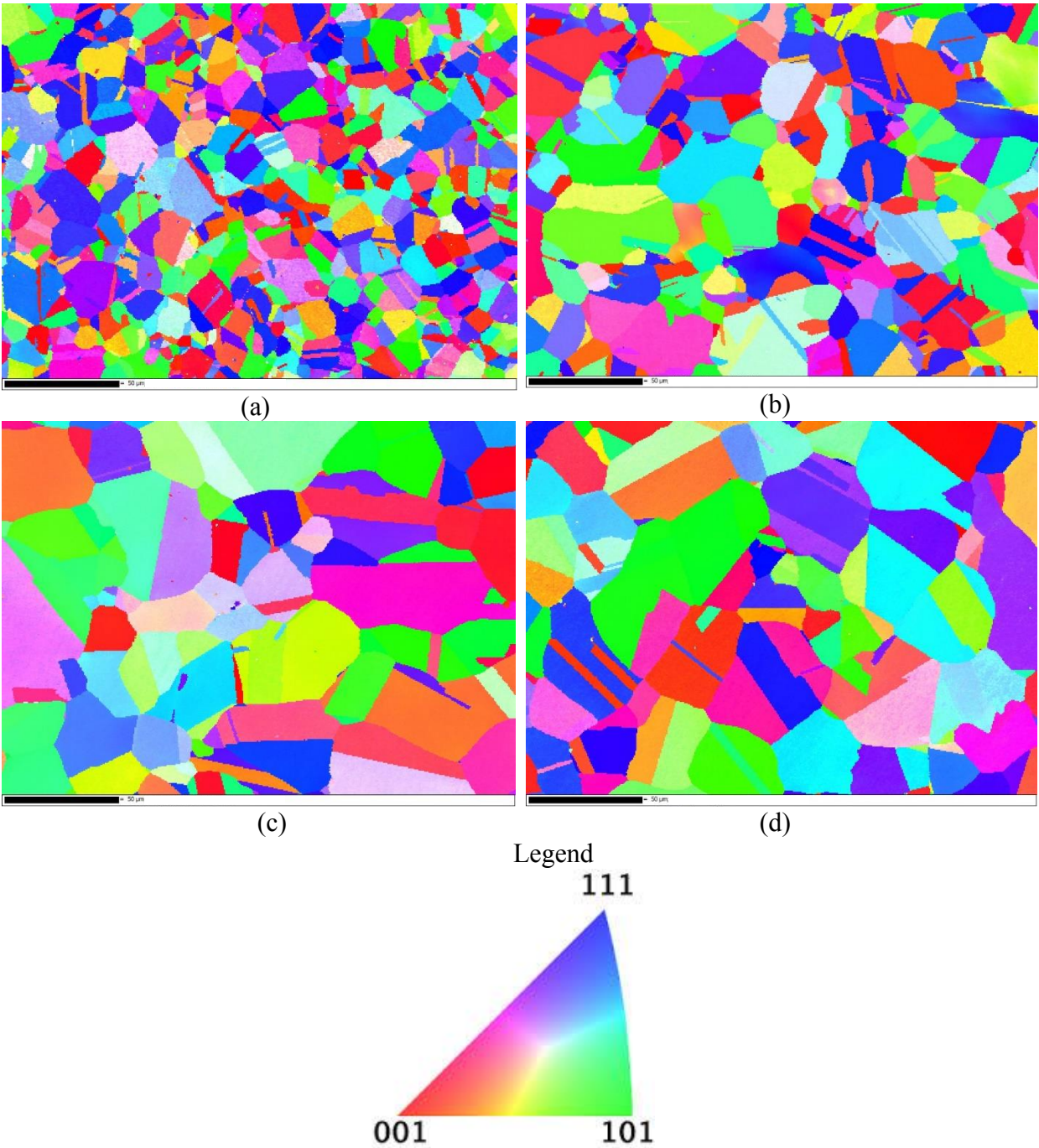


Figure 3.17: Orientation imaging microscopy of the (a) Allvac, (b) TR 1, (c) TR 2, and (d) TR 3 material lots of aged Monel K-500.

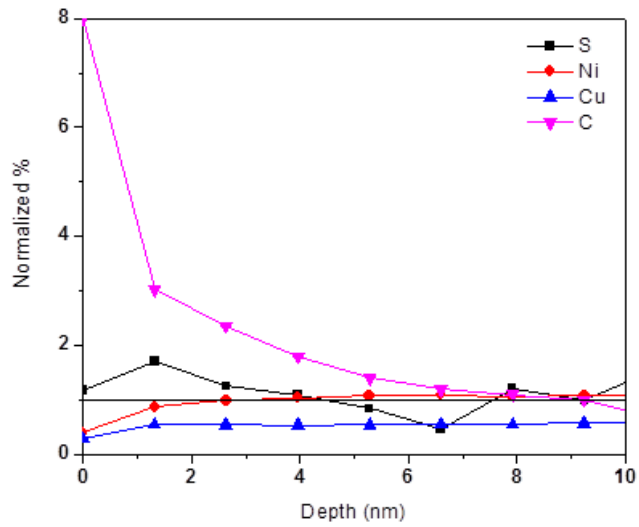
Table 3.1: Average grain size for several heat treatments of aged Monel K-500 calculated from the IPF maps shown in Figure 3.17 according to ASTM E112-3. The margin of error for the 95% confidence interval in the grain diameter measurements is also given.

Material	Average Grain Diameter [μm]	95% Confidence Interval Margin of Error [μm]
Tie Rod 1	25.8	1.6
Tie Rod 2	35.3	1.6
Tie Rod 3	31.8	1.6
Allvac	13.8	1.6

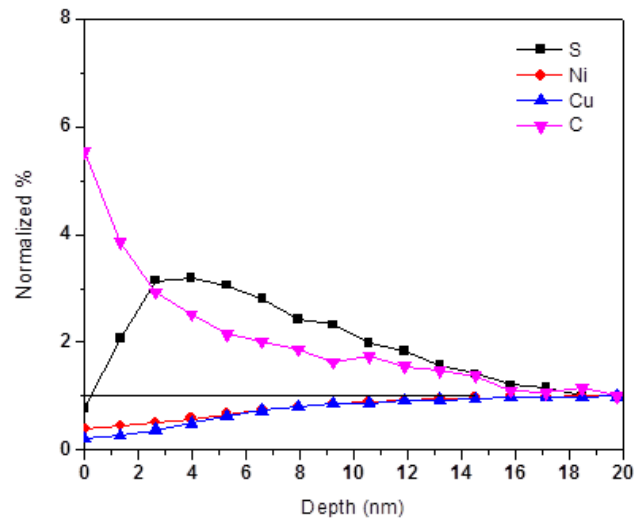
3.2.2 Impurity Segregation at Grain Boundaries

Work in a companion study by J. Scully at UVa on the Allvac and TR 2 Monel K-500 material lots included Auger depth profiling, which was completed on IG facets on available fracture surfaces to investigate possible impurity segregation at the grain boundaries. Of particular interest is sulfur segregation at the grain boundaries, consistent with its impact in GB property degradation [38-41]. The auger analysis was completed on the fracture surfaces created during SSTR testing following charging at $-1100\text{mV}_{\text{SCE}}$ shown in Figure 3.16 and described in Section 3.1.3. The depth profiles were normalized to a depth of 9 nm in the Allvac material and 20 nm in TR 2, where the atomic concentrations are observed to level off and are assumed to have stabilized to near-homogenous levels inside the grain, close to the bulk concentrations given in Table 2.1. Thus, all elements should go to a normalized concentration of 1 in Figure 3.18. Figure 3.18 (b) shows possible sulfur segregation to the grain boundaries evident in TR 2 while no such segregation was observed in the Allvac material lot in Figure 3.18 (a).

The data in Figure 3.18 was collected from one IG facet from each fracture surface. Thus, it is not clear if all the IG facets in TR 2 would show similar sulfur segregation or not, nor is it certain other grain facets in the Allvac material do not have sulfur segregation. However, much smaller grain size in the Allvac material supports the transition from no sulfur segregation in the Allvac material to sulfur segregation in TR 2. This combined with the lower bulk sulfur concentration in the Allvac material compared to TR 2 warrants investigation into lot-to-lot variation in sulfur segregation.



(a)



(b)

Figure 3.18: Grain boundary segregation data via Auger analysis on IG fracture surfaces of (a) Allvac and (b) TR 2 materials.

3.2.3 Hydrogen Behavior in the Microstructure

Dr. Scully, Dr. Hung Ha, and Dr. Brendy Rincón Troconis are investigating lot-to-lot variation in the hydrogen behavior between Allvac and TR 2 materials in a companion study; an excerpt of results pertinent to the current HEAC work is included below. These materials were chosen as they show the most variation in HEAC behavior during fracture mechanics

characterization at $-850\text{mV}_{\text{SCE}}$. Specifically, D_{eff} was measured, $C_{\text{H-Diff}}$ was measured, the hydrogen evolution reaction (HER) kinetics were measured, and the hydrogen trapping behavior was investigated.

The HER kinetics were shown to be similar for Allvac and TR 2 materials. This is important because it demonstrates the hydrogen production reactions at the crack tip or bold surfaces are not a function of material lot. The hydrogen trapping behavior was studied via TDS analysis of thin plate specimens charged at $-850\text{mV}_{\text{SCE}}$. The two most common hydrogen traps in the Monel K-500 microstructure are the Ti-carbides and the γ' (Ni_3Al) precipitates [12]. The very low concentration of Ti-carbides in the matrix preclude them from significantly altering the hydrogen behavior in the material [12, 32]. Therefore, the trapping behavior in Monel K-500 can be narrowed down to the γ' precipitates. The concentration of hydrogen at these trap sites as well as their effect on D_{eff} are a function of the trap binding energy [12]. Therefore, the hydrogen trapping behavior is effectively described using the trap binding energy of the γ' traps. The Allvac and TR 2 materials have statistically similar trap binding energies of 9.9 ± 5.0 kJ/mol and 14.8 ± 5.0 kJ/mol respectively [12]. This similarity is expected since the hydrogen trapping in both materials is dominated by trapping at γ' particles, which should be similar in size and distribution between the material lots [8, 12]. This similar trap binding energies suggest similar trapping behavior is occurring in Allvac and TR 2 material. This suggests the two lots should have similar values for D_{eff} . Indeed, D_{eff} was measured to be near 1×10^{-10} cm^2/s for both material lots, consistent with other measured diffusivities reported in the literature, which typically ranged from 5.0×10^{-11} cm^2/s to 1.3×10^{-10} cm^2/s [8, 12, 28]. This supports the use of one D_{eff} in the HEAC modeling in this project.

The diffusible concentration of hydrogen present in the system $C_{\text{H-Diff}}$ was measured as a function of overpotential, η_{H} , in each material via Barnacle Cell testing following charging at $-850\text{mV}_{\text{SCE}}$, $-950\text{mV}_{\text{SCE}}$, $-1000\text{mV}_{\text{SCE}}$, and $-1100\text{mV}_{\text{SCE}}$. The TR 2 material was charged in 0.6M NaCl while the Allvac material was charged in ASTM artificial ocean water. The key result was that the Allvac material contained less hydrogen ($C_{\text{H-Diff}} = 0.29 - 11.5 \eta_{\text{H}}$) than the TR 2 material ($C_{\text{H-Diff}} = -10.20 - 119.89 \eta_{\text{H}}$) after similar charging times [68]. This corresponds to 2 wppm for the Allvac material and 4 wppm for the TR 2 material at $-850\text{mV}_{\text{SCE}}$ and 3 wppm for Allvac and 17 wppm for TR 2 at $-950\text{mV}_{\text{SCE}}$ [68]. These hydrogen concentration for the Allvac material are

also consistent with Barnacle Cell testing completed on the Allvac material lot in 0.6M NaCl, where concentrations around 5 wppm were reported for charging at $-850\text{mV}_{\text{SCE}}$ and $-950\text{mV}_{\text{SCE}}$ [8]. This suggests that testing in ASTM artificial ocean water did not significantly affect the hydrogen uptake in the Allvac material when compared to testing in 0.6M NaCl. Furthermore, the lower measured hydrogen concentrations in the Allvac material is consistent with the improved HEAC resistance of the Allvac material compared to TR 2 found during HEAC testing at $-850\text{mV}_{\text{SCE}}$. The hydrogen concentration differences between TR 2 and Allvac at $-950\text{mV}_{\text{SCE}}$ would not lead to significant differences in da/dt_{II} between the two material lots since so much hydrogen is being introduced into the FPZ. This is supported by micromechanical modeling done in Section 4.1.2 showing a 100x difference in hydrogen concentration is needed to cause significant differences in da/dt_{II} between two material lots. Such large differences in hydrogen concentration were not measured between TR 2 and Allvac.

4 Discussion

4.1 Pertinent HEAC Fracture Mechanics Testing Results

4.1.1 Effect of Calcareous Deposits on HEAC Kinetics

The beneficial effects of calcareous deposits on the corrosion kinetics on metal alloys under cathodic polarizations has been extensively studied and is attributed to a reduction in the cathodic area, restriction of the diffusion of depolarizers at the cathode, or increasing the ohmic resistance of the system [86-88]. Others have observed increased crack growth due to wedging effects from the presence of the calcareous deposits in the crack wake [89]. The results in Figure 3.6 shows testing in ASTM artificial ocean water lead to significantly slower cracking from $20\text{MPa}\sqrt{\text{m}}$ to $50\text{MPa}\sqrt{\text{m}}$, effectively delaying the onset of Stage II crack growth and increased K_{TH} from $20\text{MPa}\sqrt{\text{m}}$ to $25\text{MPa}\sqrt{\text{m}}$. However, da/dt_{II} did not change significantly between testing in 0.6M NaCl and ASTM ocean water, with values of $1.07 \times 10^{-5}\text{ mm/s}$ and $8.2 \times 10^{-6}\text{ mm/s}$ respectively as measured at $60\text{MPa}\sqrt{\text{m}}$. SEM fractography and EDS analysis shows significant amounts of Ca-rich (Figure 3.7 d, e, f, j, k, and l) and Mg-rich (Figure 3.7 g, h, i, m, n, and o) deposits on the SEN(T) specimen surfaces (Figure 3.7 a, b, and c) during testing in ASTM artificial ocean water.

Determining the effect of the calcareous deposits on the electrochemical mechanisms for HEAC is outside the scope of this project. It is possible the other elements in the ASTM artificial ocean water can influence the crack tip chemistry by altering the pH, buffering the solution, or by promoting the formation and growth of the calcareous deposits on the specimen surface and in the crack wake. The formation of the calcareous deposits may also reduce the surface area on which hydrogen is being produced and adsorbed.

It should also be noted that significant secondary cracking and crack branching was observed during testing in ASTM ocean water. The location of the crack branch is denoted by the blue line in Figure 4.1. The data reported in Figure 3.6 were recorded prior to the development of the crack branching, however it is possible the local driving force may have been influenced at crack lengths prior to the indicated blue line in Figure 4.1. It is not clear whether the presence of the calcareous deposits lead to the secondary cracking, crack branching, or non-straight crack front observed in Figure 4.1.

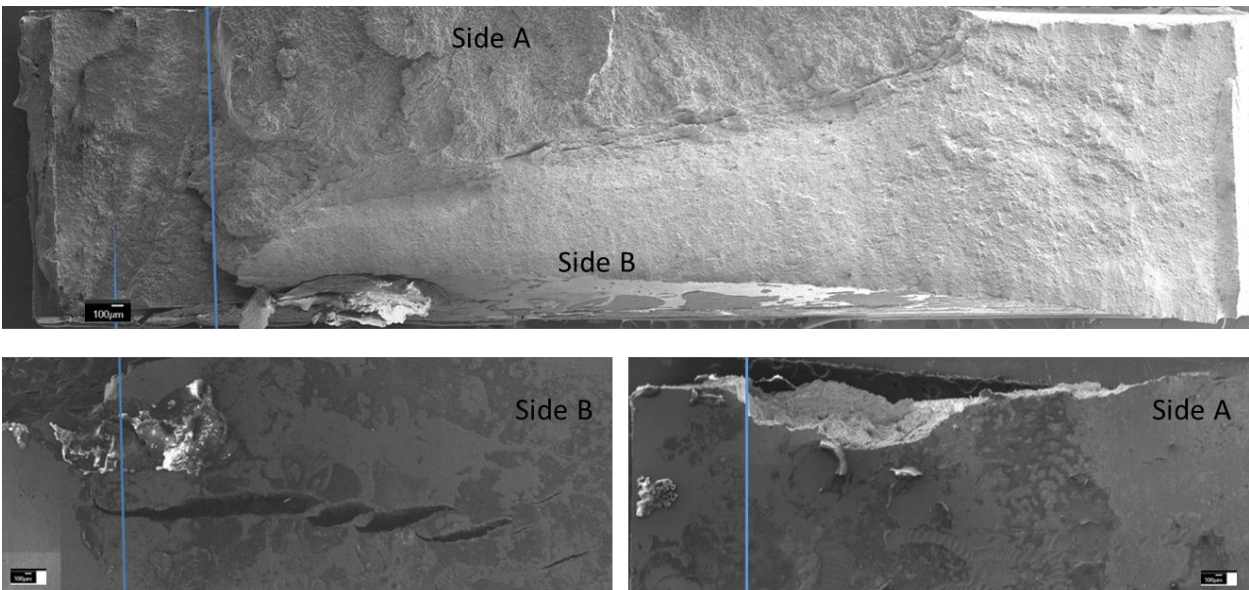


Figure 4.1: SEM images for the fracture surface (top) and bold surfaces (bottom) of an Allvac SEN(T) specimen tested in ASTM artificial ocean water at $-1000\text{mV}_{\text{SCE}}$.

Further testing at other potentials was not carried out in ASTM artificial ocean water. For one, the resulting da/dt vs K data in Figure 3.6 suggests testing in ASTM artificial ocean water may result in non-conservative crack growth and one goal of this project is to measure da/dt vs K data for input into engineering level component lifetime computer models, where

conservative crack growth data is necessary to ensure minimum component lifetime estimates. The random nature of the calcareous deposit nucleation precludes the inclusion of possible beneficial effects of the calcareous deposition on HEAC kinetics in component lifetime estimates. Second, the nucleation and growth of calcareous deposits is nonhomogeneous and it is not clear whether the deposition will occur on every test at every potential studied. This makes testing in ASTM artificial ocean water unattractive for this project, which requires detailed comparison of HEAC kinetics for several material lots of Monel K-500. The main focus of this project is on metallurgical effects on HEAC kinetics, which may be masked by test-to-test variation in calcareous deposit formation and distribution. For all of these reasons, testing was carried out in 0.6M NaCl to investigate the impact of lot-to-lot metallurgical differences on HEAC. Lot-to-Lot HEAC Behavior Differences in Highly Cathodic Environment Testing

At highly cathodic potentials in the range of $-950\text{mV}_{\text{SCE}}$, Allvac, TR 1, TR 2, and TR 3 all expressed similar da/dt_{II} values and pure IG cracking, suggesting the effect of metallurgical lot-to-lot differences is being overpowered by the amount of hydrogen present at the FPZ. However, the high K_{TH} value seen in the Allvac material compared to those of TR 1, TR 2, and TR 3 does suggest that Allvac is the most resistant to the onset HEAC of the four material lots studied, even at highly cathodic potentials. The differences in K_{TH} values for the material lots at $-950\text{mV}_{\text{SCE}}$ may be due to a lower $C_{\text{H-Diff}}$, has recently been shown to be lower in Allvac than in TR 2 in companion study, as discussed in Section 3.2.3. This would lead to a decreased $C_{\text{H}\sigma}$ at the crack tip, increasing the K_{TH} for Allvac according to Equation 1. The difference in K_{TH} may also be due to variation in the sensitivity of the grain boundaries in each material to the concentration of hydrogen at the boundary. This could arise from differences in impurity segregation at the grain boundary [15, 40]. This is discussed in more detail in Section 4.2.4.

The similarities in da/dt_{II} between the material-lots observed at $-950\text{mV}_{\text{SCE}}$ can be understood using the model for da/dt_{II} developed from the HEDE model for final failure. Equation 2 shows that da/dt_{II} is dependent on D_{eff} , x_{crit} , $C_{\text{H}\sigma\text{-crit}}$, and $C_{\text{H}\sigma}$. Recent analysis by Dr. Scully et. al. shows that D_{eff} is close to $1.0 \times 10^{-10} \text{ cm}^2/\text{s}$ for Allvac and TR 2 [68]. Similar diffusivities would be expected for TR 1 and TR 3 since da/dt_{II} did not vary significantly between these material lots and those for Allvac and TR 2. In addition, x_{crit} is assumed to be $1 \mu\text{m}$ for all materials studied as justified from previous stress field analysis and previous modeling on the Monel K-500 Allvac material lot [8, 30]. Thus, da/dt_{II} becomes dependent upon

the $C_{H\sigma-crit}/C_{H\sigma}$ ratio. Previous modeling fit da/dt_{II} data from tests on the Allvac material using Equation 2 to determine $C_{H\sigma-crit}$, resulting in a value of 1100 wppm for $C_{H\sigma-crit}$ [8]. The Auger analysis in Figure 3.17 suggests the tie rod materials have sulfur segregation that is not present in the Allvac material. The effect of the sulfur segregation would be to lower the amount of hydrogen required to cause IG failure, $C_{H\sigma-crit}$ in Equation 2 [15, 40, 41, 43]. The exact effects of sulfur and hydrogen grain boundary segregation are discussed in more detail in Section 4.2.4.1, however combining Equation 22 and Equation 2 through the elimination of $C_{H\sigma}$ yields

$$C_{H\sigma-Crit} = \frac{1}{\alpha} \left(1 - \operatorname{erf} \left\{ \frac{\frac{da}{dt_{II}} x_{crit}}{4D_{eff}} \right\} \right) \left(K_{IG} - \varphi C_S - \sqrt{\ln(K_{TH} \beta') \alpha'' \sigma_{YS}} \right), \quad (20)$$

where φ is the sensitivity of the grain boundaries to sulfur embrittlement and C_S is the sulfur concentration at the grain boundary. The effect of the lot-to-lot differences in hydrogen and sulfur concentration are captured by the da/dt_{II} and K_{TH} data used to predict $C_{H\sigma-Crit}$. It is assumed α and φ does not change lot-to-lot, which may not be the case in reality but is supported by the similar grain boundary character in each material. In order to study the effects of hydrogen and sulfur grain boundary concentration on da/dt_{II} , it is assumed that higher hydrogen and sulfur concentration in TR 1, TR 2, and TR 3 lead to decreases in $C_{H\sigma-Crit}$ on the order of 5x (thus $C_{H\sigma-crit} = 220$ wppm) for TR 1, TR 2, and TR 3. C_{H-Diff} at $-950mV_{SCE}$ is 13 wppm according to Equation 7, which correlates to $C_{H\sigma}$ on the order of 9000 wppm. Then, $C_{H\sigma-crit}/C_{H\sigma}$ is 0.18 for the Allvac material and 0.04 for the three tie rods. This correlates to a model predicted da/dt_{II} of $0.04 \mu\text{m/s}$ for the Allvac material and $0.09 \mu\text{m/s}$ for the tie rods. This exercise demonstrates that for the higher cathodic polarizations (where the C_{H-Diff} is large), a 5X change in $C_{H\sigma-crit}$ due to metallurgical differences results in only a minor change in the HEAC behavior. In order to predict a significant da/dt_{II} increase, such as a 5x increase, between the Allvac material and another Monel K-500 lot, one has to assume $C_{H\sigma-crit}$ for the other material lot is 100x lower than that of Allvac, which is not reasonable given the similarity in microstructure and HEAC behavior observed at $-950mV_{SCE}$ between the materials in this study. Thus, at highly cathodic potentials metallurgical differences are overshadowed by the aggressive nature of the charging environment and high hydrogen concentrations achieved in the FPZ.

4.1.3 Lot-to-Lot HEAC Behavior Differences in Mildly Cathodic Environment Testing

At the near-immunity potential $-850\text{mV}_{\text{SCE}}$, TR 1, TR 2, and TR 3 have K_{TH} values of 16, 32, and 26 $\text{MPa}\sqrt{\text{m}}$ and da/dt_{II} crack growth rates of 1.8×10^{-6} mm/s, 4.4×10^{-6} mm/s, and 3.2×10^{-6} mm/s at a K of 60 $\text{MPa}\sqrt{\text{m}}$ respectively. Fractography in Figure 3.14 revealed IG/TG mixed cracking in TR 1, TR 2 and TR 3 while Allvac was observed to have cracked from a ductile-like failure similar to what occurred during testing in inert environments. Therefore, Allvac is more resistant to HEAC than TR 1, TR 2, and TR 3. This is consistent with (1) lower $C_{\text{H-Diff}}$ measured in Allvac compared to TR 1 and TR 2 measured by Dr. Scully et al., (2) a lack of historical precharging of the specimen (TR1-3 had 5wppm from service exposure), (3) the SSRT results showing enhanced resistance for Allvac compared to TR2, and (4) the Auger results that show a lack of S segregation for Allvac compared to TR2. However, it is not understood what microstructure feature unique to the Allvac alloy system is causing the observed differences in hydrogen behavior.

The bulk alloys compositions for each material lot are similar. This suggests that improved HEAC resistance of the Allvac material is likely not due to an alloy compositional effect, outside of possible impurity effects. The slow ductile crack growth well below K_{IC} of each material was characterized during the inert environment testing. Figure 3.1 shows consistent cracking behavior across all materials, demonstrating that Allvac is not intrinsically tougher than TR 1-3. Furthermore, the similarities in measured Ramberg-Osgood flow constants in Table 2.2 show the increased HEAC resistance of the Allvac material is not due to different strain hardening behavior. Literature review suggested several possible features of the material that may contribute to the observed HEAC behavior differences: H-metal interaction characteristics (diffusivity, uptake, etc.), yield strength, grain size, grain boundary character, and impurity concentration at the grain boundary. A battery of materials characterization analyses were carried out to look at each feature. Lot-to-lot Microstructure Variation and its Effect on HEAC Kinetics

The effect of microstructure characteristics in Monel K-500 is not well understood. The microstructural features of each material lot were compared to the crack growth behavior in an effort to relate the microstructure/ metallurgy and HEAC kinetics.

4.2.1 Effect of Yield Strength

The measured yield strengths for the Allvac, TR 1, TR 2, and TR 3 materials are given in Table 2.2 to be 786 MPa, 898 MPa, 795 MPa, and 793 MPa respectively. The grain size for the Allvac, TR 1, TR 2, and TR 3 materials are given in Table 3.1 to be 14 μm , 26 μm , 35 μm , and 32 μm respectively. Therefore, higher yield strength does not correlate with the decreased grain size, contrary to the Hall-Petch relationship described in Equation 9. This is expected, as the yield strength for Monel K-500 is mainly dependent upon γ' precipitate size and distribution [32].

The yield strength differences will affect the K_{TH} for each material according to Equation 1. The values for α , β , α'' , and K_{IG} have been established in previous work to be 0.56 $\text{MPa}\sqrt{\text{m}}/(\text{atom fraction H})$, 0.26 $\text{MPa}\sqrt{\text{m}}$, 0.00018 MPa m , and 0.675 $\text{MPa}\sqrt{\text{m}}$ respectively [8, 30]. The yield strength (σ_{YS}) for each material is given in Table 2.2. Finally, $C_{\text{H}\sigma}$, will depend upon $C_{\text{H-Diff}}$, which is a function of the applied potential according to Equation 7, and on σ_{YS} according to Equation 5, where σ_{H} is taken to be $12\sigma_{\text{YS}}$ consistent with previous K_{TH} modeling in Monel K-500 and recent strain plasticity gradient modeling [8, 30]. Using potential-specific values of $C_{\text{H-Diff}}$ calculated from Eqn. 7 (note the E vs $C_{\text{H-diff}}$ relationship may vary from lot-to-lot, but this variation is not captured in this exercise) and the appropriate σ_{YS} values (Table 2.2) results in the predicted K_{TH} for each material shown in Figure 4.2.

The model predictions, shown by the solid lines in Figure 4.2, are directionally correct in that it shows the expected trend of decreasing K_{TH} with increasing σ_{YS} . Furthermore, the model reasonably predicts the measured K_{TH} values for TR 1, TR 2, and TR 3. There is no measured K_{TH} reported for Allvac at $-850\text{mV}_{\text{SCE}}$ since the material did not crack due to HEAC, as discussed in Section 3.1.2.3. However, the threshold stress intensity for IG cracking in Allvac must be higher than the stress intensity at which the TG microvoid-based cracking occurred (31 $\text{MPa}\sqrt{\text{m}}$), consistent with the predicted K_{TH} of 39 $\text{MPa}\sqrt{\text{m}}$ at $-850\text{mV}_{\text{SCE}}$. It is not clear why the model predicts lower K_{TH} than what was measured for the Allvac material. This may be an effect of the masking, but that would imply hydrogen produced at the bulk surface somehow affects the cracking behavior, which is supposedly dominated by hydrogen produced at the crack tip due to the much shorter diffusion distances [8]. Nevertheless, the accurate predictions of the

HEAC behavior of each material lot validates the modeling and suggests the yield strength plays an important role in controlling lot-to-lot variation in HEAC behavior.

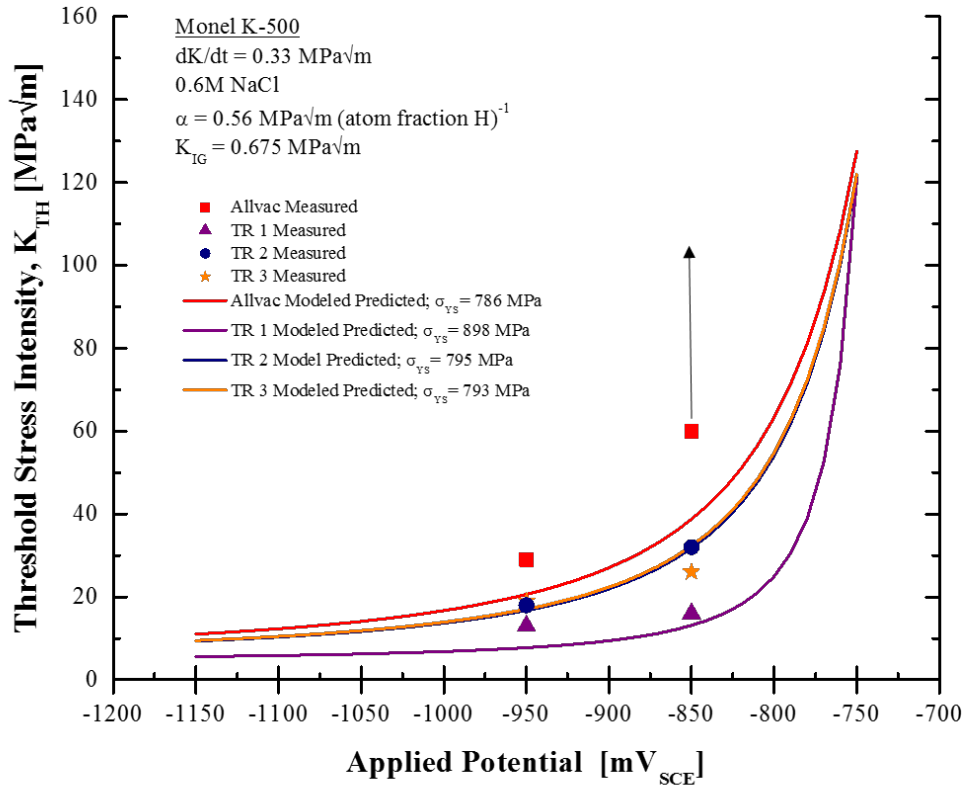


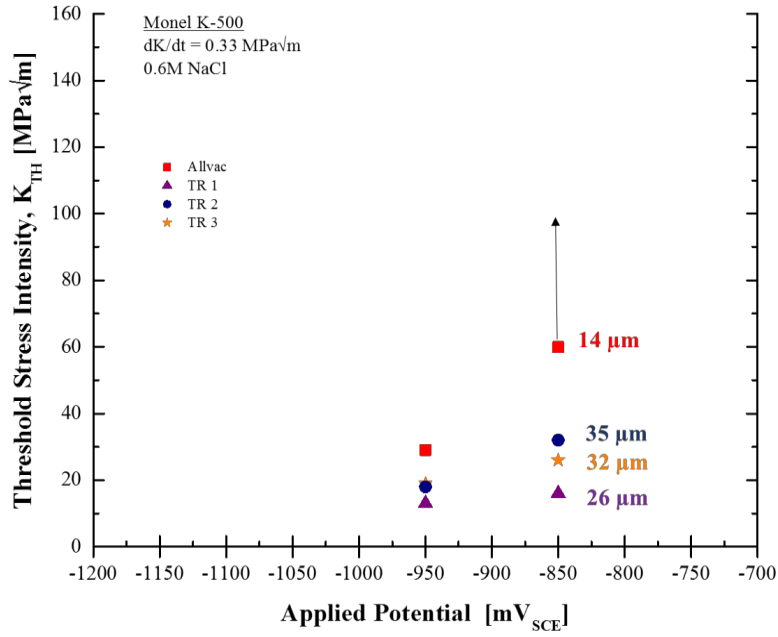
Figure 4.2: Measured K_{TH} and model predicted (Equation 1) K_{TH} for HEAC versus applied potential for four aged Monel K-500 lots. The upward arrow indicates HEAC crack growth did not occur during testing.

4.2.2 Effect of Grain Size

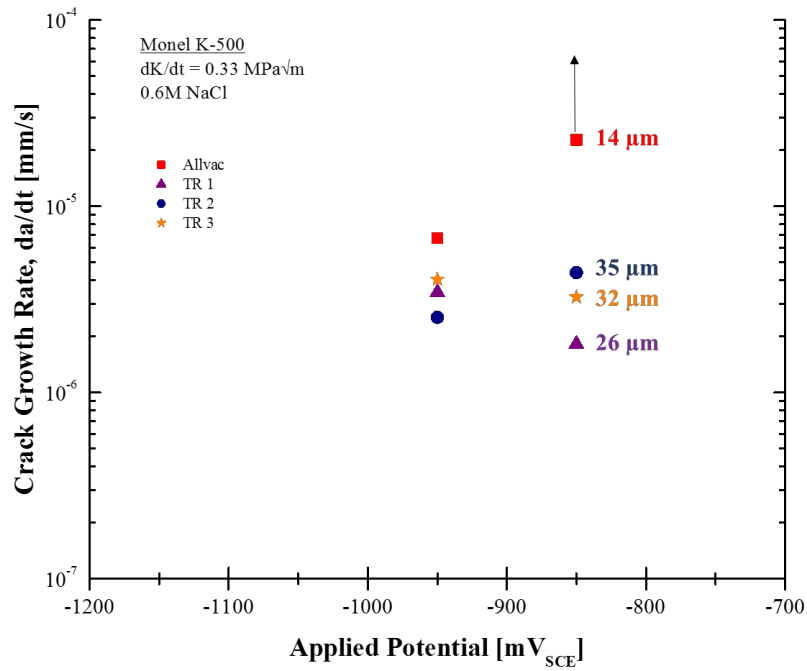
Literature suggests that K_{TH} for HEAC increases with increasing grain size in IN718 and IN903 [11, 35]. However, in both cases, the increased K_{TH} was related to carbide spacing in the matrix. In IN718, the increased K_{TH} was attributed to increased carbide spacing in the microstructure rather than the increased grain size [11]. Crack advance during Environment Assisted Cracking (EAC) of IN718 was a mixture of microvoid, IG, and slip based cracking.

The carbide spacing impacted the crack growth rate since the microvoids nucleate at carbide, matrix interfaces along the projected crack path [11]. Thus, when the carbide spacing increased with increasing grain size, the characteristic distance governing fracture toughness increased. Similarly, the increased K_{TH} with increasing grain size trend observed in IN903 was attributed to a similar increase in critical distance for IG fracture, which increased with increasing grain size[35]. In the case of Monel K-500, no microvoid cracking is expected when HEAC is active. Therefore, HEAC fracture toughness is not related to carbide spacing in this alloy. For pure nickel, the resistance to hydrogen embrittlement increased with increasing grain size, measured as an increase in ductility with increasing grain size [36]. This was attributed to an increasing fraction of low energy “special” boundaries as a function of increasing grain size. The effect of grain boundary character is discussed in more detail in Section 4.2.3.

The effect of grain size on the HEAC behavior observed in this project are shown in Figure 4.3. At the near-immunity potential of $-850mV_{SCE}$, TR 1, TR 2, and TR 3 have K_{TH} values of 16, 32, and 26 $MPa\sqrt{m}$ and grain sizes of 26, 35 and 32 μm respectively. Also, at $-950mV_{SCE}$ the K_{TH} values were 29, 13, 18, and 19 $MPa\sqrt{m}$ for the Allvac, TR 1, TR 2, and TR 3 materials. Though the differences in HEAC behavior between TR 1, TR 2, and TR 3 are slight, they generally follow a weak trend of increasing K_{TH} with increasing grain size at near immunity potentials and at aggressively cathodic potentials consistent with literature findings, while Allvac is the outlier in both potential regimes. Finally, the da/dt_{II} crack growth rates for TR 1, TR 2, and TR 3 were 1.8×10^{-6} , 4.4×10^{-6} , and 3.2×10^{-6} mm/s respectively at $-850mV_{SCE}$ and 3.4×10^{-6} , 2.5×10^{-6} , and 4.1×10^{-6} mm/s respectively at $-950mV_{SCE}$. Again the HEAC differences observed between the three tie rod materials are slight, but in the near threshold potential range, da/dt_{II} was observed to increase with increasing grain size for TR 1, TR 2, and TR 3. This trend is not observed at more cathodic potentials, where the aggressive charging environment is likely overshadowing the secondary effects of grain size on HEAC kinetics.



(a)



(b)

Figure 4.3: (a) K_{TH} and (b) da/dt_{II} at applied potentials of -850mV_{SCE} and -950mV_{SCE} and their relation to grain size.

It is difficult to fundamentally explain the rise in K_{TH} and da/dt_{II} with increasing grain size observed in Figure 4.3 because several microstructure features are altered by increases in grain size. In addition, the exact heat treatments of the TR 1, TR 2, and TR 3 material lots are unknown, preventing consideration of different heats and the effects this would have on the alloy microstructure. Using the framework of Equation 1 as a basis, several effects associated with grain size can be evaluated; specifically the influence of grain size on the slip behavior which can influence the grain boundary stress state (and therefore $C_{H\sigma}$), the effect of crack deflection, the effect of grain boundary connectivity, and the effect of impurity segregation may all change with grain size. The influence of σ_{YS} has already been shown in Section 4.2.1 to correlate with the K_{TH} results. However, assuming the differences in HEAC behavior observed in Sections 3.1.2.2 and 3.1.2.3 is simply a result of yield strength variation is speculative as no direct evidence of variation in slip damage along IG facets was observed between the material lots. Therefore, the effects of crack deflection, grain boundary connectivity, and impurity segregation must also be considered.

4.2.2.1 Effect of Crack Deflection

One possible consequence of grain size may be to increase the amount of crack deflection, making the crack path more tortuous as it progresses through the microstructure. The effect of crack deflection was analyzed using the EBSD maps showing only random, high angle boundaries for each material lot as these grain boundaries are the most susceptible to hydrogen embrittlement and therefore represent the most likely path for crack advance through the microstructure [37, 53]. The geometry of the crack deflection is given by comparing the orientation and lengths of the deflected crack segment, D , and the straight segment, S , defined in Figure 1.1. It should be noted that this model assumes the same amount of deflection is occurring throughout the specimen width for the entire crack front. In reality, the deflection across the crack front will be dispersed randomly as different sections of the crack front travel through different grain boundaries. However, this model will give the maximum effect crack deflection can theoretically have on the applied K . Average D and S values were measured from the random, high angle boundary maps and are shown for each material lot in Table 4.1. The amount of deflection is described by the K_{DEF}/K ratio, with a K_{DEF}/K of 1 relating to a θ_D of 0° , meaning a straight crack. Maximum deflection would occur at the maximum θ_D for a given D and S combination. The maximum θ_D found in the microstructure was 60° . The maximum

amount of deflection are similar for all materials, with K_{DEF}/K values of 0.82, 0.82, 0.77, and 0.81 for Allvac, TR 1, TR 2 and TR 3 respectively. The material with the largest grain size, 35.3 μm for TR 2, showed the most deflection. However, the other material lots did not show increasing deflection with increasing grain size, with similar deflection being observed for grain sizes ranging from 13.8 for Allvac to 31.8 μm for TR 3.

During the analysis, θ_D was determined to range between 0° and 60° in all material lots analyzed. The HEAC K_{TH} measured during fracture testing were then adjusted to account for crack deflection using Equation 11 and are shown in Table 4.1 for θ_D of 0° , 15° , 30° , 45° , and 60° . Increasing deflection angle led to decreasing effective stress intensity and decreasing HEAC kinetics, consistent with prior investigations of crack deflection in aluminum alloys [65, 66]. The cracking threshold stress intensity for Allvac at -850mV_{SCE} was not included in the analysis since cracking was not intergranular and failure was not due to hydrogen embrittlement.

Each material lot's adjusted HEAC K_{TH} at applied potentials of -850mV_{SCE} and -950mV_{SCE} is shown in Table 4.1. In all the materials, accounting for crack deflection resulted in a 0-13% reduction in the measured K_{TH} , the maximum reduction occurring for a crack deflection of 60° . At -850mV_{SCE} no two lots share common K_{TH} values even when assuming no crack deflection in one material and the maximum observed crack deflection of 60° in another lot. In addition, the K_{TH} of Allvac at -950mV_{SCE} is more than twice that of TR 1 and around 50% higher than TR 2 and TR 3 under identical polarization potential. The lot-to-lot differences in HEAC behavior are too large to be due to crack deflection alone. Therefore, crack deflection differences cannot explain the lot-to-lot differences in K_{TH} measured during testing.

Table 4.1: (a) Typical D and S values taken from analysis of each material lot microstructure and (b) adjusted HEAC K_{TH} for a deflected crack of angle θ_D in each material lot measured during fracture testing at -850mV_{SCE} and -950mV_{SCE}.

	Allvac	TR 1	TR 2	TR 3
D [μm]	10.5	17.6	23.2	24.1
S [μm]	10.8	18.3	14.0	23.4

(a)

θ_D [$^\circ$]	Adjusted K _{TH} at -850mV _{SCE} [MPa $\sqrt{\text{m}}$]				Adjusted K _{TH} at -950mV _{SCE} [MPa $\sqrt{\text{m}}$]			
	Allvac	TR 1	TR 2	TR 3	Allvac	TR 1	TR 2	TR 3
0	N/A	16	32	26	29	13	18	19
15	N/A	16	32	26	29	13	18	19
30	N/A	15	31	25	28	13	17	18
45	N/A	15	29	24	27	12	16	18
60	N/A	14	27	23	25	11	15	17

(b)

4.2.2.2 Effect of Slip Pile-up

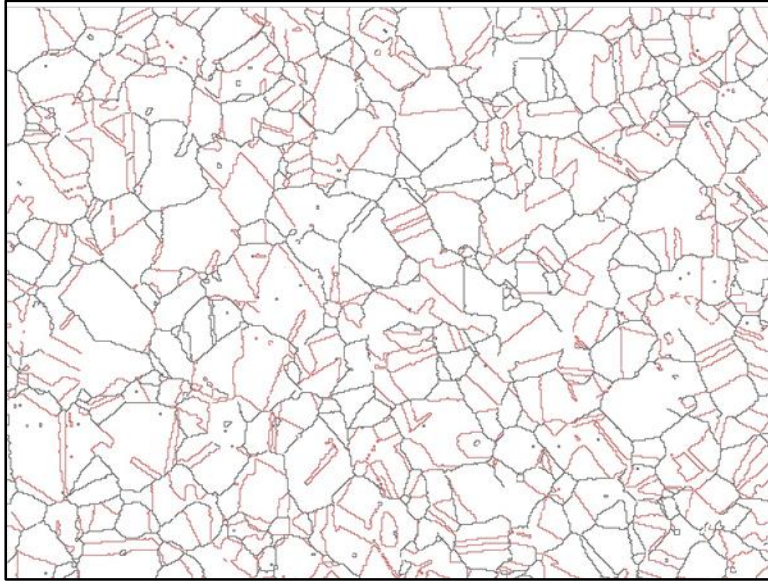
Grain size may influence the dislocations that build up at the grain boundary; specifically, the pile-up increasing with increasing grain size [24, 90, 91]. Researchers have argued that an increase in grain size would increase the local strain hardening due to the increased plastic damage at the grain boundary associated with the increased pile-up [91, 92]. This could enhance HEAC through either (1) an increased driving force for hydrogen diffusion towards the grain boundary resulting from the increased stress disparity between the grain boundaries and grain interior with increased grain size, (2) possibly increasing the amount of hydrogen transport by increasing the number of dislocation traveling to the grain boundary, or (3) an enhanced stress state due to work-hardening [24, 93]. Each of these would have the cumulative effect of increasing $C_{H\sigma}$ in the FPZ for a given C_{H-Diff} . This effect could in part be quantified by altering the σ_{YS} - σ_H relationship to include a parameter (γ) that describes the effect of grain size on local hardening and models the change in $C_{H\sigma}$ necessary to cause the differences in HEAC behavior observed at -850mV_{SCE}:

$$\sigma_H = \gamma \cdot 12\sigma_{YS}. \quad (21)$$

It is possible that the increased HEAC resistance of the Allvac material is due to the smaller grain size leading to decreased local hardening at the grain boundary and reducing C_{HG} . However, no obvious evidence of decreased slip damage at the grain boundaries was observed in the Allvac material compared to TR 1, TR 2, and TR 3, where similar slip densities and slip heights were observed across all material lots during the fractography analysis in Figure 3.10 and Figure 3.11. However, a thorough comparison of slip behavior at the grain boundaries would require detailed imaging of the sub-surface dislocation structure of the crack wake, which is outside of the scope of this effort.

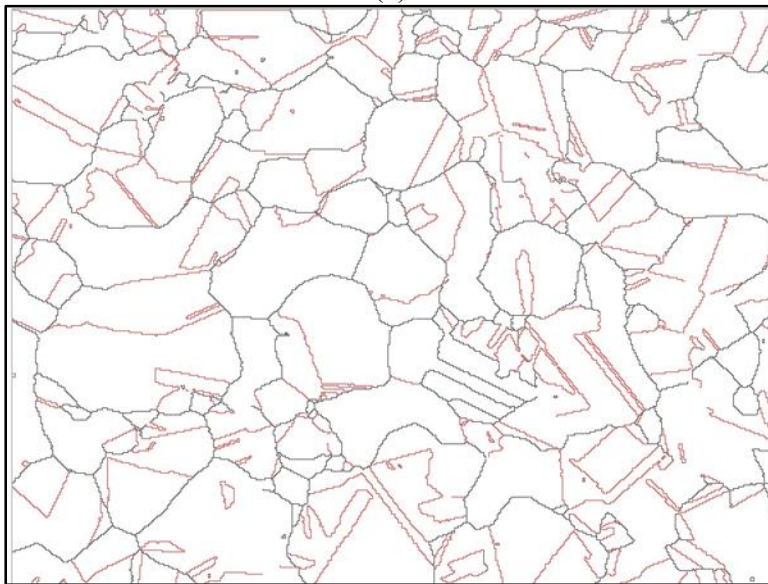
4.2.3 Effect of Grain Boundary Connectivity

Hydrogen embrittlement can be significantly reduced by reducing the fraction of random, high angle grain boundaries through the introduction of low energy “special” grain boundaries [16]. The special boundaries are those with low misorientation angles, θ , below 15° or those that have unique misorientation angles corresponding to CSL boundary geometries. The grain boundary character for each material lot was characterized via OIM microscopy and subsequent data analysis described in Section 2.8. The resulting maps, see Figure 4.4, show the majority of grains in all materials consist of random, high angle grain boundaries with two to three $\Sigma 3$ {111} boundaries internal to the grain.



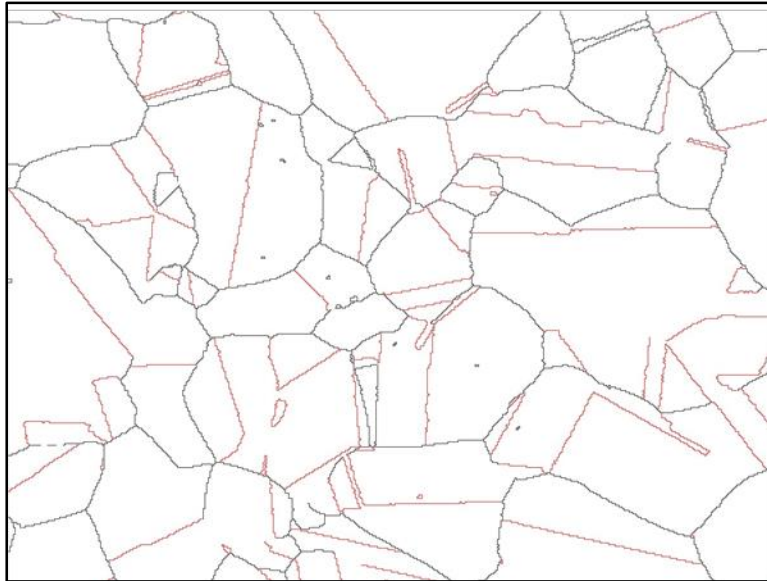
Allvac

(a)



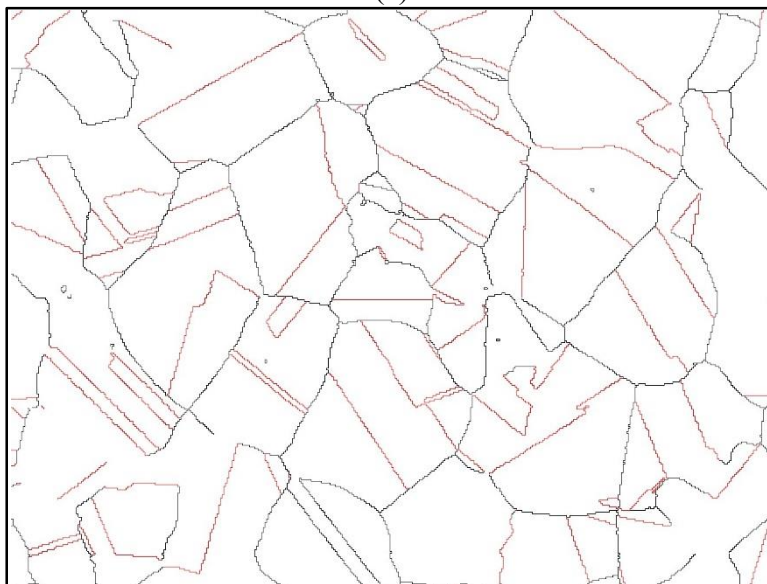
TR 1

(b)



TR 2

(c)



TR 3

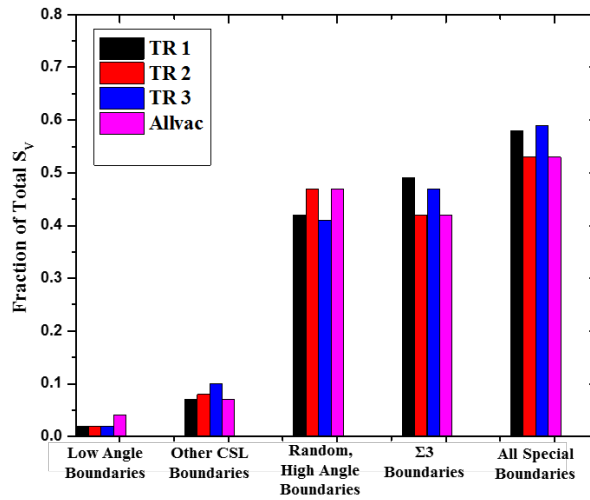
(d)

Figure 4.4: Grain boundary character of each material lot. Black lines are random, high angle boundaries. Red line are Sigma 3 boundaries.

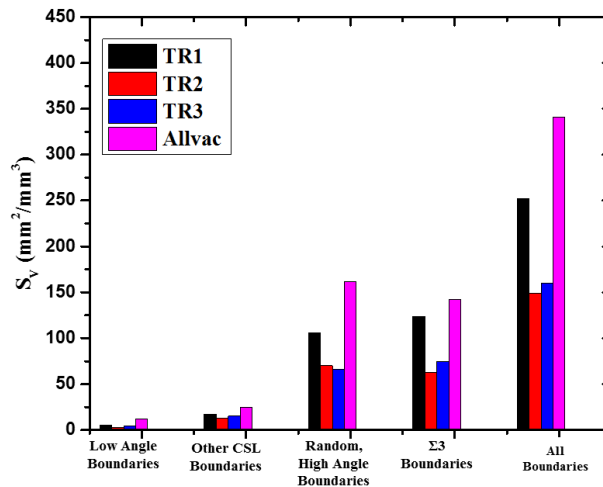


Figure 4.5: Map of $\Sigma 3$ boundaries in TR 1 used to calculate S_v with the test lines overlaid for analysis.

HEAC requires a connected network of grain boundaries susceptible to hydrogen embrittlement. These susceptible boundaries are known to be the random, high angle boundaries [16, 53, 55]. Therefore, researchers have argued that increasing the fraction of special grain boundaries in a system should increase the HEAC resistance of the alloy. From the grain boundary maps in Figure 4.4, the total surface area per volume (mm^2/mm^3), S_v , can be calculated using the simple formula $S_v = 2P_L$, where P_L is the number of intersection of grain boundary type per unit length of test line [94]. For example, to find S_v for the $\Sigma 3$ boundaries, a map showing only the $\Sigma 3$ boundaries is constructed using the OIM data analysis software Tango. Test lines are then laid over that map, as shown in Figure 4.5. P_L was calculated for each line and then averaged to determine S_v . Literature suggests that microstructures with greater fractions of special boundaries should have increased resistance to HEAC [36, 37]. However, Figure 4.6(a) shows consistent fractions of special boundaries in each material, as normalized by the total surface area per volume of all boundaries in the microstructure. Therefore, grain boundary character alone cannot be the cause of the greater HEAC resistance observed between the Allvac material and TR 1, TR 2, and TR 3.



(a)

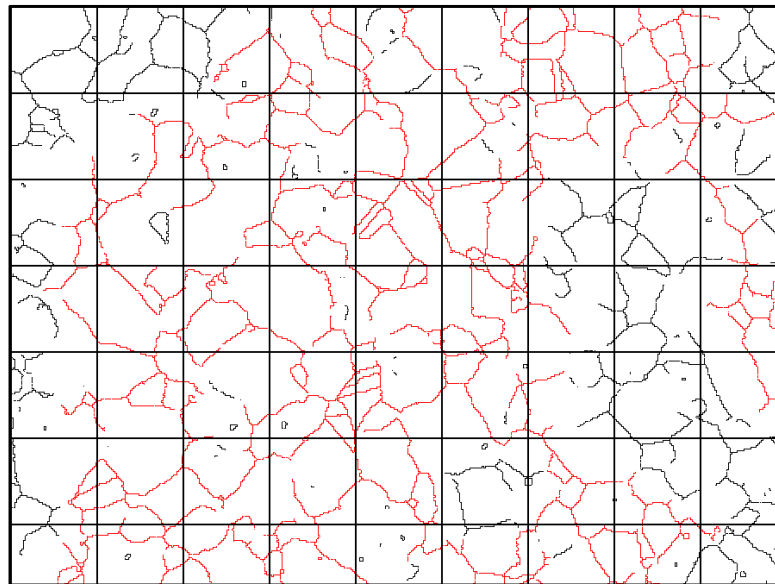


(b)

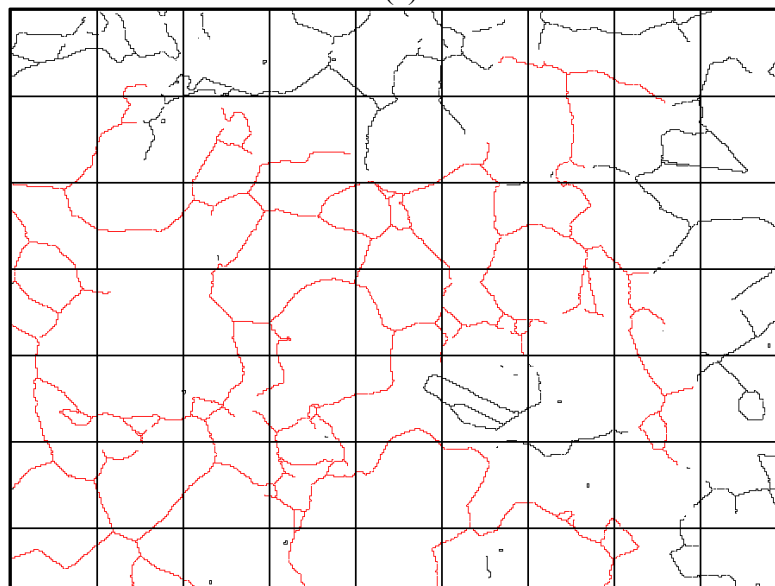
Figure 4.6: Grain boundary character in each material lot studied given as (a) fraction of total grain boundary area per volume and (b) total grain boundary area per volume

Since the grain size of the Allvac material is smaller than the grain size in the tie rod materials, the total surface area per volume of all boundary types is much higher in the Allvac material than in the tie rods, as evident in Figure 4.6(b), including each type of special boundary. It is possible that the greater concentration of low energy boundaries in the microstructure leads to increased resistance to HEAC in the Allvac material. This will occur only if the special boundaries are replacing random, high angle boundaries, lowering the connectivity of the

random, high angle boundaries rather than simply introducing more $\Sigma 3$ twins inside each grain. A quantitative analysis of the connectivity of each material's random, high angle boundary maximum conductivity network (MCN) was completed and is described in Section 2.8. The MCN of each material is shown in red in Figure 4.7.



(a)



(b)

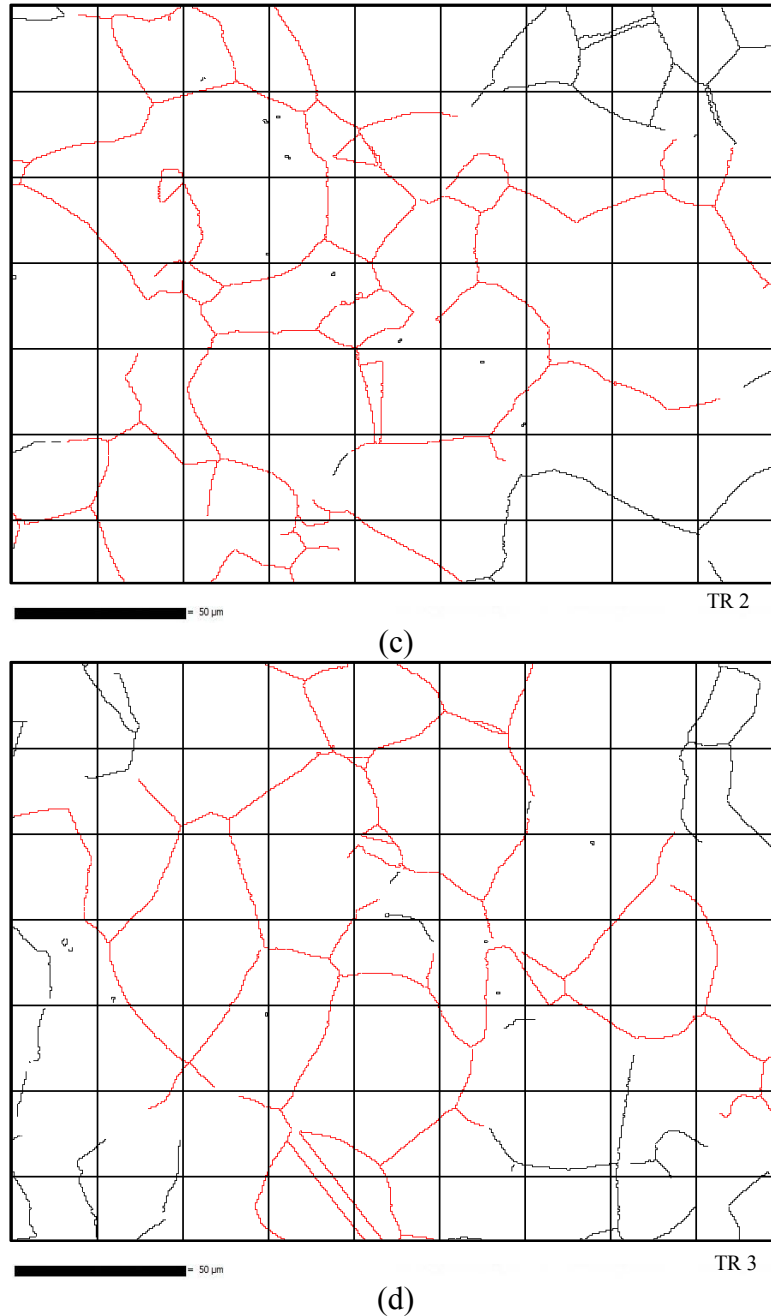


Figure 4.7: The maximum connectivity network (MCN) of the random, high angle boundaries are shown in red for the (a) Allvac, (b) TR 1, (c) TR 2, and (d) TR 3 material lots. The images are overlaid with a 25 μm grid, which was used to count N for the connectivity analysis.

The fractal dimension was then measured, yielding values of 1.59, 1.53, 1.38, and 1.35 for Allvac, TR 1, TR 2, and TR 3 respectively. Therefore, the Allvac material has the highest conductivity of random, high angle boundary. If grain boundary connectivity alone was the

governing factor then this would imply that Allvac is the most susceptible to HEAC, which is opposite to what was observed during fracture testing at $-850\text{mV}_{\text{SCE}}$. Increasing D_R , and therefore increasing connectivity of high angle, random boundaries, does not correlate to increased susceptibility to HEAC in any of the materials studied. There is no relationship or trend evident between random, high angle boundary connectivity and HEAC behavior in the materials studied in this project.

4.2.4 Effect of Impurities

Grain boundary segregation investigation of TR 2 and Allvac materials in Figure 3.18 suggests the increased HEAC resistance of the Allvac material compared to TR 1, TR 2, and TR 3 may be due to sulfur segregation along the grain boundaries present in the tie rods that is not present in the Allvac microstructure. Sulfur segregation is known to decrease the critical hydrogen concentration necessary to cause IG cracking in high purity Ni alloys [39]. A similar effect of sulfur is expected for Ni alloys such as Monel K-500. For this to explain the increased HEAC resistance of Allvac over all three tie rod materials, then similar Auger depth profiling of TR 1 and TR 3 should also show sulfur segregation at the grain boundary.

Attempts were made to complete the study in this project on IG fracture surfaces produced from the HEAC fracture mechanics testing. The results of the depth profiling were hindered by significant carbon and oxide coverage on the fracture surface due to exposure to the atmosphere in the time between the fracture surface being formed and the Auger analysis. The same issue occurred in the Auger analysis of the SSRT specimens discussed in Section 3.2.2, however surface contamination occurred to an even greater extent on the fracture mechanics samples. The exposure to atmosphere was unavoidable as the Auger analysis could not be completed in the same location as the HEAC fracture mechanics testing. The depth profile of on an IG facet of a TR 3 fracture surface is shown in Figure 4.8, where the carbon concentration does not stabilize to a constant value, at around 8 atomic %, until roughly 120 nm penetration. This concentration is much higher than the bulk concentration of TR 3 in Table 2.1, which corresponds to 0.661 atomic % C. Depth profiles in other locations of the TR 3 fracture surface as well as on all other fracture surfaces analyzed show similarly high carbon and oxygen concentrations that decrease with increased depth penetration but do not completely dissipate to alloy concentrations shown in Table 2.1. This strongly suggests the Auger analysis is sampling

the surface contamination on top of the fracture surface rather than the alloy microstructure itself. Thus, it remains uncertain whether the TR 1, TR 2, and TR 3 materials suffer from sulfur segregation along the grain boundaries not present in the Allvac material.

While these data are inconclusive and did not provide results, the data from Figure 3.16 suggest differences in sulfur segregation exist at least between the Allvac and TR 2 materials. Furthermore, the smaller grain size in the Allvac material (and therefore higher area per volume of grain boundary) suggests less sulfur segregation would occur in the Allvac material since the bulk concentration of sulfur diffuses and is spread out over a greater area of grain boundary. Finally, the trace element analysis in Table 2.1 shows Allvac has a lower bulk concentration of sulfur than the other material lots, which could lead to lower concentrations of sulfur at the grain boundary. Previous in situ Auger analysis of IG facets in high purity nickel containing a bulk sulfur concentration of 20 wppm did not reveal any resolvable sulfur concentration peaks at the grain boundary [16]. However, this may have been due to the final heat treatment at 1173 K for the material in this study, where the equilibrium sulfur concentration is negligible in a high purity nickel system as the sulfur become completely soluble in the matrix at such high temperatures [95-97]. Conversely, the final heat treating stage for Monel K-500 material lots in this study likely involved a temperature hold around 755 K followed by air cooling. At this temperature, sulfur segregation may be possible, supported by the occurrence of sulfur segregation following aging at 873K in a Ni-10 Cu binary alloy [95]. All of this evidence suggests that sulfur segregation may play an important role in controlling the lot-to-lot variation in HEAC behavior

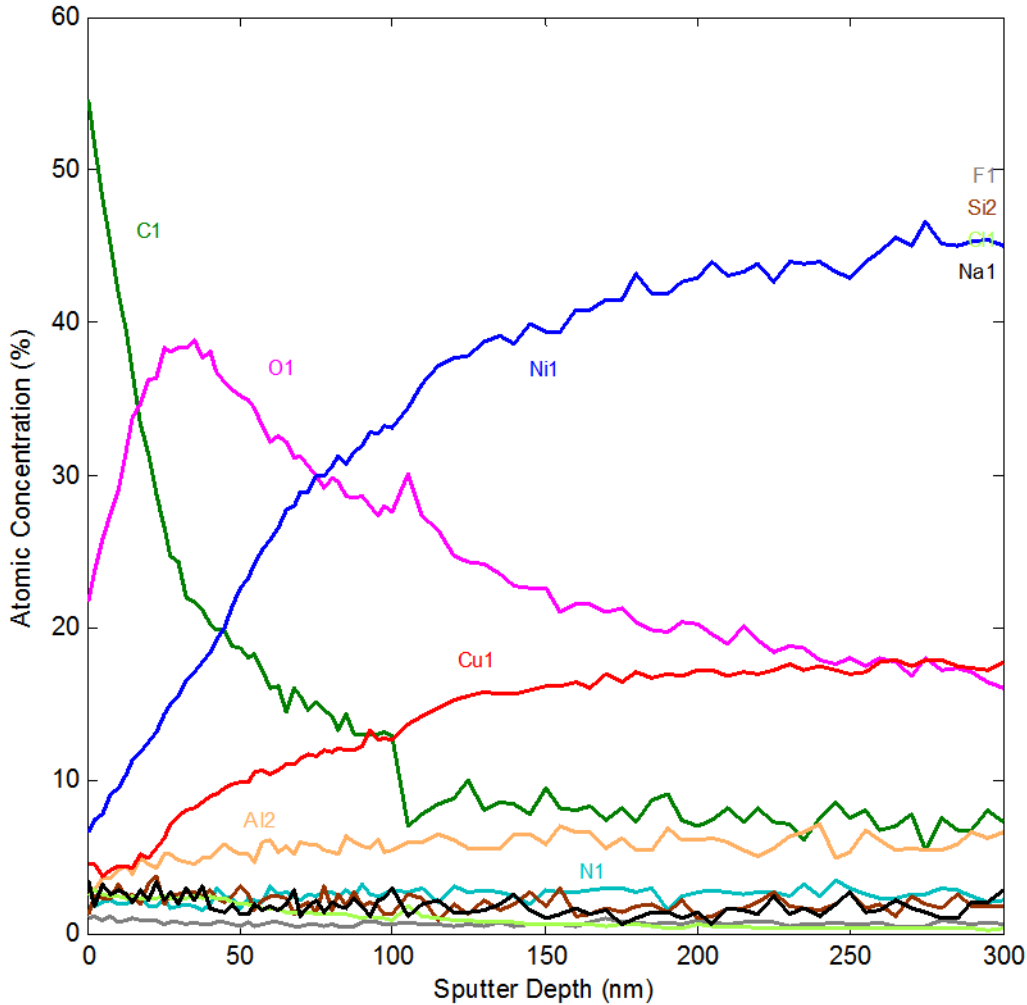


Figure 4.8: Atomic concentration depth profile on an IG facet of the TR 3 material lot showing extensive surface contamination, which hindered the investigation of impurity segregation along the grain boundaries in the material microstructures.

4.2.4.1 Effect of Lot-to-Lot Variation in Sulfur Segregation on HEAC K_{TH}

In order for sulfur segregation to explain the increased HEAC resistance of Allvac compared to the three tie rod materials, then sulfur segregation must be present TR 1 and TR 3 similar to what was measured in TR 2 via the Auger spectroscopy in Figure 3.18(b). The effect of sulfur segregation on the measured K_{TH} can be estimated by adding a parameter describing the grain boundary sensitivity to sulfur embrittlement to Equation 1. Assuming the embrittlement due to sulfur and hydrogen are additive yields

$$K_{TH} = \frac{1}{\beta'} \exp \left[\frac{(K_{IG} - \phi C_S - \alpha C_{H\sigma})^2}{\alpha'' \sigma_{YS}} \right], \quad (22)$$

where ϕ is the reduction of K_{IG} per atom fraction of sulfur [$\text{MPa}\sqrt{\text{m}}/(\text{atom fraction S})$], C_S is the concentration of sulfur [atom fraction S], and the other terms have the same meaning as in Equation 1. The assumption that sulfur embrittlement and hydrogen embrittlement are additive when both S and H are present at the grain boundary is consistent with previous modeling on the effect of impurity (phosphorous) segregation on the hydrogen embrittlement of a 5 percent Ni high strength steel [98]. However, researchers suggest that the effect of S and H embrittlement are *at least* additive when they occur simultaneously and may be synergistic [40, 41, 98]. While it is possible that S and H embrittlement are synergistic in nature, this project assumes the effects are only additive.

Trace element analysis in Table 2.1 shows the bulk S concentration for Allvac, TR 1, TR 2, and TR 3 is 1.6 wppm, 3.1 wppm, 11.0 wppm, and 12.0 wppm respectively. It is assumed no sulfur segregation occurs in the Allvac material, consistent with the Auger spectroscopy in Figure 3.18(a), and sulfur segregation does occur in TR 1, TR2, and TR 3, consistent with Figure 3.18(b) and the decreased HEAC resistance of the three tie rod materials. Previous study on sulfur segregation in Ni-10 Cu binary alloy observed a grain boundary sulfur concentration on the order of 1000x of the bulk sulfur concentration [95]. Assuming a similar sulfur segregation profile in TR 1, TR 2, and TR 3 yields grain boundary sulfur concentrations of 3100 wppm, 11,000 wppm, and 12,000 wppm for TR 1, TR 2, and TR 3 respectively. Since it is assumed no sulfur segregation is occurring in the Allvac material, the sulfur concentration is equivalent to the bulk sulfur concentration for this material, 1.6 wppm. Current modeling will employ values for β' (0.26 $\text{MPa}\sqrt{\text{m}}$), α'' (0.00018 MPa m), and K_{IG} (0.675 $\text{MPa}\sqrt{\text{m}}$) proposed for the Allvac material in previous work [8, 30]. The yield strength (σ_{YS}) for each material is given in Table 2.2. Finally, $C_{H\sigma}$, will depend upon C_{H-Diff} , which is a function of the applied potential according to Equation 7, and of σ_{YS} according to Equation 5, where σ_H is taken to be $12\sigma_{YS}$ consistent with previous K_{TH} modeling in Monel K-500 and recent strain plasticity gradient modeling [8, 30]. Then, if the K_{TH} is known for one material at two applied potentials, α and ϕ can be solved for simultaneously.

For TR 2, K_{TH} is given in Section 3.1 to be 32 MPa√m at -850mV_{SCE} and 18 MPa√m at -950mV_{SCE}. Algebraic manipulation of Equation 22 yields

$$\varphi = \frac{K_{IG} - \alpha C_{H\sigma}^{-850mV} - \sqrt{\alpha'' \sigma_{YS} \ln(K_{TH}^{-850mV} \beta')}}{C_S} \quad \text{and} \quad (23)$$

$$\alpha = \frac{\sqrt{\alpha'' \sigma_{YS} \left(\sqrt{\ln(K_{TH}^{-950mV} \beta')} - \sqrt{\ln(K_{TH}^{-850mV} \beta')} \right)}{C_{H\sigma}^{-850mV} - C_{H\sigma}^{-950mV}}. \quad (24)$$

According to Equation 7, C_{H-Diff} is 5.9 wppm at -850mV_{SCE} and 12.8 wppm at -950mV_{SCE}. Inserting these values into Equations 23 and 24 yields 0.50 MPa√m/(atom fraction H) for α and 0.64 MPa√m/(atom fraction S) for φ . These results suggest that the grain boundary is equally sensitive to S embrittlement as it is to H embrittlement; i.e. a similar atomic fraction of H is necessary to cause IG failure in Monel K-500 as S.

If the values α and φ are assumed to be the same for each material lot (as justified by the similarities in grain boundary character demonstrated in Figure 4.6) then they can be used to investigate how the degree of impurity segregation influences K_{th} . Using the appropriate σ_{YS} value for Table 2.2 and potential-specific C_{H-Diff} values as described in Section 4.2.1, K_{TH} was estimated for TR 1, TR 3, and Allvac as a function of applied potential in Figure 4.9. For the TR 1 material, K_{TH} values of 15 MPa√m at -850mV_{SCE} and 9 MPa√m at -950mV_{SCE} were predicted, which reasonably agrees with the measured K_{TH} of 16 MPa√m at -850mV_{SCE} and 13 MPa√m at -950mV_{SCE}. For the TR 3 material, K_{TH} values of 32 MPa√m at -850mV_{SCE} and 18 MPa√m at -950mV_{SCE} were predicted, which reasonably agrees with the measured K_{TH} of 26 MPa√m at -850mV_{SCE} and 19 MPa√m at -950mV_{SCE}. The good correlation between the predicted and measured K_{TH} values for the TR 1, TR 2, and TR 3 data validates the modeling and highlights the important roles yields strength and sulfur segregation play in governing lot-to-lot HEAC behavior.

For the Allvac material, K_{TH} values of 38 MPa√m at -850mV_{SCE} and 21 MPa√m at -950mV_{SCE} were predicted, which reasonably aligns with the measured K_{TH} of 29 MPa√m for the Allvac material at -950mV_{SCE}. It also predicts a K_{TH} of 38 MPa√m higher than the threshold for the microvoid creep-like cracking observed to start at a K of 31 MPa√m. This explains why the

ductile cracking occurred during testing in the 31 to 38 MPa \sqrt{m} K regime. However, it does not explain why no HEAC occurred for the test entirety up to a K of 60 MPa \sqrt{m} .

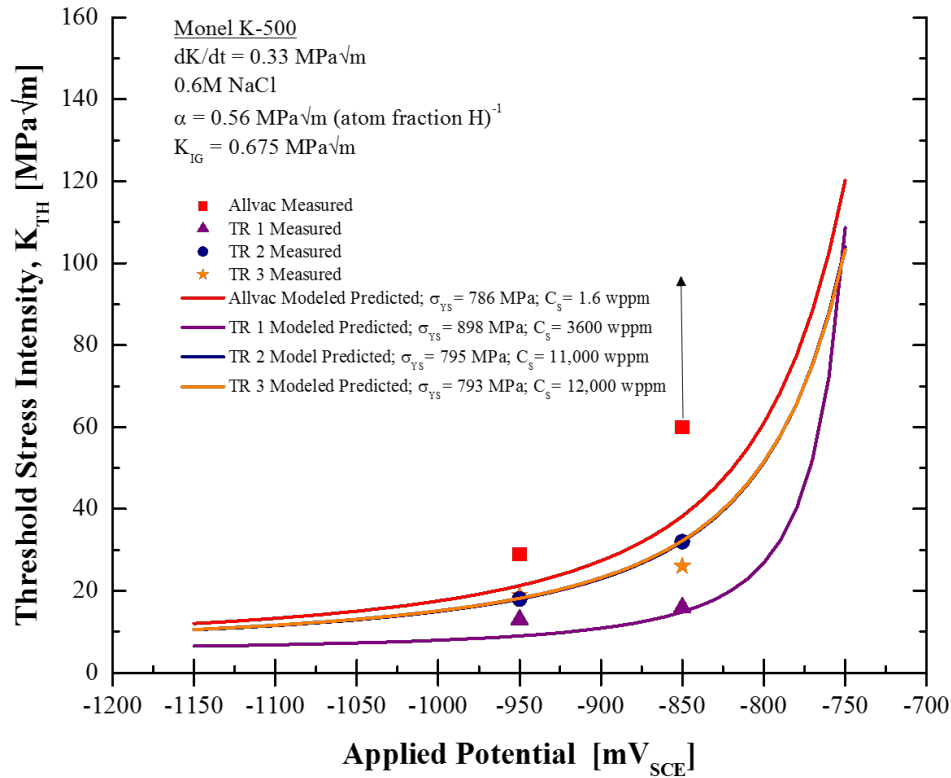


Figure 4.9: Measured K_{TH} and model predicted (Equation 22) K_{TH} for HEAC versus applied potential for four aged Monel K-500 lots accounting for yield strength and possible sulfur segregation differences. The upward arrow indicates HEAC crack growth did not occur during testing.

5 Conclusions

The cracking behavior of four material lots of Monel K-500 (Allvac, TR 1, TR 2, and TR 3) was characterized in order to understand the extent of lot-to-lot variation in the alloy microstructure and its effects on HEAC behavior. Fracture mechanics testing was completed in inert environment (N_2 gas), ASTM artificial ocean water at -1000mV_{SCE} , 0.6M NaCl at -950mV , and 0.6M NaCl at -850mV_{SCE} .

Inert environment testing was completed to establish the resolution limit of the dcPD fracture mechanics test setup and investigate possible lot-to-lot variation in innate toughness. All materials tested demonstrated the same innate material cracking behavior, assuring that differences in HEAC kinetics observed in charging environments are related to the material's reaction to hydrogen rather than being due to differences in inherent toughness of the material.

Two tests were also completed on the Allvac material at $-1000\text{mV}_{\text{SCE}}$, one in 0.6M NaCl and the other in ASTM artificial ocean water to investigate the effects of the electrolyte solution on HEAC kinetics. During testing in the ASTM artificial ocean water, calcareous deposits were observed to form on the bold surface of the SEN(T) specimen. The deposits had the effect of lowering da/dt for a K below $50\text{MPa}\sqrt{\text{m}}$, but did not alter da/dt_{II} as compared to testing in 0.6M NaCl, where no calcareous deposits formed. In addition, testing in ASTM artificial ocean water resulted in a higher K_{TH} . These observations demonstrate beneficial effects of calcareous deposit formation in that it reduced HEAC cracking during the test. However, the stochastic nature of the deposit nucleation precludes the consideration of calcareous deposit effects on component lifetime estimates. In addition, the main goal of this project is to investigate material differences in HEAC behavior. It was not desirable to add in the extra complexity of calcareous deposits and their effect on HEAC behavior during additional testing. Testing in 0.6M NaCl yields conservative da/dt vs K data and allows for chloride to be in the solution, which plays an important role in the HEAC damage mechanism. Thus, 0.6M NaCl was chosen to be the electrolyte solution in other testing.

The HEAC kinetics for all materials were characterized at $-950\text{mV}_{\text{SCE}}$. No significant difference was observed in K_{TH} or da/dt_{II} between TR 1, TR 2, and TR 3. The Allvac material showed the same da/dt_{II} as TR 1-3, but had a higher K_{TH} , supporting the observation that Allvac had an increased resistance to HEAC as compared to the three tie rods. The similarities in da/dt_{II} is explained by the very high concentration of hydrogen introduced into the FPZ, $C_{\text{H}\sigma}$, at this aggressively cathodic potential.

HEAC characterization in the near-immunity potential regime ($-850\text{mV}_{\text{SCE}}$) revealed slight variation in K_{TH} and da/dt_{II} between TR 1, TR 2, and TR 3. These small differences in HEAC behavior correlated with the grain size of the material, with K_{TH} increasing and da/dt_{II} increasing with increasing grain size, though this trend is weak given the small differences in

measured K_{TH} between TR 1, TR 2, and TR 3. The Allvac material, on the other hand, did not suffer HEAC at this potential, contrary to previous work on the Allvac material [8]. Rather the crack growth during observed during testing was identical to the time-dependent microvoid cracking observed during testing in inert environment. The reasons behind the different behavior in the Allvac material observed in this project and in previous work remain unknown and are likely related to differences in lab setup and/or the masking of the bold surfaces on the SEN(T) specimens. Regardless, several data points to Allvac having improved HEAC resistance compared to TR 1, TR 2, and TR 3, including SSRT testing completed in previous work and with recent hydrogen study, where C_{H-Diff} was found to be lower in Allvac than in TR 2. The extensive material characterization completed in this work was focused on identifying the microstructural feature(s) present in Allvac, but not in TR 1, TR 2, or TR 3, that can explain the observed difference in HEAC susceptibility at $-850mV_{SCE}$.

An attempt was made to explain the observed differences in HEAC behavior at $-850mV_{SCE}$ through a thorough examination of metallurgical and/or microstructural variation present between the material lots. The effects of lot-to-lot variation in yield strength, grain size, crack deflection, grain boundary character, grain boundary connectivity, and sulfur segregation were investigated. This work suggests that the HEAC differences are most likely attributed to (a) the decreased yield strength of Allvac as compared to TR 1, TR 2, and TR 3 and/or (b) perhaps a smaller concentration of sulfur at the grain boundary, leading to less grain boundary embrittlement occurring in the Allvac material than in the three tie rods. Explanation (a) is supported by accurate prediction of HEAC behavior through K_{TH} modeling. Explanation (b) is supported by Auger depth analysis showing sulfur segregation in TR 2 not present in Allvac, though the Auger work may be compromised by surface contamination prior to Auger analysis, Allvac having the lowest bulk concentration of S of all the material lots in Table 2.1, and by accurate prediction of HEAC behavior through novel K_{TH} modeling accounting for simultaneous S and H embrittlement.

Work in this project on four lots of aged Monel K-500 and previous work on the Allvac material lot demonstrate HEAC susceptibility is strongly dependent on environmental conditions, with da/dt_{II} increasing and K_{TH} decreasing with increasingly cathodic applied potentials [8]. This is attributed to increasing C_{H-Diff} as the applied potential becomes more

cathodic, supplying more H to the FPZ and leading to increased H embrittlement along the grain boundary. Previous work on the Allvac material lot demonstrated the existence of a threshold potential above which HEAC is limited by a low C_{H-Diff} [8]. Figure 4.9 shows HEAC susceptibility sharply decreases, measured as decreasing K_{TH} , as the applied potential approaches the threshold potential for HEAC, which was identified to be around $-770mV_{SCE}$ for the Allvac material in previous work [8]. A small shift in the threshold potential can be seen between the material lots in Figure 4.2 and Figure 4.9. This suggests the threshold potential for HEAC is sensitive to metallurgical differences. Metallurgical effects on the threshold potential become important in near-threshold potential environmental conditions since the HEAC behavior changes drastically with small changes in potential in this regime.

In the field, fluctuations in the applied potential may be leading to the observed Monel K-500 service failures. Components that failed may have been exposed to more cathodic potentials than other components, leading to increased H embrittlement and HEAC. This effect could be amplified by differences in the metallurgically sensitive threshold potential that exists between different Monel K-500 lots. The combination of more cathodic potential and component metallurgy correlating to a less cathodic threshold potential would cause large difference in HEAC behavior, especially in the potential regime near the threshold potential. This may explain why some components fail during service while others do not.

All materials experienced unexpected and stable crack growth well below the reported K_{IC} of 198-340 $MPa\sqrt{m}$ during the inert environment testing[8]. This cracking was tentatively identified as microvoid time-dependent cracking and was observed in all materials above a K of 35 $MPa\sqrt{m}$. This cracking was also observed in the Allvac material when tested in 0.6M NaCl at the near-immunity potential of $-850mV_{SCE}$. However, the exact mechanism behind the observed crack growth is not well understood since it occurs below K_{IC} . It is unclear whether this kind of cracking has led to component failures in the field, as the failure analysis reports studied in this project identified HEAC as the failure mechanism rather than ductile failure [1-7]. However, this cracking must be understood as it may lead to significant component damage even in the most inert environmental conditions.

6 References

- [1] R. E. Butler, "Hydrogen Embrittlement of High-strength Alloys in Marine Environments," in *Alloys*, London, U.K.: Metals Society, 1988, pp. 79-84.
- [2] C. A. Clark, S. Driscoll, and P. Guha., "Development of a New Fastener Alloy Resistant to Hydrogen Embrittlement " *British Corrosion Journal*, vol. 27, pp. 157-160, 1992.
- [3] G. A. Scott, "Studbolting Experience in the Underwater Environment of the North Sea," presented at the 17th Offshore Technology Conference, Paper No. OTC 5050, Houston, TX, 1985.
- [4] R. N. Tuttle and J. W. Kochera, *Control of Hydrogen Embrittlement in Deep Gas Wells*. United States: Metallurgical Society AIME, 1976.
- [5] L. Wolfe, C. Burnetter, and M. Joosten, "Hydrogen Embrittlement of Cathodically Protected Subsea Bolting Alloys," presented at the Corrosion 93, Paper No. 288, Houston, TX, 1993.
- [6] J. R. Scully and M. G. Vassilaros, "The Hydrogen Embrittlement Susceptibility of Monel Alloy K-500," presented at the Electrochemical Society Fall 1983 Meeting, Washington, D.C. , 1983.
- [7] R. D. Bayles, T. Lemieux, F. Martin, D. Lysogorski, T. Newbauer, W. Hyland, *et al.*, "Monel K-500 Hydrogen Embrittlement," presented at the Naval Surface Treatment Center MR2010 Proceedings Presentation, 2010.
(<http://nstcenter.com/docs/PDFs/MR2010/Thurs-1-Presentations/10-Bayles.PDF>).
- [8] R. Gangloff, H. Ha, J. Burns, and J. Scully, "Measurement and Modeling of Hydrogen Environment-Assisted Cracking in Monel K-500," *Metallurgical and Materials Transactions A*, vol. 45, pp. 3814-3834, 2014.
- [9] H. R. Copson and C. F. Cheng, "Stress Corrosion Cracking Of Monel in Hydrofluoric Acid," *Corrosion*, vol. 12, pp. 71-77, 1956.
- [10] R. P. Gangloff, "Hydrogen Assisted Cracking of High Strength Alloys," in *Comprehensive Structural Integrity*. vol. 6, I. Milne, R. O. Ritchie, and B. Karahaloo, Eds., New York, NY: Elsevier Science, 2003, pp. 31-101.
- [11] J. A. Lillard, "Environment Assisted Cracking of a Nickel-Based Superalloy in Hydrogen-Producing Solutions," PhD Dissertation, University of Virginia, Charlottesville, VA, 1998.
- [12] J. Ai, H. M. Ha, R. P. Gangloff, and J. R. Scully, "Hydrogen Diffusion and Trapping in a Precipitation-Hardened Nickel–Copper–Aluminum Alloy Monel K-500 (UNS N05500)," *Acta Materialia*, vol. 61, pp. 3186-3199, 2013.
- [13] *Nickel-Copper-Aluminum Alloy, Wrought (UNS N05500)*. QQ-N-286G: Department of the Navy, 2000.
- [14] R. P. Gangloff, D. C. Slavik, R. S. Piascik, and R. H. V. Stone, "Direct Current Electrical Potential Measurement of the Growth of Small Cracks," in *Small-Crack Test Methods, ASTM STP 1149*, M. Larsen and J. E. Allison, Eds., Philadelphia: ASTM International, 1992, pp. 116-168.
- [15] D. H. Lassila and H. K. Birnbaum, "The Effect of Diffusive Segregation on the Fracture of Hydrogen Charged Nickel," *Acta Metallurgica*, vol. 36, pp. 2821-2825, 1988.
- [16] S. Bechtel, M. Kumar, B. P. Somerday, M. E. Launey, and R. O. Ritchie, "Grain-Boundary Engineering Markedly Reduces Susceptibility to Intergranular Hydrogen Embrittlement in Metallic Materials," *Acta Materialia*, vol. 57, pp. 4148-4157, 2009.

- [17] M. W. Joosten and L. H. Wolfe, "Failures of Nickel-Copper Bolts in Subsea Applications," Offshore Technology Conference Paper No 5553-MS, 1987.
- [18] M. G. Vassilaros, R. L. Juers, M. E. Natishan, and A. K. Vasudevan, "Environmental Slow Strain Rate J-Integral Testing of Ni-Cu Alloy K-500 " in *Slow Strain Rate Testing for the Evaluation of Environmentally Induced Cracking: ASTM STP 1210*, R. D. Kane, Ed., West Conshohocken, PA: ASTM International, 1993, pp. 123-133.
- [19] B. A. Kehler and J. R. Scully, "Predicting the Effect of Applied Potential on Crack Tip Hydrogen Concentration in Low-Alloy Martensitic Steels," *Corrosion*, vol. 64, pp. 465-477, 2008.
- [20] Y. D. Park, D. L. Olson, A. Landau, and M. Pinkas, "Assessment of Hydrogen-Induced Precipitation in a Nickel-Copper Alloy Using Thermoelectric Power," *Corrosion*, vol. 62, pp. 395-402, 2006.
- [21] S. Lynch, "Hydrogen Embrittlement Phenomena and Mechanisms," *Corrosion Reviews*, vol. 30, pp. 105-123, 2012.
- [22] T. Boniszewski and G. C. Smith, "The Influence of Hydrogen on the Plastic Deformation Ductility, and Fracture of Nickel in Tension," *Acta Metallurgica*, vol. 11, pp. 165-178, 1963.
- [23] M. L. Wayman and G. C. Smith, "The Effects of Hydrogen on the Deformation and Fracture of Nickel-Iron Alloys," *Acta Metallurgica*, vol. 19, pp. 227-231, 1971.
- [24] M. L. Martin, B. P. Somerday, R. O. Ritchie, P. Sofronis, and I. M. Robertson, "Hydrogen-Induced Intergranular Failure in Nickel Revisited," *Acta Materialia*, vol. 60, pp. 2739-2745, 2012.
- [25] Z. Guo, M. Zhao, C. Li, S. Chen, and L. Rong, "Mechanism of Hydrogen Embrittlement in a Gamma-Prime Phase Strengthened Fe-Ni Based Austenitic Alloy," *Materials Science and Engineering: A*, vol. 555, pp. 77-84, 2012.
- [26] Y. Katz, N. Tymiak, and W. Gerberich, "Nanomechanical Probes as New Approaches to Hydrogen/Deformation Interaction Studies," *Engineering Fracture Mechanics*, vol. 68, pp. 619-646, 2001.
- [27] H. Huang and W. W. Gerberich, "Quasi-Equilibrium Modeling of the Toughness Transition During Semibrittle Cleavage," *Acta Metallurgica et Materialia*, vol. 42, pp. 639-647, 1994.
- [28] C. D. S. Tuck, X. Zeng, and D. E. J. Talbot, "Hydrogen Embrittlement Resistance of Ultrahigh Strength Cupronickel Alloy: Effects of Exposure to Gaseous Hydrogen Environment on Fatigue Resistance " *British Corrosion Journal*, vol. 29, pp. 70-74, 1995.
- [29] U. Komaragiri, S. R. Agnew, R. P. Gangloff, and M. R. Begley, "The Role of Macroscopic Hardening and Individual Length-Scales on Crack Tip Stress Elevation from Phenomenological Strain Gradient Plasticity," *Journal of the Mechanics and Physics of Solids*, vol. 56, pp. 3527-3540, 2008.
- [30] R. P. Gangloff, "Accelerated Measurement and Mechanism-Based Simulation of Hydrogen Cracking," presented at the Hydrogen Embrittlement: Multi-Scale Modelling and Measurement, Teddington, Middlesex, 2014.
- [31] G. K. Dey and P. Mukhopadhyay, "Precipitation in the Ni-Cu-Base Alloy Monel K-500," *Materials Science and Engineering*, vol. 84, pp. 177-189, 1986.
- [32] G. K. Dey, R. Tewari, P. Rao, S. L. Wadekar, and P. Mukhopadhyay, "Precipitation Hardening in Nickel-Copper Base Alloy Monel K 500," *Metallurgical Transactions A*, vol. 24, pp. 2709-2719, 1993.

- [33] J. R. Davis, "Nickel, Cobalt, and Their Alloys: ASM Specialty Handbook," ed: ASM International, 2000.
- [34] J. Kameda, "Equilibrium and Growth Characteristics of Hydrogen-Induced Intergranular Cracking in Phosphorus-Doped and High Purity Steels," *Acta Metallurgica*, vol. 34, pp. 1721-1735, 1986.
- [35] N. R. Moody, R. E. Stoltz, and M. W. Perra, "The Relationship of Grain Size to Critical Distance and Hydrogen-Induced Crack Growth Thresholds," *Scripta Metallurgica*, vol. 20, pp. 119-123, 1986.
- [36] A. Oudriss, J. Bouhattate, C. Savall, J. Creus, X. Feaugas, F. A. Martin, *et al.*, "On the Implication of Hydrogen on Inter-granular Fracture," *Procedia Materials Science*, vol. 3, pp. 2030-2034, 2014.
- [37] J. R. Scully, "Environment-Assisted Intergranular Cracking: Factors that Promote Crack Path Connectivity," in *Environmentally Assisted Cracking: Predictive Methods for Risk Assessment and Evaluation of Materials, Equipment, and Structures*, ASTM STP 1401, R. D. Kane, Ed., West Conshohocken, PA: ASTM International, 2000, pp. 40-69.
- [38] W. C. Johnson, J. E. Doherty, B. H. Kear, and A. F. Giamei, "Confirmation of Sulfur Embrittlement in Nickel Alloys," *Scripta Metallurgica*, vol. 8, pp. 971-974, 1974.
- [39] D. H. Lassila and H. K. Birnbaum, "Intergranular Fracture of Nickel: the Effect of Hydrogen-Sulfur Co-segregation," *Acta Metallurgica*, vol. 35, pp. 1815-1822, 1987.
- [40] C. J. McMahon, C. L. Briant, and S. K. Banerji, "The Effect of Hydrogen and Impurities on Brittle Fracture in Steel," in *Proc. Fourth International Conference on Fracture*. vol. 1, D. M. R. Taplin, Ed., Waterloo: University of Waterloo Press, 1977, p. 363.
- [41] J. F. Knott, "Fracture Toughness and Hydrogen-Assisted Crack Growth in Engineering Alloys," in *Hydrogen Effects in Materials*: John Wiley & Sons, Inc., 2013, pp. 385-408.
- [42] H. Fukushima and H. K. Birnbaum, "Surface and Grain Boundary Segregation of Deuterium in Nickel," *Acta Metallurgica*, vol. 32, pp. 851-859, 1984.
- [43] R. M. Latanision and H. Opperhauser, "The intergranular embrittlement of nickel by hydrogen: The effect of grain boundary segregation," *Metallurgical Transactions*, vol. 5, pp. 483-492, 1974/02/01 1974.
- [44] J. Chakravarty, T. Sinha, and M. Asundi, "Effects of Hydrogen and Impurities on Fracture Behaviour of a Low Strength Cr-Mo Steel," *Advances in Fracture Research(Fracture 84)*. vol. 4, pp. 2419-2426, 1984.
- [45] A. Brokman and R. W. Balluffi, "Coincidence Lattice Model for the Structure and Energy of Grain Boundaries," *Acta Metallurgica*, vol. 29, pp. 1703-1719, 1981.
- [46] S. Ranganathan, "On the Geometry of Coincidence-Site Lattices," *Acta Crystallographica*, vol. 21, pp. 197-199, 1966.
- [47] H. Mykura, "A Checklist of Cubic Coincidence Site Lattice Relations," in *Grain-Boundary Structure and Kinetics*, Metals Park, Ohio: ASTM International,, 1980, pp. 445-456.
- [48] W. T. Read and W. Shockley, "Dislocation Models of Crystal Grain Boundaries," *Physical Review*, vol. 78, pp. 275-289, 1950.
- [49] S. Jothi, T. N. Croft, and S. G. R. Brown, "Influence of Grain Boundary Misorientation on Hydrogen Embrittlement in Bi-Crystal Nickel," *International Journal of Hydrogen Energy*, 2014.

- [50] J. Bruley, V. J. Keast, and D. B. Williams, "An EELS Study of Segregation-Induced Grain-Boundary Embrittlement of Copper," *Acta Materialia*, vol. 47, pp. 4009-4017, 1999.
- [51] V. J. Keast, J. Bruley, P. Rez, J. M. Maclaren, and D. B. Williams, "Chemistry and Bonding Changes Associated with the Segregation of Bi to Grain Boundaries in Cu," *Acta Materialia*, vol. 46, pp. 481-490, 1998.
- [52] V. J. Keast and D. B. Williams, "Quantitative Compositional Mapping of Bi Segregation to Grain Boundaries in Cu," *Acta Materialia*, vol. 47, pp. 3999-4008, 1999.
- [53] S. Kobayashi, T. Maruyama, S. Tsurekawa, and T. Watanabe, "Grain Boundary Engineering Based on Fractal Analysis for Control of Segregation-Induced Intergranular Brittle Fracture in Polycrystalline Nickel," *Acta Materialia*, vol. 60, pp. 6200-6212, 2012.
- [54] A. Schwartz, M. Kumar, and D. Lassila, "Analysis of Intergranular Impurity Concentration and the Effects on the Ductility of Copper-Shaped Charge Jets," *Metallurgical and Materials Transactions A*, vol. 35, pp. 2567-2573, 2004.
- [55] A. Oudriss, J. Creus, J. Bouhattate, E. Conforto, C. Berziou, C. Savall, *et al.*, "Grain Size and Grain-Boundary Effects on Diffusion and Trapping of Hydrogen in Pure Nickel," *Acta Materialia*, vol. 60, pp. 6814-6828, 2012.
- [56] T. Watanabe, "Grain Boundary Engineering: Historical Perspective and Future Prospects," *Journal of Materials Science*, vol. 46, pp. 4095-4115, 2011.
- [57] B. P. Somerday and N. R. Moody, "Micromechanical Modeling of Hydrogen-Induced Fracture Modes in IN903," in *Advances in Fracture Research, Proceedings of ICF10*, Oxford, UK, 2001.
- [58] G. Gray, III, S. Chen, and K. Vecchio, "Influence of Grain Size on the Constitutive Response and Substructure Evolution of Monel 400," *Metallurgical and Materials Transactions A*, vol. 30, pp. 1235-1247, 1999.
- [59] E. O. Hall, "The Deformation and Ageing of Mild Steel: III Discussion of Results," *Proceedings of the Physical Society. Section B*, vol. 64, p. 747, 1951.
- [60] N. J. Petch, "The Cleavage Strength of Polycrystals," *The Journal of the Iron and Steel Institute*, vol. 173, pp. 25-28, 1953.
- [61] N. Hansen, "Hall-Petch Relation and Boundary Strengthening," *Scripta Materialia*, vol. 51, pp. 801-806, 2004.
- [62] K. D. Ralston and N. Birbilis, "Effect of Grain Size on Corrosion: A Review," *Corrosion*, vol. 66, pp. 075005 1-13, 2010.
- [63] D. Cheng, V. L. Tellkamp, C. J. Lavernia, and E. J. Lavernia, "Corrosion Properties of Nanocrystalline Co-Cr Coatings," *Annals of Biomedical Engineering*, vol. 29, pp. 803-809, 2001.
- [64] R. O. Ritchie, "Mechanisms of Fatigue Crack Propagation in Metals, Ceramics and Composites: Role of Crack Tip Shielding," *Materials Science and Engineering: A*, vol. 103, pp. 15-28, 1988.
- [65] R. O. Ritchie and S. Suresh, "Some Considerations on Fatigue Crack Closure at Near-Threshold Stress Intensities Due to Fracture Surface Morphology," *Metallurgical Transactions A*, vol. 13, pp. 937-940, 1982.
- [66] S. Suresh, "Crack Deflection: Implications for the Growth of Long and Short Fatigue Cracks," *Metallurgical Transactions A*, vol. 14, pp. 2375-2385, 1983.

- [67] J. E. King, "Fatigue Crack Propagation in Nickel-Base Superalloys – Effects of Microstructure, Load Ratio, and Temperature," *Materials Science and Technology*, vol. 3, pp. 750-764, 1987.
- [68] J. R. Scully and B. Rincón-Troconis, *Personal Communication*. University of Virginia, 2014-2015.
- [69] T. L. Anderson, *Fracture Mechanics: Fundamentals and Applications*. Boca Raton, FL: CRC Press: Taylor and Francis Group, 2005.
- [70] H. Tada, P.C. Paris, and G.R. Irwin, *The Stress Analysis of Cracks Handbook*. St. Louis, MO: Paris Productions Incorporated, 1985.
- [71] H. H. Johnson, "Calibrating the Electric Potential Method for Studying Slow Crack Growth," in *Materials Research and Standards*. vol. 5: ASTM International, 1965, pp. 442-444.
- [72] J. K. Donald and J. Ruschau, "Direct Current Potential Difference Fatigue Crack Measurement Techniques," in *Fatigue Crack Measurement: Techniques and Applications*, K. J. Marsh, R. A. Smith, and R. O. Ritchie, Eds., Warley, UK: Engineering Materials Advisory Service Ltd., 1991, pp. 11-37.
- [73] S. A. English and N. K. Arakere, "Effects of the Strain-Hardening Exponent on Two-Parameter Characterizations of Surface-Cracks under Large-Scale Yielding," *International Journal of Plasticity*, vol. 27, pp. 920-939, 2011.
- [74] S. Cravero and C. Ruggieri, "Estimation Procedure of J-Resistance Curves for SE(T) Fracture Specimens using Unloading Compliance," *Engineering Fracture Mechanics*, vol. 74, pp. 2735-2757, 2007.
- [75] V. Kumar, M. D. German, and C. F. Shih, *An Engineering Approach for Elastic-Plastic Fracture Analysis, EPRI Final Report NP-1931*. Palo Alto, CA: Electric Power Research Institute 1981.
- [76] "Capabilities of Quanta 200 SEM," in *FEI Quanta 200 SEM*, The Ohio State University: Center for Electron Microscopy and Analysis (CEMAS), 2014 (<https://cemas.osu.edu/instrumentation/fei-quanta-200-sem>).
- [77] O. Thompson, *Quanta x50 Training Handbook*. Hillsboro, OR: FEI, 2012.
- [78] M. Dufek and M. Hayles, *The Quanta FEG 200, 400, 600 User's Operation Manual*. Hillsboro, Ohio: FEI Company, 2003.
- [79] F. J. Humphreys, "Review Grain and Subgrain Characterisation by Electron Backscatter Diffraction," *Journal of Materials Science*, vol. 36, pp. 3833-3854, 2001.
- [80] A. J. Wilkinson, G. Meaden, and D. J. Dingley, "High-Resolution Elastic Strain Measurement from Electron Backscatter Diffraction Patterns: New Levels of Sensitivity," *Ultramicroscopy*, vol. 106, pp. 307-313, 2006.
- [81] A. Roy, E. Perfect, W. M. Dunne, and L. D. McKay, "Fractal Characterization of Fracture Networks: An Improved Box-Counting Technique," *Journal of Geophysical Research: Solid Earth*, vol. 112, pp. B12201 1-9, 2007.
- [82] T. W. Crooker and B. N. Leis, *Corrosion Fatigue Mechanics, Metallurgy, Electrochemistry and Engineering: ASTM STP801*: ASTM International, 1983.
- [83] F. Zucchi, V. Grassi, C. Monticelli, and G. Trabanelli, "Hydrogen Embrittlement of Duplex Stainless Steel under Cathodic Protection in Acidic Artificial Sea Water in the Presence of Sulphide Ions," *Corrosion Science*, vol. 48, pp. 522-530, 2006.
- [84] S. W. Dean and H. R. Copson, "Stress Corrosion Behavior Of Maraging Nickel Steels In Natural Environments," *Corrosion*, vol. 21, pp. 95-103, 1965.

- [85] K. Nibur, B. Somerday, C. Marchi, J. Foulk, III, M. Dadfarnia, and P. Sofronis, "The Relationship Between Crack-Tip Strain and Subcritical Cracking Thresholds for Steels in High-Pressure Hydrogen Gas," *Metallurgical and Materials Transactions A*, vol. 44, pp. 248-269, 2013.
- [86] A. Bahadori, *Corrosion and Materials Selection: A Guide for the Chemical and Petroleum Industries*: Wiley, 2014.
- [87] W. H. Hartt, C. H. Culberson, and S. W. Smith, "Calcareous Deposits on Metal Surfaces in Seawater—A Critical Review," *Corrosion*, vol. 40, pp. 609-618, 1984.
- [88] S. S. Rajpathak and W. H. Hartt, "Formation of Calcareous Deposits within Simulated Fatigue Cracks in Seawater," *Corrosion*, vol. 43, pp. 339-347, 1987.
- [89] R. C. Dorward and K. R. Hasse, "Flaw Growth in High Strength Al-Zn-Mg-Cu Alloys Exposed to Stress Corrosion Environments," *Corrosion*, vol. 34, pp. 386-395, 1978.
- [90] R. P. Gangloff, *Personal Communication*. University of Virginia, 2014-2015.
- [91] J. P. Hirth and J. Lothe, *Theory of Dislocations*: Krieger Publishing Company, 1982.
- [92] W. F. Hosford, *Mechanical Behavior of Materials*: Cambridge University Press, 2010.
- [93] J. Tien, A. Thompson, I. M. Bernstein, and R. Richards, "Hydrogen Transport by Dislocations," *Metallurgical Transactions A*, vol. 7, pp. 821-829, 1976.
- [94] E. E. Underwood, *Quantitative stereology*: Addison-Wesley Pub. Co., 1970.
- [95] R. A. Mulford, "Grain Boundary Segregation in Ni and Binary Ni Alloys Doped with Sulfur," *Metallurgical Transactions A*, vol. 14, pp. 865-870, 1983.
- [96] R. G. Thompson, J. R. Dobbs, and D. E. Mayo, "The Effect of Heat Treatment on Microfissuring in Alloy 718 " *Welding Journal*, vol. 65, pp. 299s-304s, 1986.
- [97] C. L. Briant, "Grain Boundary Segregation of Sulfur in Iron," *Acta Metallurgica*, vol. 33, pp. 1241-1246, 1985.
- [98] C. L. Briant, H. C. Feng, and C. J. McMahon, "Embrittlement of a 5 Pct Nickel High Strength Steel by Impurities and Their Effects on Hydrogen-Induced Cracking," *Metallurgical Transactions A*, vol. 9, pp. 625-633, 1978.
- [99] M. E. Glicksman, *Diffusion in Solids: Field Theory, Solid-State Principles, and Applications*: Wiley, 1999.
- [100] J. Crank, *The Mathematics of Diffusion*: Clarendon Press, 1979.

A: Testing Method Considerations

A.1 Observed Crack Length Dependent HEAC Behavior at $-850mV_{SCE}$

During the initial phases of the research, multiple K-rise tests were run on a single sample to increase the amount of HEAC data that could be generated on a limited number of specimens; these tests were complicated by crack length dependent HEAC growth rate behavior. The results of three K-rise ($0.33\text{MPa}\sqrt{\text{m/hr}}$) tests on a single specimen of Allvac at $-850mV_{SCE}$ are shown in Figure A.1 and illustrate typical behavior; the starting crack sizes were 1.05, 2.86, and 7.18 mm for the first, second and third test, respectively. Between each of the tests the specimen was fatigued under a series of decreasing ΔK protocols. The first K-shed is from a K_{max} of $60\text{MPa}\sqrt{\text{m}}$ to $30\text{MPa}\sqrt{\text{m}}$ ($R=0.5$) over 0.500 mm of crack growth ($C=-1.4$). This is followed by a K-shed from $30\text{MPa}\sqrt{\text{m}}$ to $20\text{MPa}\sqrt{\text{m}}$ ($R=0.1$) over 0.517 mm of crack growth ($C=-0.8$). The final K-shed is from $20\text{MPa}\sqrt{\text{m}}$ to $13.5\text{MPa}\sqrt{\text{m}}$ ($R=0.1$) over 0.983 mm of crack growth ($C=-0.4$). This protocol was employed to limit load history effects from loading in previous tests and resulted in a transgranular, slip based cracking fracture surface morphology in the fatigued portion of the fracture surface.

The da/dt values in Test 1 in Figure A.1 show crack growth rates similar to what was measured in inert environment testing (a direct comparison of the growth rates is shown in Figure 3.14 and is discussed in detail in Section 3.1.2.3). The cracking was later confirmed to be ductile crack extension (Figure A.2 and Figure A.3) starting at stress intensity of $31\text{MPa}\sqrt{\text{m}}$ and a having crack growth rate of $2.3 \times 10^{-6}\text{mm/s}$ at a K of $60\text{MPa}\sqrt{\text{m}}$. The second and third test show HEAC crack growth (Figure A.2 and Figure A.3) with a lower threshold of $10\text{MPa}\sqrt{\text{m}}$ and $15\text{MPa}\sqrt{\text{m}}$ respectively, but a lower stage II growth rate. Also of note is the slight decrease in da/dt throughout the course of the test. Data in Figure A.1 clearly demonstrates that similitude is not realized for growth rates generated for the different crack sizes and loading histories in Test 1, 2, and 3.

Fracture surface analysis shows that the extent of HEAC crack growth associated with Test 2 and Test 3 increases for testing at longer crack depths but identical testing conditions. This is apparent in Figure A.2, where the crack growth (indicated by the area between the blue, red, and green lines) increases with each subsequent test. Moreover, there is a change in crack

growth mechanism between Test 1 and the subsequent tests. Figure A.3 shows fractography revealing crack growth during Test 1 was due to ductile-like failure similar to what was observed in fracture mechanics testing of the Allvac material in inert, non-charging, environments where no hydrogen embrittlement is possible. Crack growth in Test 2 and Test 3, however, is observed to have occurred due to HEAC, evidenced by the pure intergranular fracture surfaces created during these tests, enclosed in red for Test 3 in Figure A.3 (c) and (d). This suggests that either Test 1 is an outlier or there was a change in crack tip electrochemistry associated with the different crack lengths.

This appendix will discuss several potential mechanisms that may contribute to this crack depth dependent behavior, including an increased influence of crack wake shorting for the lower crack opening displacements (CODs) associated longer crack sizes, a load-history effect due to the prior fracture mechanics test, crack depth dependent crack tip electrochemistry, and/or an influence of specimen plasticity. While each are considered in this appendix, a detailed investigation to conclusively determine the cause of this behavior is outside of the scope of this thesis that focuses on quantifying and understanding any metallurgical differences for different lots of Monel K-500. All HEAC data reported in main body of the thesis was generated for a single crack per specimen. However, this reporting and analysis of the observed crack size dependent behavior is justified to inform the extent to which the reported HEAC growth rates can be used in fracture mechanism prediction models of other cracking geometries and to inform future efforts to standardize this dcPD-based method for characterizing HEAC behavior.

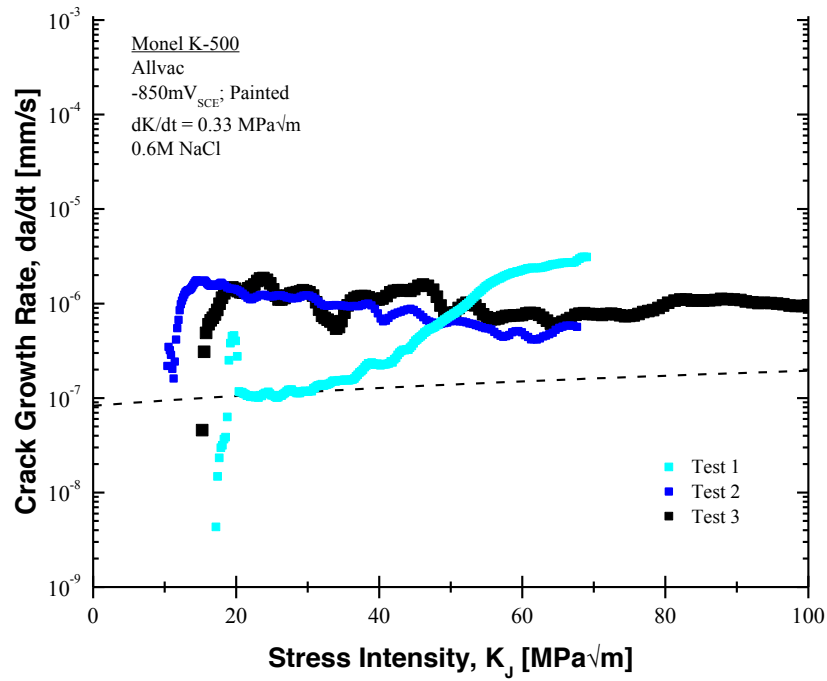


Figure A.1: da/dt vs plastic K for subsequent tests of Allvac at $-850mV_{SCE}$ executed with a slow K -rise ($0.33 MPa\sqrt{m/hr}$). Each test was run on the same sample.

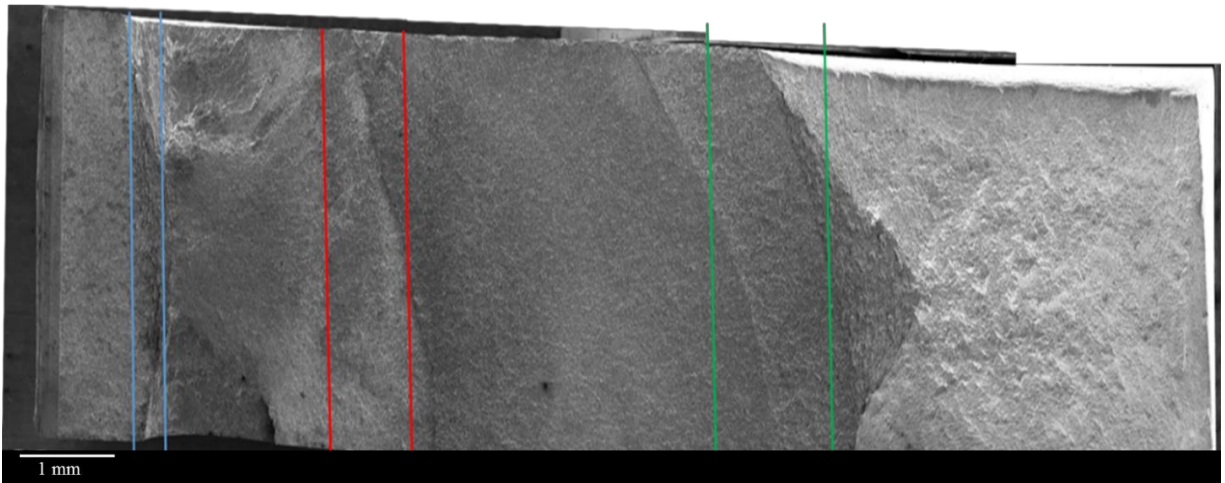


Figure A.2: The fracture surface of multiple fracture mechanics tests run on a single Allvac SEN(T) sample in $0.6M NaCl$ at $-850mV_{SCE}$.

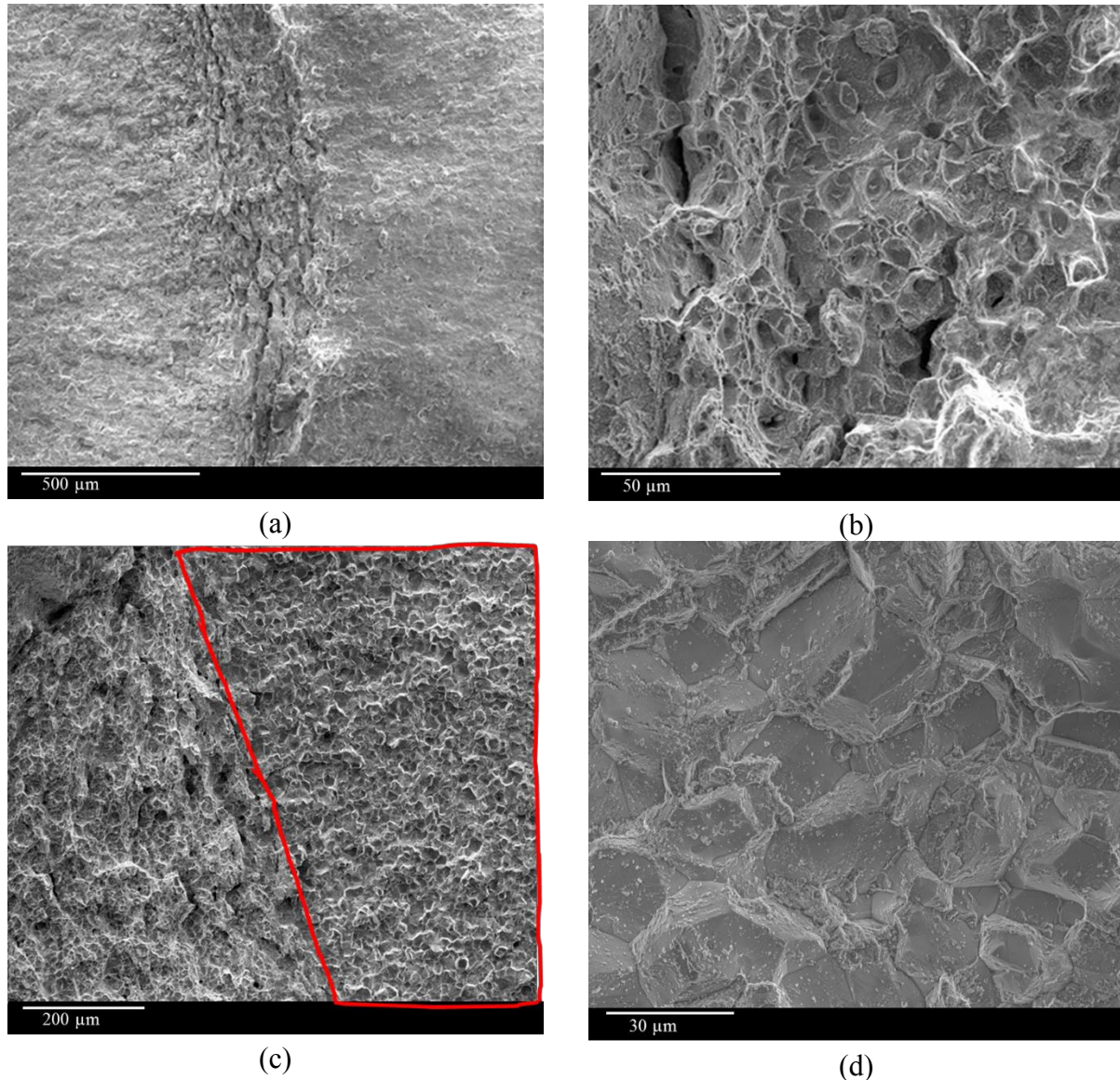


Figure A.3: Fractography showing (a) macro-scale image and (b) ductile failure of Test 1 on Allvac at $-850\text{mV}_{\text{SCE}}$; also shown are (c) macro-scale and (d) high magnification images of intergranular failure of Test 2. The area outlined in red in (c) shows the IG failure that occurred during Test 3

A.1.i Crack Wake Surface Contact

There should exist a maximum COD (call it COD_{Max}) for which crack wake surface contact is possible. This COD_{Max} can be assumed to be equal to twice the maximum height of fracture surface features, which will vary with cracking morphology and grain size. At a constant K , the average COD would be smaller for longer crack sizes due to the lower stresses needed to achieve the same stress intensity. These lower COD values would increase the fraction of crack length for which the COD is below COD_{Max} , suggesting more surface contact

occurs at long crack lengths leading to greater amounts of shorting. This is demonstrated schematically in Figure A.4, which shows the distance over which wake surface contact is possible, D_{SH} , is higher for a long crack than a short crack at a constant K . In order for shorting to be the cause of the long duration of elevated da/dt seen in Test 2 and Test 3 in Figure A.1, significant crack wake contact would need to occur throughout the duration of both tests.

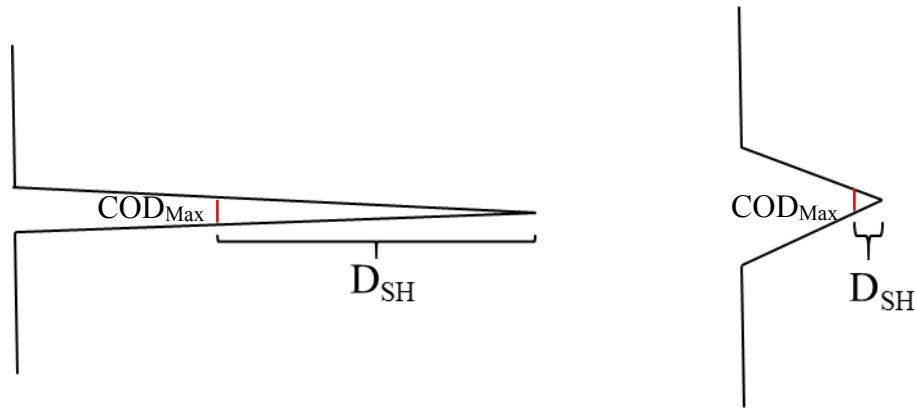


Figure A.4: Schematic showing the difference in D_{SH} between a long crack and a short crack for the same applied K . The location of COD_{Max} , which is assumed to be constant, is shown by the vertical red line in the crack wake.

In order to separate the effects of fracture surface shorting from possible load history effects, additional fracture mechanics tests were carried out on two separate Allvac specimens at $-1000mV_{SCE}$. One sample was tested at short crack lengths (1 mm) and the other was tested at long crack lengths (4 mm). The crack mouth opening displacement can be calculated from the crack depth and loading conditions [69, 70]. From this, the crack geometry can be approximated using the triangular model that assumes no opening at the crack tip and no deflection of the crack wake surfaces in Figure A.5. When the distance between the two fracture surfaces, Y , is less than COD_{Max} , wake surface contact is possible. The area of possible surface contact is described by the distance behind of the crack tip, $d_{contact}$, which is related to $Y/2$ and θ in Figure A.5.

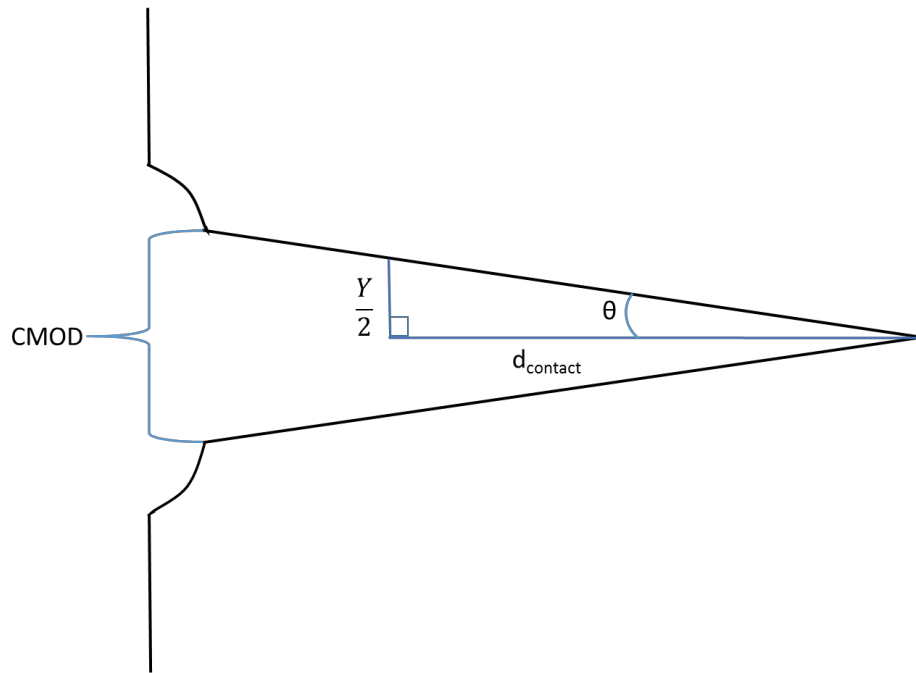
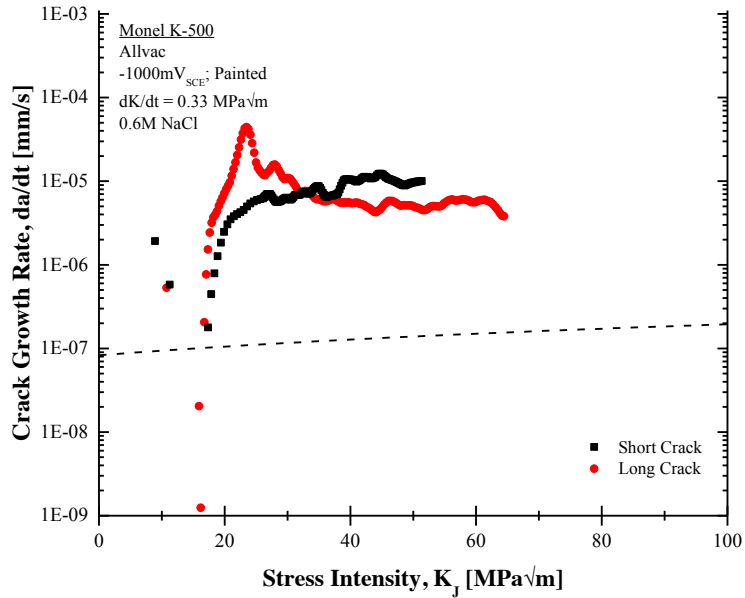


Figure A.5: Triangular model of the crack geometry, where CMOD is the crack mouth opening displacement, Y is the distance between the fracture surfaces and is a function of the distance ahead of the crack tip, d_{contact} .

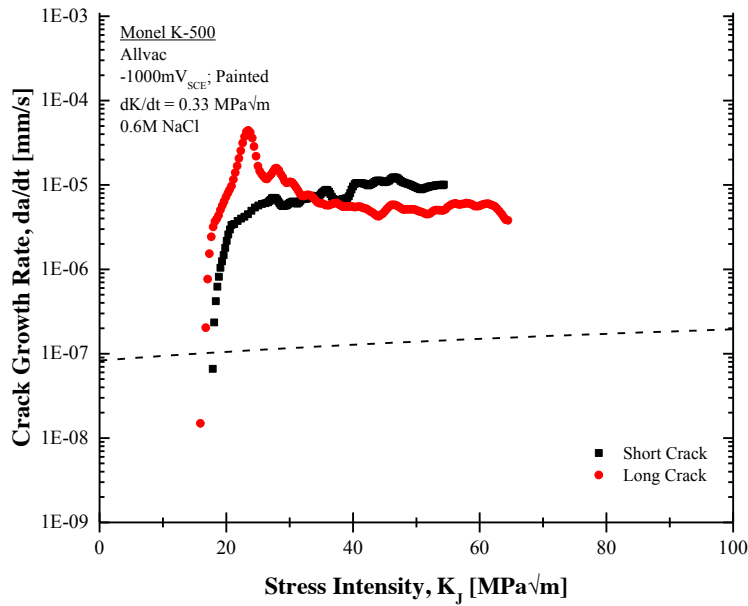
Setting Y equal to COD_{Max} gives the maximum distance of possible surface contact, D_{SH} . Assuming COD_{Max} is half the grain size (the grain size of Allvac is given in Section 3.2 to be $14 \mu\text{m}$) yields COD_{Max} of $7 \mu\text{m}$. The D_{SH} values were calculated at a K of 20, 40, and $60 \text{ MPa}\sqrt{\text{m}}$ for Test 1, 2, and 3 on one Allvac sample at $-850\text{mV}_{\text{SCE}}$ (Figure A.1), Allvac at $-1000\text{mV}_{\text{SCE}}$ at short crack lengths around 1 mm (Figure A.6), and Allvac at $-1000\text{mV}_{\text{SCE}}$ at long crack lengths around 4 mm (Figure A.6); results are shown in Figure A.7. The calculated D_{SH} evident during the first test at short crack lengths in Allvac at $-850\text{mV}_{\text{SCE}}$ (Figure A.1) are similar to the D_{SH} values that occurred during testing at short crack lengths (1 mm) in Allvac at $-1000\text{mV}_{\text{SCE}}$ at a K of $20 \text{ MPa}\sqrt{\text{m}}$. This is consistent with similar shorting behavior that dissipated before a K of $10 \text{ MPa}\sqrt{\text{m}}$. The D_{SH} values for short cracks were smaller than those for long cracks during testing of two Allvac samples at $-1000\text{mV}_{\text{SCE}}$. This is expected as D_{SH} should increase with increasing crack depth.

The observation that D_{SH} increases with increasing crack length suggests increased shorting is occurring during testing at long cracks compared to testing at short cracks. This may

affect the measurement of HEAC kinetics when testing on long cracks. However, significant shorting that persisted into the onset of actual crack growth was not observed during testing on Allvac material at $-1000\text{mV}_{\text{SCE}}$ with a long (4 mm) precrack (Figure A.6(a)). This suggests that effects from shorting is not the cause of the abnormal HEAC kinetics observed in Figure A.1 at low stress intensities in Test 2 and Test 3. However, it is possible that the fracture surface features developed during the first test on the Allvac sample are of greater height than those created during a fatigue precrack protocol. This may lead to fracture surface contact which would occur in subsequent HEAC tests that would not occur if the sample was simply fatigued to reach identical crack lengths. Additional work is needed to study how the average fracture surface feature height varies with crack growth mechanism and how that affects the observed shorting.



(a)



(b)

Figure A.6: Measured da/dt data from two slow K-rise (0.33 MPa√m) tests done on two Allvac SEN(T) samples in 0.6 M NaCl at -1000mV_{SCE} at short and long crack lengths (a) before and (b) after the applied linear shorting correction.

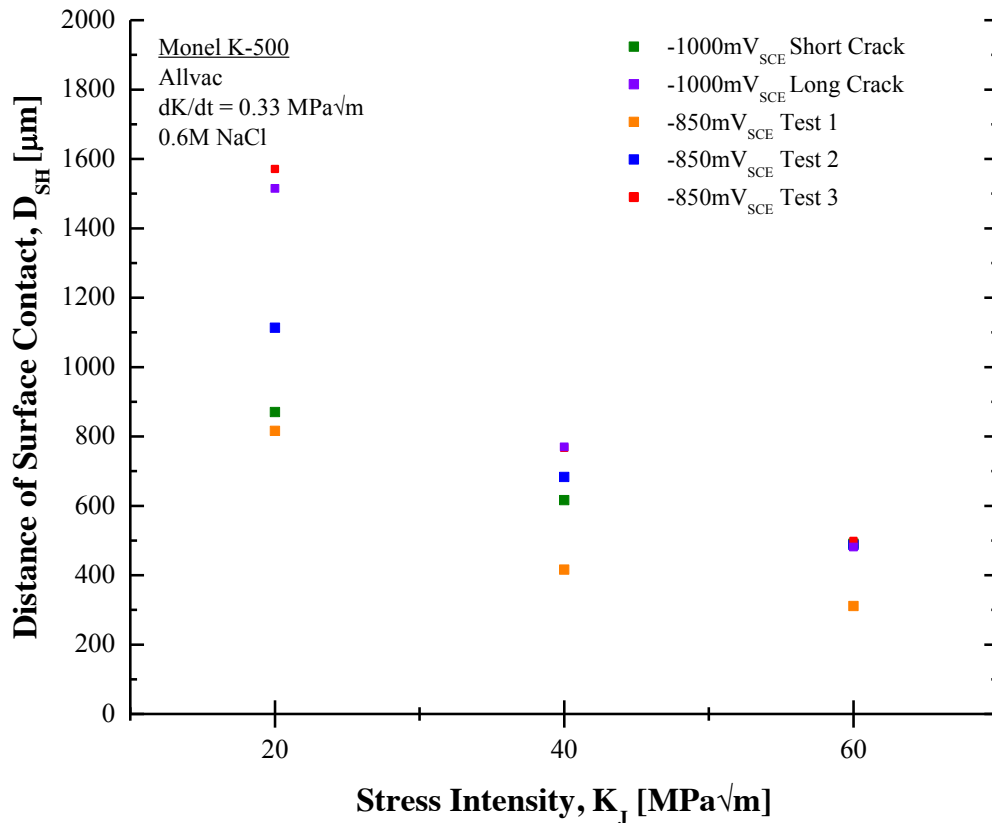


Figure A.7: D_{SH} calculated from crack depth and loading conditions during Test 1 (1.0 mm), Test 2 (2.9 mm), and Test 3 (7.2 mm) on one Allvac sample tested at -850mV_{SCE} , one Allvac sample tested at -1000mV_{SCE} at short crack lengths (1.0 mm), and one Allvac sample tested at -1000mV_{SCE} at long crack lengths (4.0 mm).

A.1.ii Effect of Mechanics on the Crack Depth Dependent Behavior

A.1.ii.(a) Inert Environment Testing

In order to isolate the effect of mechanics on the crack depth dependent behavior, testing was conducted on a TR3 SEN(T) sample in inert environment (dry N_2 gas) fatigue pre-cracked to short (1.0 mm) and long (4.0 mm) crack lengths. Inert environment testing precludes the influence of crack tip chemistry and crack wake shorting. Additionally, no difference in crack growth retardation load-history effects during the second test would be expected. The fatigue precrack protocol described in Section A.1 sharing identical K_{max} values and appropriate K-shed

protocols in line with other precrack procedures used in other tests and described in Section 2.2 were used to ensure the same plastic zone size ahead of the crack tip at the beginning of both tests. The first test at small crack lengths in Figure A.8 shows similar cracking kinetics established for TR 1, TR 2, and Allvac aged Monel K-500 materials in inert environment testing. During the second test, slightly higher da/dt values were measured in the K regime of 28 $\text{MPa}\sqrt{\text{m}}$ to 45 $\text{MPa}\sqrt{\text{m}}$, ending with slightly lower measured da/dt in the 55 $\text{MPa}\sqrt{\text{m}}$ to 75 $\text{MPa}\sqrt{\text{m}}$ regime. Measured da/dt above 30 $\text{MPa}\sqrt{\text{m}}$ is higher than the resolution limit, suggest real crack growth occurred during both tests. The crack lengths ranged from 1.136 mm to 1.265 mm during the first test and 3.593 mm to 3.764 mm during the second test, meaning roughly the same amount of crack growth occurred in both tests.

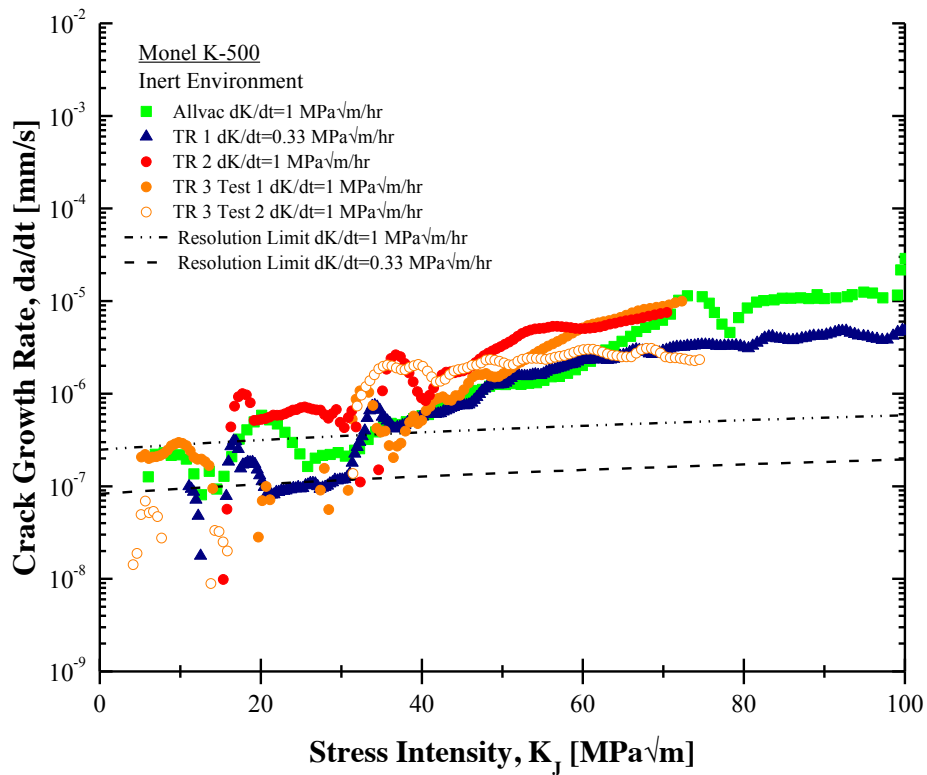


Figure A.8: Measured da/dt data from two slow K -rise ($1 \text{ MPa}\sqrt{\text{m}}$) testing done in TR 3 material in inert N_2 environment on a short (1.1 mm) crack and a long (3.6 mm) crack. The residual humidity was below 2% for the test duration. The measured da/dt of tests on TR 1, TR 2, and Allvac materials when tested in inert environments at short crack lengths is also included.

While the crack growth trends between Test 1 and Test 2 for TR 3 in inert environment testing in Figure A.8 are similar to those observed in Figure A.2, comparison of these data with a larger data-base of inert environment test results suggests that the differences in crack growth behavior observed between short cracks and long cracks is within the bounds of test-to-test variation. Figure A.8 shows the crack growth measured in TR 3 when tested in inert environments for short cracks (Test 1) and long cracks (Test 2) do not range outside the crack growth rate measured for TR 1, TR 2, or Allvac in inert environment at short cracks.

A change in fracture surface morphology between Test 1 and Test 2 on TR 3 in inert environment was observed (Figure A.9). During Test 1, crack growth was due to a time-dependent microvoid (transgranular) cracking similar to what was observed in the Allvac, TR 1, and TR 2 material during inert environment testing and described in detail in Section 3.1.1. The characteristic microvoids with embedded titanium carbides are circled in red in Figure A.9(c). During Test 2, however, fractography in Figure A.9 revealed a slightly different transgranular morphology with no microvoids present. The reason for this change in crack growth behavior is not well understood.

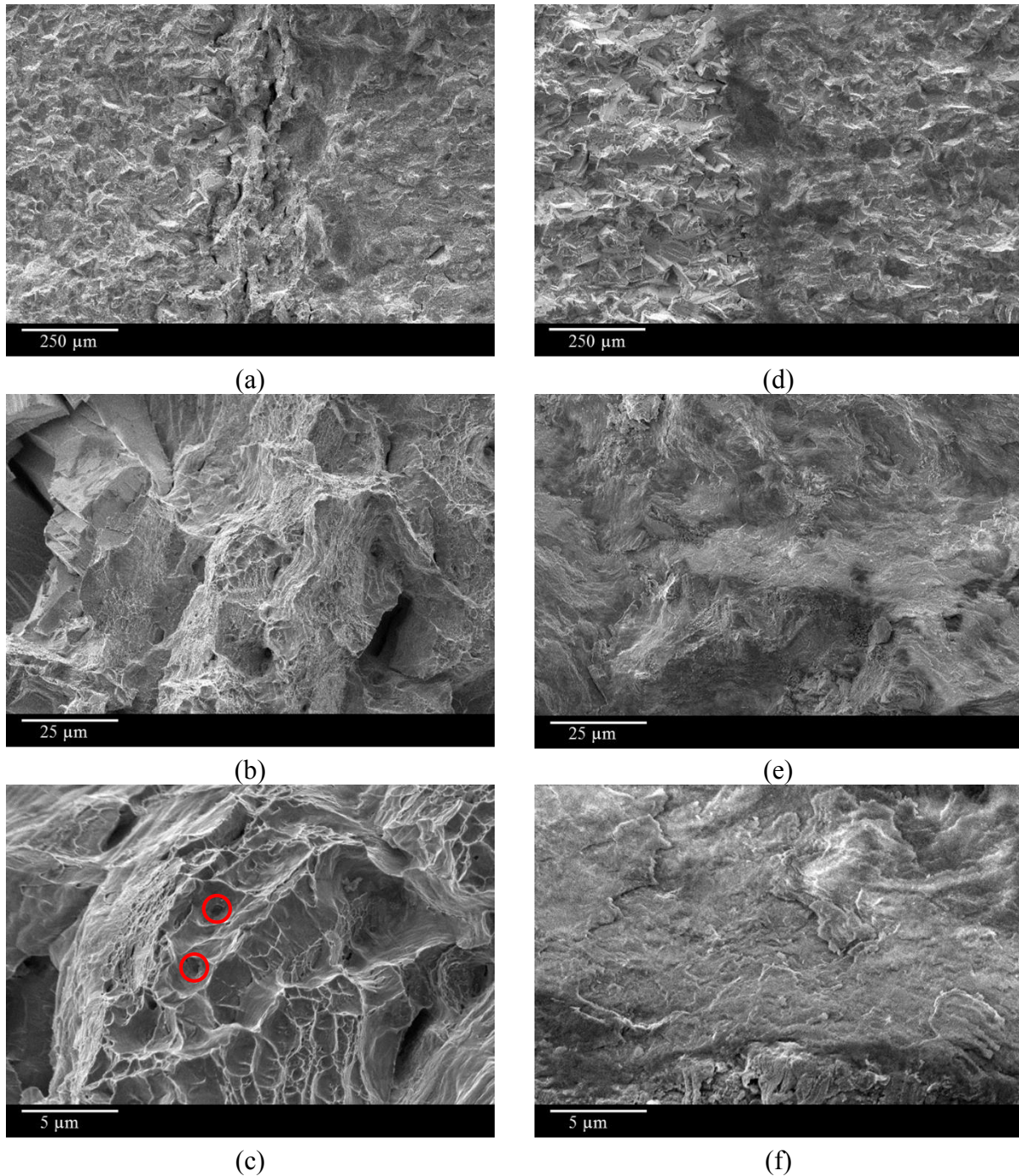


Figure A.9: Fractography of TR 3 in inert environment testing (a-c) at short crack lengths (1.1 mm) and (d-f) long crack length (3.6mm). The red circles in (c) point out embedded titanium carbides at the bottom of the microvoids.

A.1.ii.(b) Crack Depth Dependent Crack Tip Plasticity

The difference in crack growth behavior between Test 1 and Test 2 on a TR 3 sample in

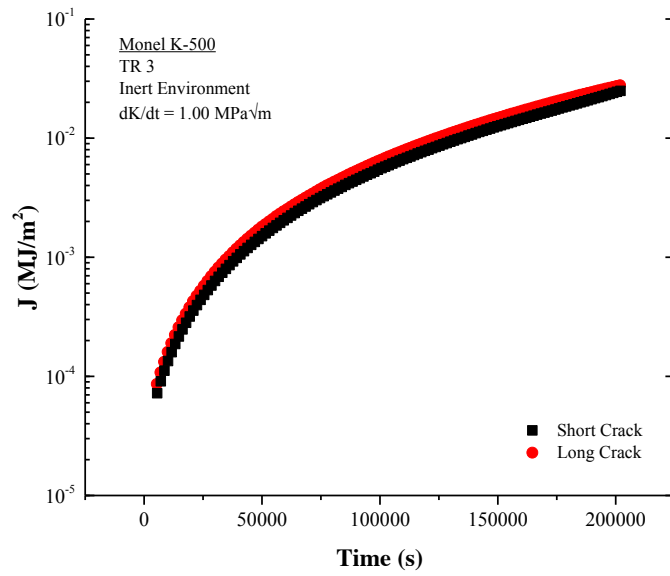
inert environment (Figure A.9) may be due to variation in the amount of plasticity at the crack tip. In order to investigate this possibility, J_{plastic} analysis was carried out for both tests. J_{plastic} can be calculated from the crack length and loading conditions as

$$J_{\text{Plastic}} = \frac{\alpha \sigma_0^2}{E} a \frac{(W-a)}{W} h_1(n, a/W) \left(\frac{P}{P_0} \right)^{n+1} \quad (\text{A.1})$$

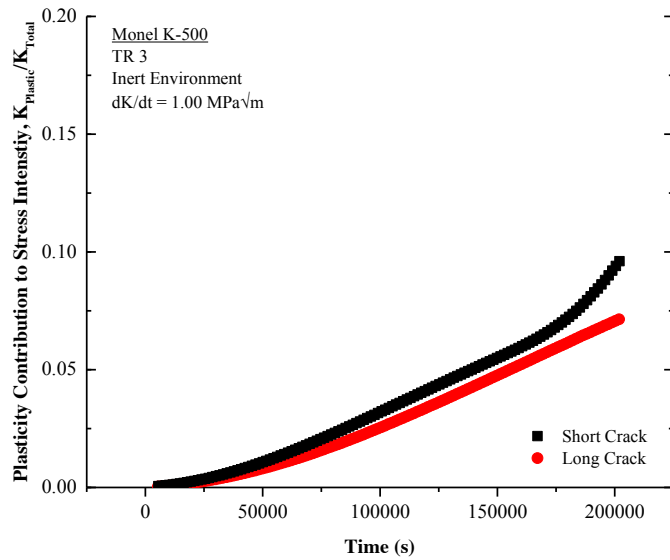
where h_1 is a geometric and hardening function, P is load, α and n are the afore-mentioned Ramberg-Osgood flow rule constants and was determined to be 0.39 and 20 respectively for the Allvac material, and P_0 is the limit load for net plastic deformation in the remaining ligament [75]. The h_1 for a free-rotating SEN specimen was defined using a sixth order polynomial fit to discrete values, excluding negative h_1 values [8, 75]. P_0 is given by

$$P_0 = \beta \left(\sqrt{1 + \left(\frac{a}{W-a} \right)^2} - \left(\frac{a}{W-a} \right) \right) (W-a) B \sigma_0, \quad (\text{A.2})$$

where β is 1.455 for plane strain and B is thickness [69]. In this analysis, the strengthening constants from Table 2.2 were used ($\sigma_{\text{YS}} = 795$ MPa, $\alpha = 0.37$, and $\eta = 23$). The results, shown in Figure A.10, indicate there is no difference in the plasticity experienced during the second test at long crack lengths than at short crack lengths. The tests were executed at a constant dK/dt of 0.33 MPa $\sqrt{\text{m/hr}}$ starting at a K of 10 MPa $\sqrt{\text{m}}$. Thus, plotting versus time in Figure A.10 is appropriate since similar stress intensities and crack growth occurred in both tests at a given test time. The plasticity-related portion of total stress intensity, $K_{\text{Plastic}}/K_{\text{Total}}$ was also calculated using the results in Figure A.10. The results, shown in Figure A.10 (b) demonstrate K_{Plastic} was consistent across both tests, with the maximum $K_{\text{Plastic}}/K_{\text{Total}}$ achieved being 0.09 and 0.07 in Test 1 (short crack) and Test 2 (long crack) respectively, suggesting the crack length difference did not affect the level of plasticity at the crack tip. Therefore, the change in crack behavior in Figure A.9 is not due to variation in crack tip plasticity damage.



(a)



(b)

Figure A.10: (a) Plasticity at the crack tip calculated from loading conditions and crack length for two fracture mechanics tests on a single TR3 sample in inert, N₂ environment and (b) its contribution to K_{Total} .

A.1.ii.(c) Load History Effects in an Aqueous Environment

In order to investigate possible load history effects, fracture mechanics tests were carried out on two separate specimens. Slow K-rise ($0.33 \text{ MPa}\sqrt{\text{m/hr}}$) testing was completed on two Allvac samples that were precracked to a short (1 mm) and long crack length (4 mm) in 0.6M NaCl at $-1000\text{mV}_{\text{SCE}}$; the results are seen in Figure A.6. The crack lengths studied were selected to cover the range of crack lengths in the three tests done on one Allvac sample at $-850\text{mV}_{\text{SCE}}$ (Figure A.1).

In the short crack specimen, initial shorting is evident between a K_I of 0 and $17 \text{ MPa}\sqrt{\text{m}}$ as a sharp linear decrease in $\log(\text{da}/\text{dt})$ with increasing K (Figure A.6(a)). This is similar to what has been historically observed at short cracks in this project and in other work completed by Gangloff et. al. [8]. A similar feature is observed for the long crack specimen prior to a K of $16 \text{ MPa}\sqrt{\text{m}}$, demonstrating the fracture surface shorting had dissipated before the onset of intergranular fracture. This suggests that the slow decreases observed in Figure A.1, for Test 2 and 3 on one Allvac sample tested at $-850\text{mV}_{\text{SCE}}$ are not caused by a crack wake electrical contact based phenomenon, as discussed in Section A.1.i. Applying the shorting correction protocol (described in Section 2.5) yields the data reported in Figure A.6(b). Following this initial stage of shorting, the long crack sample shows increased measured da/dt compared to the short crack specimen that eventually transitions to slower cracking than what was measured at small crack lengths.

The peak in da/dt measured during testing at long crack lengths in the 20 to $30 \text{ MPa}\sqrt{\text{m}}$ stress intensity range may be a result of a non-straight crack front developed during the fatigue precrack protocol. Normally, the precrack protocol produces a sharp crack with a straight crack front, as shown for the short crack testing in Figure A.11 (a). During long crack testing, the crack front pinned on one side of the sample, as shown in Figure A.11 (b). This lead to a stage of increased HEAC crack growth during which the crack front Section that was “lagging” behind catches up to form a straight crack front. Once the straight crack front was established, crack growth slowed to levels characteristic of Allvac under cathodic polarization of $-1000\text{mV}_{\text{SCE}}$. Another consequence of the initial non-straight crack front is that the calculated stress intensity is no longer valid, since the theoretical K solution and Johnson equation used to calculate the crack length from the direct current potential drop (dcPD) probes assume a straight crack front. Thus,

K_{TH} during the test at long crack lengths may not be accurate. Nevertheless, by the end of the test, the crack front is straight, suggesting the measured da/dt_{II} crack growth rates are reliable.

The transition from faster cracking at long crack depths in the early K regime to slower cracking at long crack depths in the high K regime in Figure A.6 is similar to the HEAC behavior between Test 1 and Test 2/Test 3 at $-850mV_{SCE}$ carried out on the same specimen in Figure A.1. However, the non-straight crack front achieved during testing of the Allvac material at long cracks compromises the data in the early K regime. Thus, it is not clear whether the crack length dependent HEAC behavior evident in Figure A.1 is due to the longer crack length or if it is an artifact of testing conditions, specifically being due to the presence of load history effects from previous slow rising dK/dt testing (Figure A.1) or due to a straight versus non-straight crack front (Figure A.6).

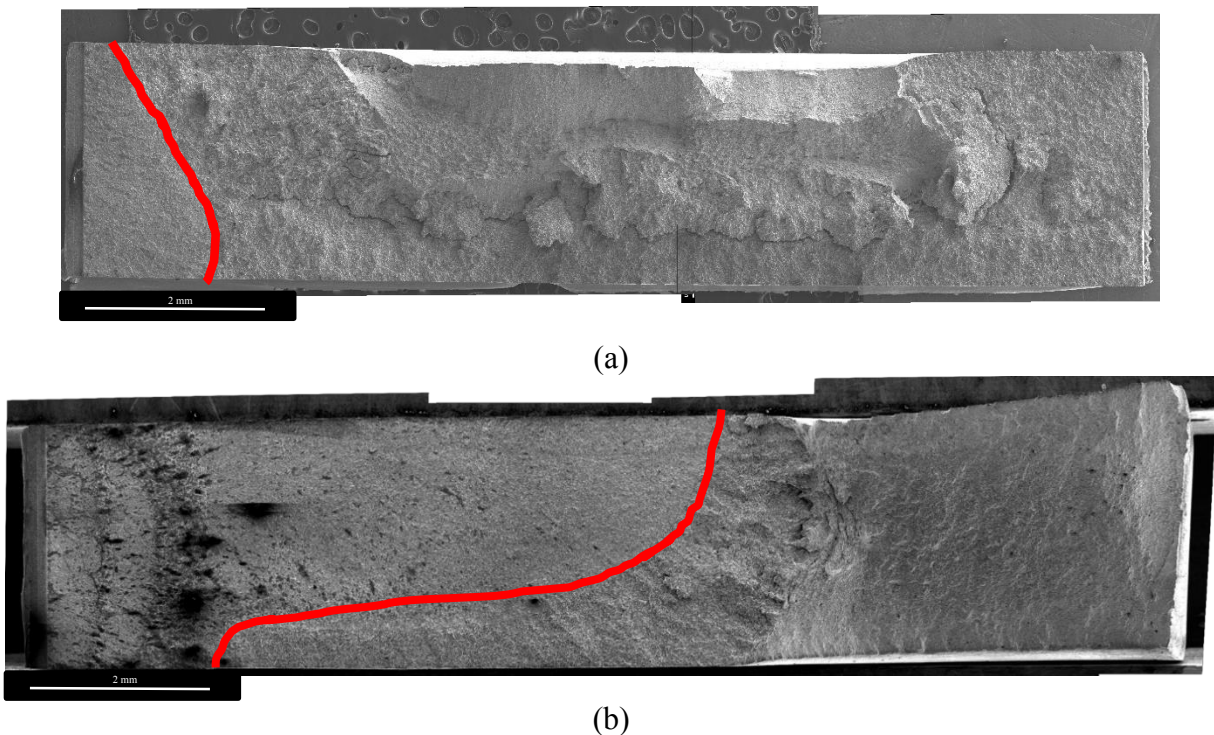


Figure A.11: fracture surface for (a) short crack testing and (b) long crack testing of Allvac aged Monel K-500 material at $-1000mV_{SCE}$. The crack front after the precrack is outlined on both fracture surfaces.

A.2 Effect of Crack Tip Chemistry on the Crack Depth Dependent Behavior

The increased area of intergranular fracture of higher crack lengths in Figure A.2 and Figure A.3 suggests a more significant role of hydrogen embrittlement, thus a higher

overpotential for H production, for the longer crack lengths. As discussed in the main text and in Appendix B, the overpotential for H-production is critically dependent on the crack wake channel geometry, which will change for identical rising dK/dt tests with different starting crack lengths [8]. This possibility is investigated both experimentally as well as via calculations of the diffusible H concentration expected for various crack channel geometries.

Slightly lower da/dt_{II} crack growth rates of 1.0×10^{-5} and 5.6×10^{-6} m/s were measured during testing at small crack lengths and long crack lengths respectively on two separate Allvac samples tested at -1000mV_{SCE} (Figure A.6). This may be due to difference in crack tip chemistry, which changes as a function of crack depth and crack opening displacement, and is represented by either the ratio x^2/G or x/G , where x is the shortest distance between the crack tip and the bulk solution and G is the average crack opening displacement [8]. It is still debated whether the crack tip chemistry follows an x^2/G or x/G relationship; however, a comparison between the crack geometries associated with a short crack versus a long crack can be informative in either case. In this study, x^2/G was used to describe the crack geometry.

The distance between the crack tip and the bulk solution, x , is equivalent to either the crack length or half of the specimen thickness, whichever quantity is smaller. Thus, once the crack length exceeds half the specimen thickness, or 1.35 mm, x remains constant. The average crack opening displacement can be calculated by averaging the crack mouth opening displacement and crack tip opening displacement, both of which can be calculated from loading conditions and crack depth as described in Section A.1.i [69, 70]. During testing at short crack lengths, the crack length ranged from 1.19mm to 4.33mm as K increased from $10 \text{ MPa}\sqrt{\text{m}}$ to $54 \text{ MPa}\sqrt{\text{m}}$. This correlates to x^2/G ranging from 9.6 cm to 83.4 cm throughout the test duration. For the long crack sample, the crack length ranged from 3.99 mm to 7.90 mm as K increased from $10 \text{ MPa}\sqrt{\text{m}}$ to $64 \text{ MPa}\sqrt{\text{m}}$, correlating to x^2/G ranging from 75.3cm to 176.7 cm.

The da/dt_{II} measurements are taken from a K of $54 \text{ MPa}\sqrt{\text{m}}$ and a crack length of 4.33 mm for the short crack test and from a K of $60 \text{ MPa}\sqrt{\text{m}}$ and a crack length of 7.68 mm for the long crack test. This corresponds to an x^2/G of 83.4 cm for the test at short crack lengths and 176.7 cm for the test at long crack lengths. Figure A.12 plots an empirical relationship developed by Scully et al, relating the applied potential to the crack tip diffusible H, C_{H-Diff} , for various crevice geometries described by the x^2/G given in the figure [8]. The red line in Figure

A.12 shows the C_{H-Diff} versus applied potential relationship for an x^2/G of 83.4, reflecting the short crack geometry when da/dt_{II} was measured. The blue line in Figure A.12 shows the C_{H-Diff} versus applied potential relationship for an x^2/G of 176.7, reflecting the long crack geometry when da/dt_{II} was measured. This data suggests that at $-1000mV_{SCE}$, the x^2/G values of interest correlate with C_{H-Diff} quantities of 16 ppm and 15 ppm for short crack and long crack geometries, respectively. This small difference in C_{H-Diff} for the longer crack length does not explain the slower da/dt_{II} observed for the longer cracks in Figure A.6 and Figure A.1 at high K values near $60 MPa\sqrt{m}$. In addition, it is not consistent with the increased role of hydrogen embrittlement as crack length increases evident in Figure A.2 nor is it consistent with the increased da/dt shown at long crack lengths in Figure A.6 and Figure A.1 at early K values. This analysis suggests that the observed behavior in Figure A.1 is not consistent with the expected changes in crack tip chemistry for short versus long cracks.

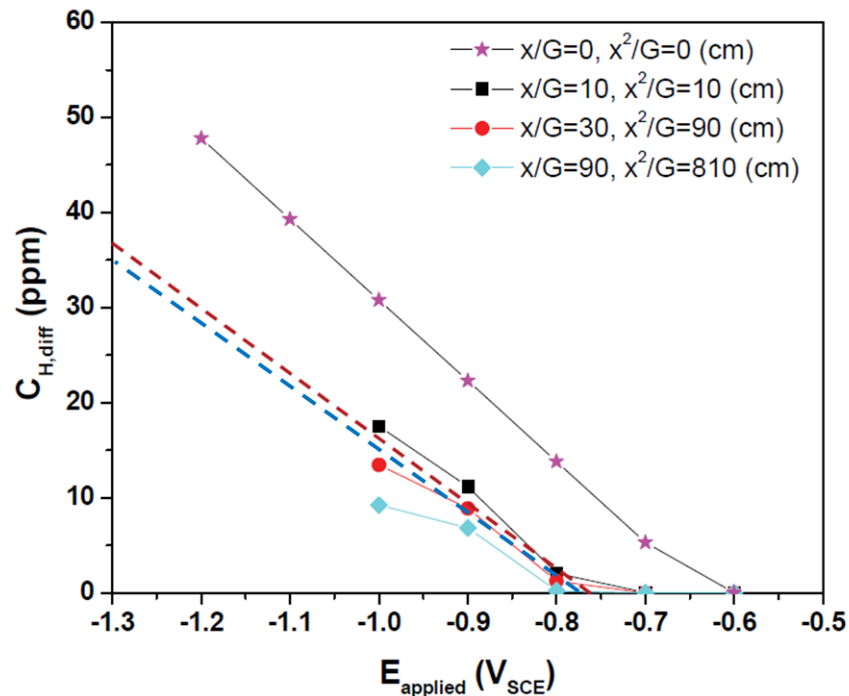


Figure A.12: C_{H-Diff} as a function of crack geometry at several applied potentials. The red dotted line indicates expected C_{H-Diff} values for a short crack length. The blue dotted line indicates expected C_{H-Diff} values at long crack lengths.

A.3 Conclusions

Multiple HEAC tests on a single Allvac SEN(T) sample run at $-850\text{mV}_{\text{SCE}}$ demonstrated a lack of similitude between identical slow K-rise testing started at different crack lengths. Specifically, a lower threshold stress intensity for crack growth, accelerated crack growth in the 10 to 50 $\text{MPa}\sqrt{\text{m}}$ range, and lower da/dt_{II} were observed in subsequent tests (Test 2-3) than in the first test (Test 1). Additionally, fracture surface analysis showed a higher degree of IG-HEAC in Test 2-3 as compared to a more ductile/transgranular appearance in Test 1. Several potential mechanisms were investigated including crack wake surface contact, mechanistic effects from the load history associated with the previous slow K-rise, variation in crack tip plasticity as a function of crack length, and the effects of crack tip chemistry, which is known to change with crack depth.

The crack depth dependent HEAC behavior was investigated by analyzing differences in crack wake surface contact, possible load history effects, variations in crack tip plasticity as a function of crack length, and crack tip chemistry. None of the potential mechanisms investigated in this project stood out as conclusive mechanistic causes for the behavior observed in consecutive slow K-rise testing on a single Allvac sample at $-850\text{mV}_{\text{SCE}}$ (Figure A.1), though the comparison of tests on the Allvac material at $-1000\text{mV}_{\text{SCE}}$ for short and long cracks was compromised by effects of a non-straight crack front on the long crack specimen. Further study is required to provide a conclusive mechanism for the observed crack dependent HEAC behavior.

It remains a possibility that the non-IG crack growth that occurred in the Allvac material at $-850\text{mV}_{\text{SCE}}$ is an anomaly with regard to the two additional K-rise tests executed on the same sample showing HEAC, previous work on the Allvac material that observed HEAC at the less cathodic potential of $-800\text{mV}_{\text{SCE}}$, and the lack of a conclusive mechanism for increased HEAC with increasing crack length [8]. However, the increased resistance of the Allvac material over TR 1, TR 2, and TR 3 material lots was observed in this study at both $-950\text{mV}_{\text{SCE}}$ and $-850\text{mV}_{\text{SCE}}$, and is consistent with work done in other projects, specifically the SSRT discussed in Section 3.1.3 and the H analysis discussed in Section 3.2.3. Therefore, the crack dependent HEAC behavior does not preclude the conclusion of increased HEAC resistance of Allvac compared to the other material lots in this study.

B: Accelerated Side Cracking

B.1 Observation of Enhanced Hydrogen Embrittlement near Specimen Surface

Testing conducted using the side masking protocol detailed in Section 2.2 exhibited uniform crack fronts which are necessary to ensure (1) rigorous application of the Johnson-equation to convert the dcPD signal to a crack depth and (2) accuracy of the K-solution of the SEN specimen. This testing protocol enabled investigation of the effect of heat-to-heat metallurgical differences on HEAC behavior, which is the primary objective of this thesis. Testing was also performed on specimens without the side lacquer and tape protection described in section 2.2; this configuration mimics the protocol used for the data reported in previous work where a uniform crack front was also observed [8]. The test matrix shown in Table B.1 was executed on specimens with no masking. Interpretation of these results was hampered by the onset of rapid cracking along either edge of the specimen. The cracking on either specimen flank was optically observed to extend from the main crack to the end of the specimen. Every test executed in 0.6M NaCl solution under cathodic polarization marked with an asterisk in Table B.1 experienced this side cracking, which caused unexpected and unpredictable specimen failure before test completion. The only test that did not exhibit side cracking was Allvac at -850mV_{SCE}, which did not experience any crack growth due to HEAC. While a conclusive mechanistic description of this behavior is outside the scope of the current effort, this appendix aims to document the observed behavior and discuss potential causes of this behavior in the context of the HEAC mechanism.

Table B.1: Testing matrix of SEN(T) specimens without painting the sides. An “X” denotes the test was run, an asterisk denotes the test was shortened due to the onset of accelerated side cracking. All tests run under cathodic protection were executed in 0.6M NaCl solution.

Potential	Material			
	Allvac	TR1	TR2	TR3
-1000mV _{SCE}	X*		X*	
-950mV _{SCE}		X*	X*	
-850mV _{SCE}	X	X*		
Inert Environment	X	X	X	X

Typical fractography of the failed specimens is shown in Figure B.1. On the left edge is the EDM notch, followed by an area of mixed transgranular slip-base cracking associated with

the fatigue precrack that extends to the first blue line. Beyond this point the yellow highlighted regions represent areas where IG cracking was observed. In the region between the two blue lines shown in Figure B.1, intergranular cracking occurred during the K-rise at crack growth rates similar to what was measured in other samples with the side tape protection present and is also similar to rates presented in the literature, as shown in Figure B.2 [8]. In this region, optical observation of the specimen surface did not show cracking along the crack flanks. However, beyond this point, there is pure intergranular cracking along the broad sides and back of the specimen. The IG cracking at the back of the specimen was observed to occur near the end of test after the side cracks had progressed along the entire specimen width. It is likely that at this stage in the test, the normally compressive stresses in the back of the SEN(T) specimen were tensile. The intergranular cracking suggests extensive hydrogen embrittlement emanating from the specimen's broad surfaces that dominates the H-production and crack growth at the crack tip. Final specimen failure occurred in the central grey region in Figure B.1, which fractography revealed to be ductile failure. When observed, the onset of side cracking began at test times between 86 and 118 hours, with the average onset time of 105 hours. This corresponds to a typical stress intensity of $44 \text{ MPa}\sqrt{\text{m}}$ applied to the main crack when side cracking begins, as governed by the dK/dt of $0.33 \text{ MPa}\sqrt{\text{m/hr}}$ used during the test (note the K rise started at $10 \text{ MPa}\sqrt{\text{m}}$). Moreover, the onset time for side cracking did not scale with applied potential, as evident in Table B.2.

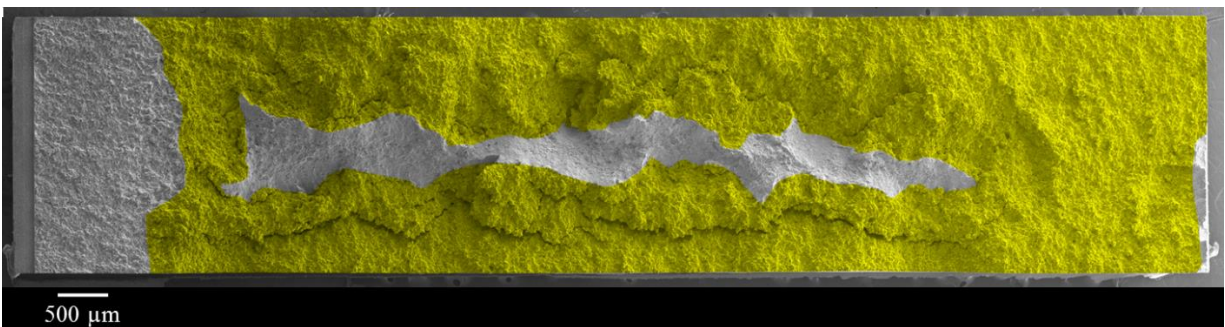
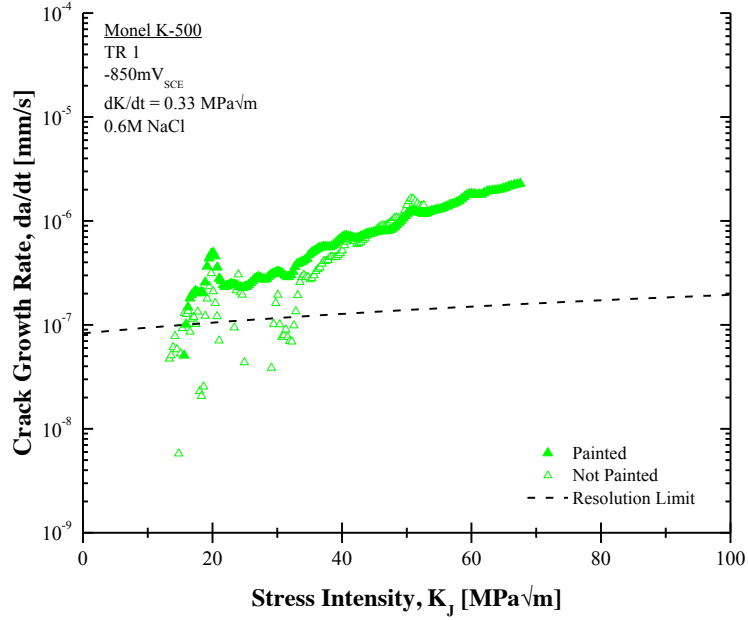
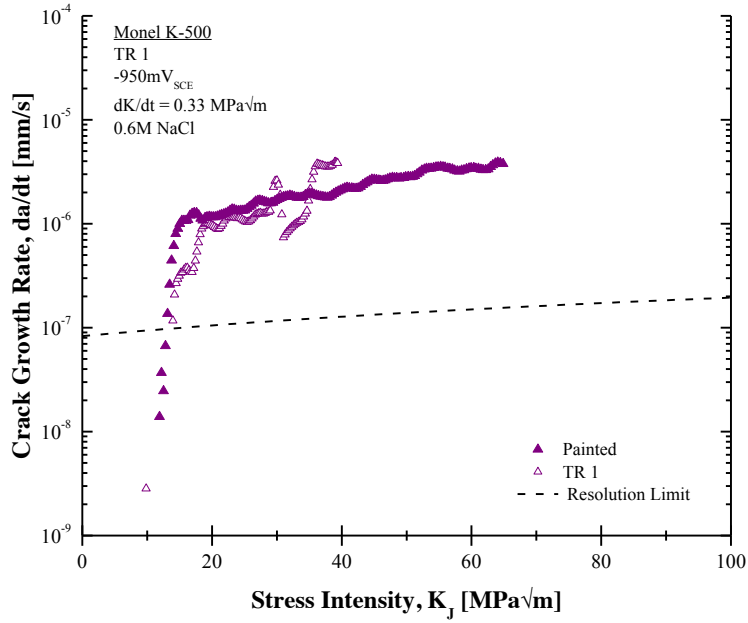


Figure B.1: Fractography of a TR1 sample tested in 0.6M NaCl at $-950\text{mV}_{\text{SCE}}$. The area highlighted in yellow is where intergranular surface morphology is observed. The area in between the blue vertical lines signifies the section of normal intergranular crack growth.



(a)



(b)

Figure B.2: crack growth measurement of (a) TR 1 at $-850\text{mV}_{\text{SCE}}$ for a painted and not painted specimen and (b) TR 1 at $-950\text{mV}_{\text{SCE}}$ for a painted and not painted specimen. The non-painted specimens are truncated at the point where the side-cracking began.

The fractography of a TR2 sample tested at $-850\text{mV}_{\text{SCE}}$ with the tape masking, shown in Figure B.3, provides further insight. At the end of this test, side cracking occurred despite the implementation of the side masking (this is the lone instance of side-cracking in masked specimens). Fractography revealed mixed intergranular/transgranular cracking in the middle of the specimen, in the region shaded blue, similar to what was observed in TR1 and TR3 specimens at $-850\text{ mV}_{\text{SCE}}$ with masking. Steady-state crack growth rate, da/dt_{II} of $4.4 \times 10^{-6}\text{ mm/s}$ were measured at a K of $60\text{ MPa}\sqrt{\text{m}}$, similar to the growth rates of $1.8 \times 10^{-6}\text{ mm/s}$ and $3.2 \times 10^{-6}\text{ mm/s}$ measured in TR1 and TR3 respectively. Furthermore, there is a consistent fracture surface morphology showing mixed intergranular/transgranular growth in all three material lots in the fractography comparisons shown in Figure B.3. However, testing during the TR2 test also produced a region of pure intergranular fracture along the sides of the specimen, highlighted in yellow in Figure B.3. As previously argued, the mixed intergranular/transgranular morphology is indicative of conditions where there are mild amount of $C_{\text{H-Diff}}$ thus marginal HEAC, whereas the pure IG that is observed for the side-cracking suggests a greater level of hydrogen embrittlement.

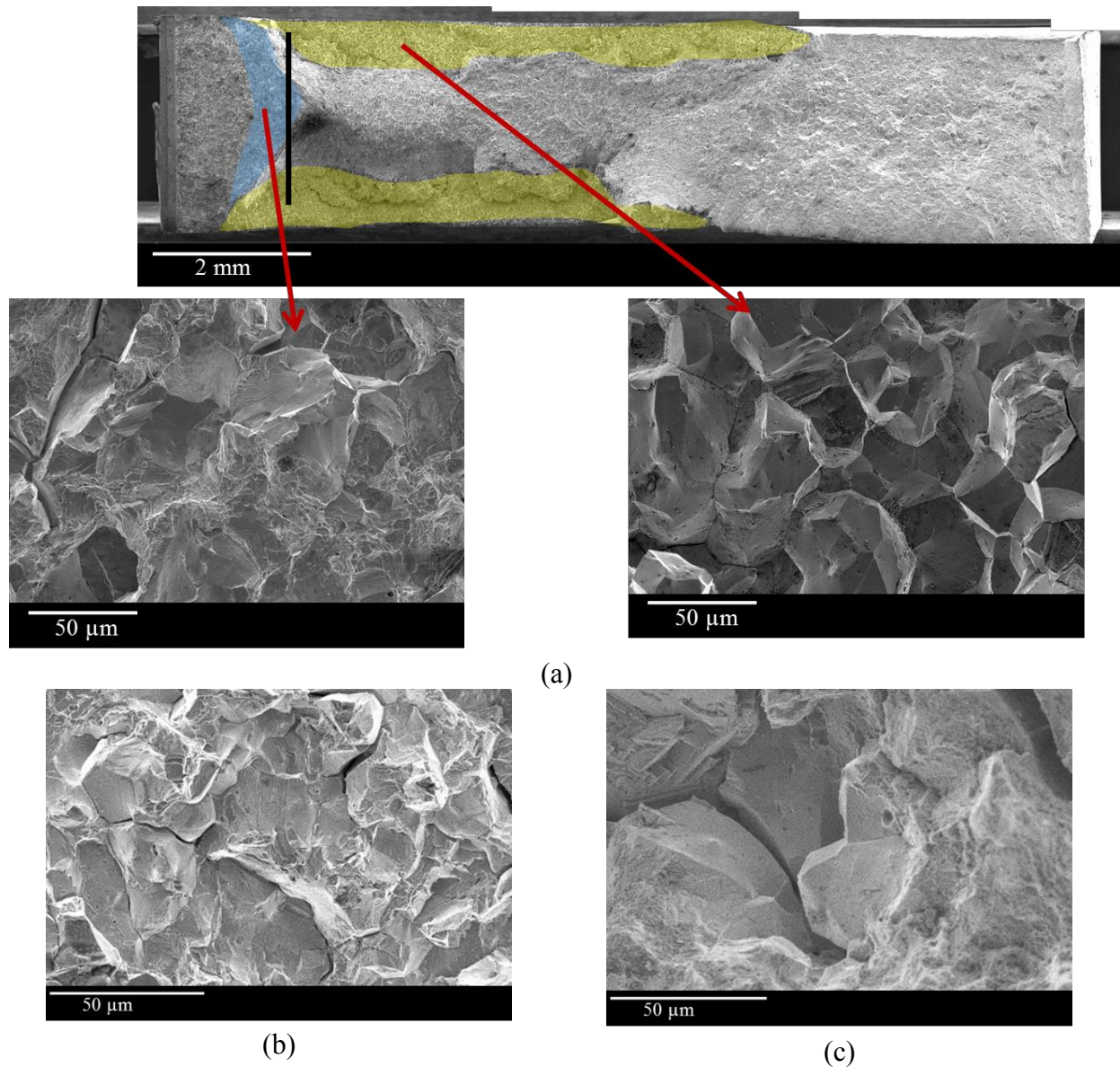
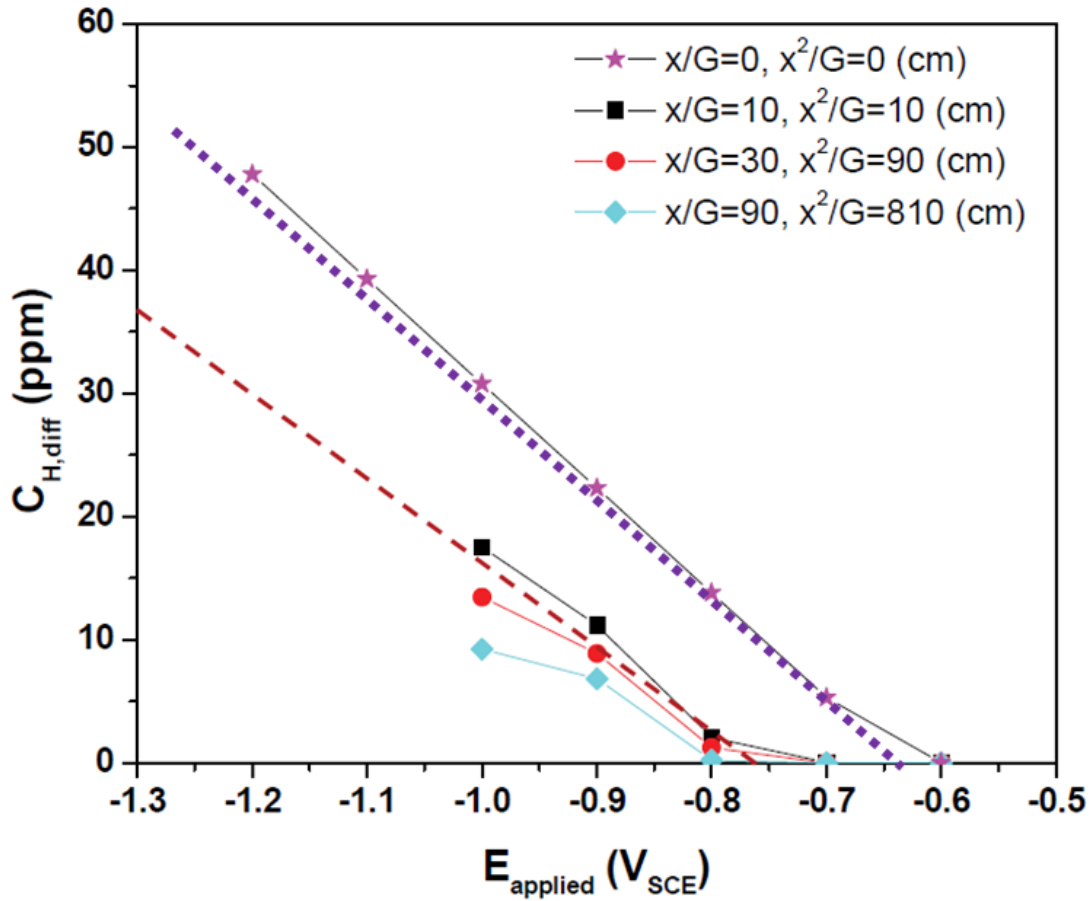


Figure B.3: Fractography of (a) TR2 at the crack tip near the center of the specimen width and near the specimen surface, (b) TR1, and (c) TR3 at $-850\text{mV}_{\text{SCE}}$ with side masking implemented.

B.2 Hydrogen Production at the Surface

Previous work has demonstrated that the chemistry at the bold surface will result in a higher overpotential for H-production than at the crack tip, resulting in a higher concentration of diffusible hydrogen, $C_{\text{H-Diff}}$, at the bold surface than in artificial crevices of various depth [8, 12]. B.4 shows the variation in $C_{\text{H-Diff}}$, with an x^2/G of 0 representing the bold surface and the red dotted line showing typical $C_{\text{H-Diff}}$ concentrations at various applied potentials for a typical mode

I crack, when side cracking does not occur. Typically, C_{H-Diff} at the bold surface is 2-3 times higher than at the crack tip. It is hypothesized that for SEN-HEAC testing of Monel K-500 in 0.6M NaCl under cathodic polarization this difference in H-production is overwhelmed by the enhanced hydrostatic stresses at the center of the crack front. These enhanced stresses at the center of the crack front are due constraint, where maximum constraint occurs in the specimen center and the constraint dissipates along the crack front towards either surface edge of the specimen. This hypothesis is supported by the uniform crack front observed for unmasked specimens (Allvac Monel K-500) employing near-identical environmental testing conditions (albeit at a separate laboratory; Fatigue Technologies Associates) [8] and in the current side-masked specimens. However, the side-cracking behavior shown by the current non-masked specimen results suggest a strong role of the bold-surface charging. It is unclear why testing of the same lot (Allvac) Monel K-500 under identical environmental conditions results in a different relative influence of the bulk charging.



B.4: $C_{\text{H-Diff}}$ as a function of applied potential, E_{applied} established for the Allvac Monel K-500 material lot as a function of crack geometry described by x/G or x^2/G .

B.3 Side Cracking Kinetics

The rate of the side cracking cannot be measured from the dcPD potential readings, since both dcPD calculations of crack lengths and the K-solution accuracy are compromised by the non-straight crack front [71]. However, the time for the cracking to progress from the last data point at which the crack front is straight (this estimate is informed by optical observation of the crack front during the test), marked by the vertical line in Figure B.3, and the end of the test is known. This can be coupled with measurements of the area of IG on the fracture surface past the second vertical line in Figure B.3 to yield an average crack growth rate estimate for this phenomenon. The results of this analysis are shown in Table B.2. The growth rate estimates ranged from 1.1×10^{-4} mm/s to 5.3×10^{-4} mm/s for all tests in which side cracking was observed.

These rough estimates correlated with applied potential; faster crack growth rates for the side cracking coincided with higher cathodic polarizations for each material lot. This suggests that the crack growth rates for the side cracking increased with increased hydrogen charging. The crack growth rates of the side cracking are up to an order of magnitude faster than the da/dt_{II} measured at the respective applied potentials both in section 3.1.2 and the literature [8].

Table B.2: estimated crack growth rates for observed side cracking as well as the side crack initiation time and stress intensity for the main mode I crack at the start of side cracking.

Material	E_{applied} [mV_{SCE}]	Test Time for Start of Side Cracking [hours]	K at Start of Side Cracking [MPa√m]	Estimated Crack Growth Rate [mm/s]
TR 1	-850	118.3	53	1.1×10^{-4}
TR 1	-950	95.0	39	5.3×10^{-4}
TR 2	-950	86.6	41	1.5×10^{-4}
TR 2	-1000	114.9	67	3.1×10^{-4}

B.4 Hydrogen Diffusion Modeling

Intergranular cracking along the sides was measured on the fracture surfaces to penetrate between 100 to 1200 μm from the edge of the specimen. It is critical to understand the extent to which hydrogen adsorbed on the bold surfaces affects the side-cracking behavior. A clear understanding of the hydrogen diffusion distances achieved during the fracture test duration provides insight into the mechanism that governs the side cracking behavior. Two models were used to evaluate hydrogen diffusion during testing from the bold surfaces.

The first model, Model A, predicts hydrogen diffusion concentrations at a given penetration distance, x , from the surface. It assumes the specimen is infinitely wide; thus, hydrogen adsorption and diffusion is only occurring at one surface. It also assumes the surface concentration of hydrogen, C_s , is constant. This becomes especially important if the charging conditions lead to hydrogen diffusion distances greater than half the specimen width. In this case, hydrogen from either flank would contribute to the hydrogen concentration in the center of the specimen, causing concentration predictions from Model A to become inaccurate. Both models assume 1-D diffusion at along the crack growth plane only (at height $y=0$). The fact that

the masking successfully prevents or delays the side cracking suggests that additional contributions from above and below the crack growth plane may be important. However, this diffusion was not included in this modeling.

These assumptions correspond to linear diffusion into a semi-infinite medium, the solution of which is

$$\frac{C[x,t]}{C_s} = \operatorname{erfc}\left(\frac{x}{2\sqrt{D_{\text{eff}}t}}\right) = \operatorname{erfc}(\eta), \quad (\text{B. 1})$$

where t [s] is the charging time experienced by the sample, D_{eff} [cm^2/s] is the effective diffusivity of hydrogen, and η equals $x/2\sqrt{D_{\text{eff}}t}$ [99]. When $C[x,t]/C_s = 0.16$, $\eta=1$, yielding the convenient and often-used estimate for hydrogen diffusion distance, $x = 2\sqrt{D_{\text{eff}}t}$. The charging time of the specimen is equivalent to the test time plus the time between the potential being applied and the start of the test, typically 1 to 2 hours. For the purposes of the diffusion analysis, the charging time was taken to be the average test time to the onset of side cracking calculated from Table B.2 plus 2 hours to account for test setup time, yielding 106 hours. For this charging time, the first order $x = 2\sqrt{D_{\text{eff}}t}$ estimate predicts a hydrogen penetration depth of 87 to 140 μm for D_{eff} values of 5.0×10^{-11} and 1.3×10^{-10} cm^2/s respectively. Table B.3 shows the charging time necessary to reach various hydrogen concentrations at a penetration depth of 87 μm .

Table B.3: Charging time to reach various hydrogen concentrations at a penetration depth of 87.23 μm predicted using Model A. A value of $5.0 \times 10^{-11} \text{ cm}^2/\text{s}$ was used for D_{eff} .

C/C_0 at x [%]	$\text{Erf}[\eta]$	η	$x[\mu\text{m}]$	t [s]	t [h]
95	0.05	0.045	87.23	1.88E+08	52190.1235
90	0.1	0.085	87.23	5.27E+07	14627.6817
80	0.2	0.18	87.23	1.17E+07	3261.8827
70	0.3	0.275	87.23	5.03E+06	1397.4876
60	0.4	0.37	87.23	2.78E+06	771.9869
50	0.5	0.48	87.23	1.65E+06	458.7023
40	0.6	0.595	87.23	1.07E+06	298.5241
30	0.7	0.735	87.23	7.04E+05	195.6314
25	0.75	0.815	87.23	5.73E+05	159.1102
20	0.8	0.905	87.23	4.65E+05	129.0376
19	0.81	0.93	87.23	4.40E+05	122.1933
18	0.82	0.95	87.23	4.22E+05	117.1025
17	0.83	0.97	87.23	4.04E+05	112.3233
16	0.84	1	87.23	3.80E+05	105.6850
15	0.85	1.015	87.23	3.69E+05	102.5844
1	0.99	1.825	87.23	1.14E+05	31.7313
0.5	0.995	1.985	87.23	9.66E+04	26.8221

The second model, Model B, is for a specimen of finite length, accounting for diffusion from either bold surface of the specimen simultaneously. Due to the shorter diffusion length, diffusion studied across the specimen thickness (around 2.75 mm) rather than across the specimen width (around 12.5 mm). It also assumes the hydrogen concentration at either surface, C_s , is constant. The solution for this diffusion problem is given in the literature to be

$$\frac{C}{C_s} = 1 - \frac{4}{\pi} \sum_{n=0}^{\infty} \frac{(-1)^n}{2n+1} \exp\left\{ \frac{-D_{\text{eff}}(2n+1)^2 \pi^2 t}{4l^2} \right\} \cos\left(\frac{(2n+1)\pi x^*}{2l} \right), \quad (\text{B. 2})$$

where l is the half the specimen width and x^* is the distance from the specimen center [100]. In this model, $x^* = 0$ corresponds to the center of the specimen, with positive x^* values going towards one surface and negative x^* values going towards the other surface. Thus, the hydrogen profile throughout the entire specimen can be predicted. Table B.4 shows the hydrogen diffusion profile for penetration depths of 81 to 94 μm for a charging time of 105.685 hours. Notice, Model A and Model B predict a C/C_s of 0.16 at a penetration depth of 86-87 μm for charging

time of 106 hours and a D_{eff} of $5.0 \times 10^{-11} \text{ cm}^2/\text{s}$.

Table B.4: The predicted hydrogen concentrations for penetration depths of 81 to 94 μm for a charging time of 105.685 hours using Model B. A value of $5.0 \times 10^{-11} \text{ cm}^2/\text{s}$ was used for D_{eff} .

$x[\mu\text{m}]$	$x^*[\mu\text{m}]$	C/C_s
81	1269	0.189119416
82	1268	0.183715784
83	1267	0.178427365
84	1266	0.173253063
85	1265	0.168191746
86	1264	0.163242248
87	1263	0.15840337
88	1262	0.153673884
89	1261	0.149052531
90	1260	0.144538025
91	1259	0.140129055
92	1258	0.135824286
93	1257	0.131622359
94	1256	0.127521895

A comparison of the models shown in Table B.5 demonstrates the two models predict similar hydrogen depth profiles for large hydrogen concentrations above C/C_s of 0.15. However, as C/C_s become very small, the two models diverge from each other. Determining which model better predicts C/C_s is outside the scope of this work. However, for this hydrogen diffusion study, Model B was selected since it accounts for diffusion from both specimen flanks. This allows for accurate prediction of the hydrogen profile for conditions in which diffusion distances are larger than the specimen half width, where contributions from both surfaces must be considered.

Table B.5: Comparison of hydrogen penetrations for two concentration levels predicted by Model A and Model B for a charging times of 105.685 hours and D_{eff} of 5.0×10^{-11} cm²/s.

Model	C/C_s	Predicted H Penetration [μm]
Model A	0.15	87.3
Model A	0.001	174.4
Model B	0.15	88-89
Model B	0.001	201.5

B.5 Potential Mechanisms for Side Crack Initiation and Growth

This discussion will evaluate two potential crack paths for the side cracking phenomenon: (1) cracking that initiates relatively uniformly along the specimen side and propagates towards the specimen center, and (2) cracking that initiates at the corners of the main crack and preferentially propagates along the crack flanks with some progression towards the specimen center. Both of these potential crack paths will be evaluated in the context of the H-production and diffusion into the sample. The first condition implies that the higher overpotential for H-production on the specimen surface (as compared to at the crack tip) causes a higher concentration of H to diffuse into the side of the specimen, the net stress on the specimen away from the crack tip would then cause a new crack to form. This is not likely for several reasons. First, the stresses at the specimen surface are much lower than near the crack tip; the stresses at the crack tip can be 3 to 20 times the alloy yield strength [8]. It is unlikely the sides of the specimen experience enough embrittlement to overcome the stress disparity between the specimen surface and the crack tip [29].

Second, the penetration depth of the side cracks is large compared to the diffusion distance of hydrogen adsorbed at the bulk surface. Intergranular cracking along the sides was measured on the fracture surfaces to penetrate between 100 to 1200 μm from the edge of the

specimen. The first order diffusion estimate ($2\sqrt{D_{eff} t}$) predicts hydrogen penetration at C/C_s levels greater than 0.16 up to distances of 87 to 140 μm for D_{eff} values of 5.0×10^{-11} and 1.3×10^{-10} cm^2/s respectively assuming an average charging time of 105.685 hours, the average time to the onset of side cracking [12, 28]. A more detailed model of the hydrogen profile was performed using Equation B.2. Figure B.5 shows the resulting hydrogen profiles for an SEN(T) specimen achieved at test times of 2, 10, 150, 105, and 152 hours (152 hours being the end of the testing protocol). The low concentration level of $C/C_s = 0.001$ was investigated to estimate the penetration depth of hydrogen, yielding depths of 202 and 325 μm from the bold surface for D_{eff} values of 5.00×10^{-11} cm^2/s and 1.30×10^{-10} cm^2/s respectively, well below the observed depth of intergranular cracking measured on the fracture surfaces. While the critical level of H necessary to cause decohesion is not known for the side cracking, it is likely greater than $C/C_s = 0.001$. Thus, hydrogen embrittlement failure would not be expected at these penetration depths. However, the intergranular cracking occurred well beyond these depths, suggesting that another source of hydrogen besides absorption from the bulk surface is contributing to the side cracking.

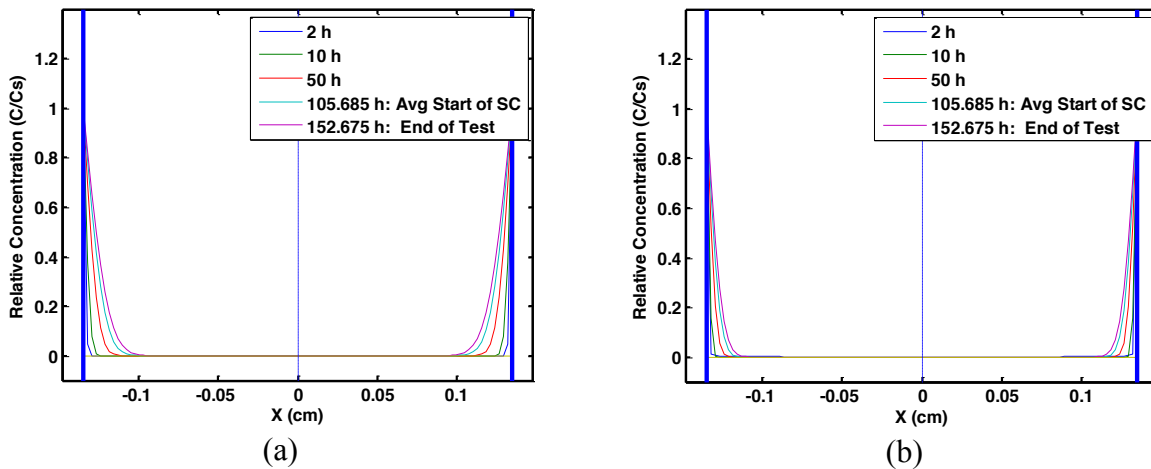


Figure B.5: Hydrogen profiles from Dr. Crank's model for a semi-infinite plate with diffusion from both sides for an SEN(T) specimen 2.70 mm in thickness and (a) D_{eff} of 1.30×10^{-10} cm^2/s and (b) D_{eff} of 5.00×10^{-11} cm^2/s .

Finally, in every instance, the cracking along the sides always occurred at the same height

along the SEN(T) specimen as the initial mode I crack developed earlier in the test; i.e. the initial cracking and the side cracking occurred along the same plane. This suggests that the presence of the crack tip plays some role in the side cracking, possibly serving as an initiation point from which the side cracking begins (Condition 2 above), and then travels down the side of the crack. This is consistent with observations during the test, in which the crack front along either side of the specimen accelerates greatly, rather than a side crack nucleating elsewhere on the specimen and growing to eventually connect to the initial crack front.

A side crack that had initiated along the corners crack front and propagated down either surface of the specimen at enhanced crack growth rates compared to the crack front in the center of the specimen would be reasonable due to the predicted increased C_{H-Diff} associated with a higher overpotential at the surface. Once these smaller side cracks were formed, a higher overpotential would be maintained at the side-crack tip due to the smaller crack dimensions, thus leading to enhanced embrittlement and faster cracking than in the center of the crack tip. The geometry of the side crack can be described by the ratio x^2/G , where x is the penetration depth of the side crack and G is the average opening displacement. Estimates of the penetration depth of the side crack near the point of side cracking onset can be measured from the fracture surface since the cracking was intergranular and final specimen failure was ductile. This yielded initial crack depths ranging from 100 to 400 μm . The short crack depths of the side cracks would lead to large crack mouth opening displacements compared to a mode I crack 1-3 mm in crack length. Therefore, the average crack opening displacement was conservatively assumed to be 2 to 10 times larger than the average opening displacement of a typical 1-3 mm mode I crack. These assumptions yield a range for G of 7 to 33 μm , yielding x^2/G between 0.3 and 2 cm. Previous work on the Allvac Monel K-500 material lot established the relationship between applied potential and C_{H-Diff} as a function of x^2/G and is shown in B.4 [8]. The purple line in B.4 shows the expected C_{H-Diff} values as a function of applied potential for a side crack, while the red dotted line shows the expected C_{H-Diff} concentrations for a typical mode I crack 1-3 mm in length. The side crack experiences roughly 2-3 times higher C_{H-Diff} concentrations than a typical mode I crack. B.4 yields C_{H-Diff} estimates of 17 ppm at the applied potential of -850mV_{SCE} and 28 ppm at -950mV_{SCE} for the side crack geometry.

This C_{H-Diff} can then be used to estimate a stage II crack growth rate using a decohesion

based model that assumes growth rate limitation by H diffusion ahead of the crack tip; details of the assumptions and issues with this analysis are found in previous work [8, 10, 14, 26]. First the stress concentrated H concentration is calculated assuming:

$$C_{H\sigma} = C_{H-Diff} \exp\left(\frac{\sigma_H V_H}{RT}\right), \quad (B.3)$$

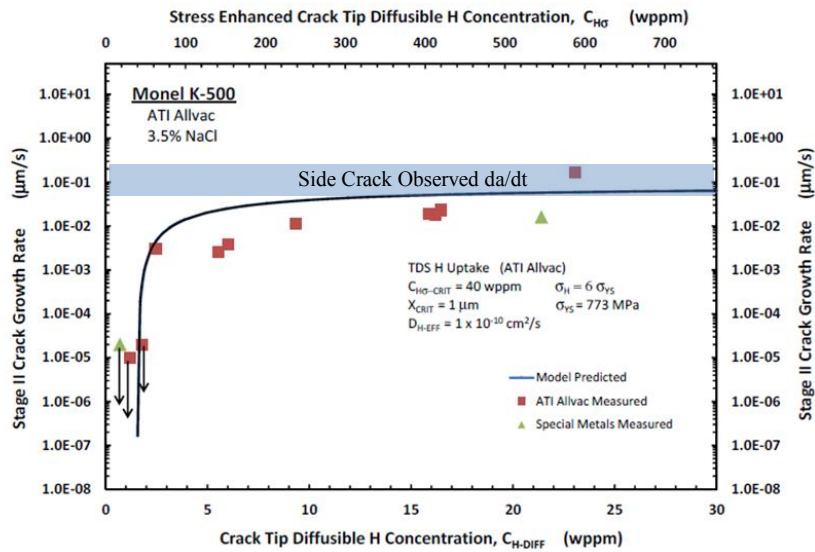
where R is the gas constant, T is temperature, σ_H is the hydrostatic stress located a distance of x_{crit} ahead of the crack tip, and V_H is the partial molar volume of hydrogen in a nickel matrix, $1.73 \text{ cm}^3/\text{mol H}$ [8]. The hydrostatic stress, σ_H is 12 times the yield strength of the alloy in cases of plain strain [28]. Plane stress conditions are present at the specimen surface for the side crack, suggesting σ_H is lower for the side crack than for a normal Mode I crack. However, plane strain is assumed, providing the fastest possible crack growth rates. $C_{H\sigma}$ can then be used to predict da/dt_{II} using

$$\left(\frac{da}{dt}\right)_{II} = \frac{4D_{eff}}{x_{crit}} \left(\text{erf}^{-1}\left(1 - \frac{C_{H\sigma-crit}}{C_{H\sigma}}\right) \right)^2, \quad (B.4)$$

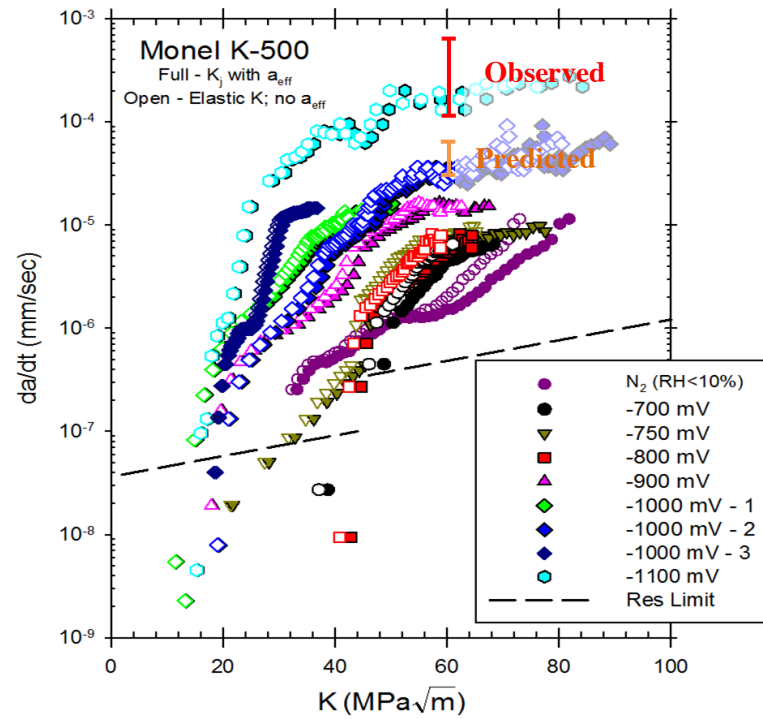
where x_{crit} is critical distance in front of the crack tip where crack advance nucleates, and $C_{H\sigma-crit}$ is the critical concentration of hydrogen necessary to activate decohesion at x_{crit} , assumed to be $1 \mu\text{m}$ [8, 10]. Using the pertinent values shown in Figure B.6(a), the da/dt as a function of C_{H-Diff} was successfully modeled for the Allvac material lot [8]. The expected crack growth from a side crack can be read off the plot in Figure B.6(a) using the C_{H-Diff} calculated for a side crack geometry, yielding crack growth rates between $3.0 \times 10^{-5} \text{ mm/s}$ and $7.0 \times 10^{-5} \text{ mm/s}$ for -850mV_{SCE} and -950mV_{SCE} respectively. Figure B.6(b) shows these crack growth rates (depicted by the orange bracket) are an order of magnitude slower than the da/dt estimates from observed side cracking at various potentials described in section B.3 (depicted by the red bracket), which ranged from $1.1 \times 10^{-4} \text{ mm/s}$ to $5.3 \times 10^{-4} \text{ mm/s}$. Thus, the model predicting crack growth rate due to hydrogen evolution at the shorter crack tip, is lower than the estimated experimental crack growth rate, even with the assumption of plane strain conditions for the side crack.

It remains unclear whether the stress intensity for the side crack is high or lower than at the main crack tip from which the side cracks initiated. Determining the stress intensity for a side crack was outside the scope of this work. The accuracy of this analysis is compromised by

extensive estimations and assumptions; however, the order of magnitude higher observed-estimated growth rates suggests an additional mechanism contributing to the fast side-cracking growth rates.



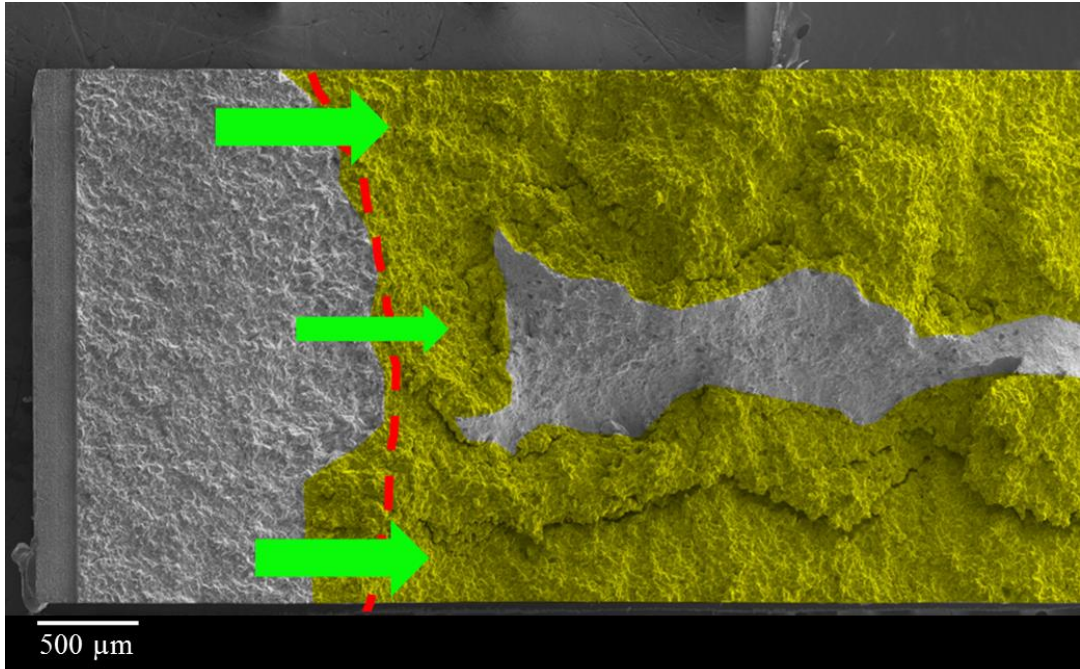
(a)



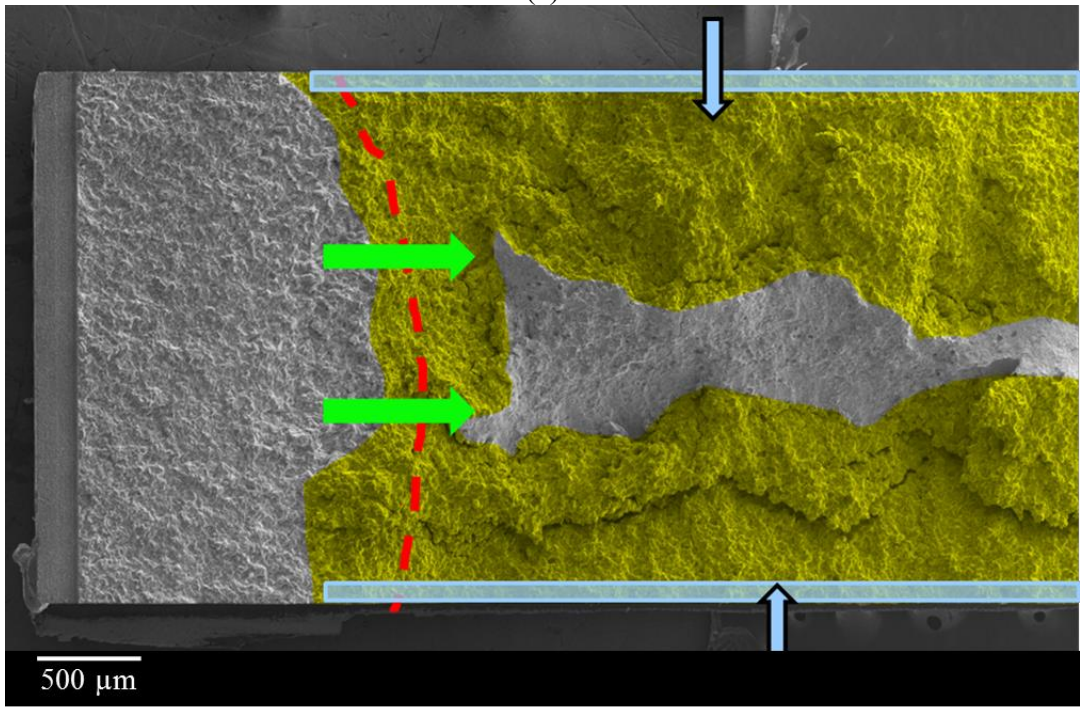
(b)

Figure B.6: (a) Equation B.4 previously fit to C_{H-DIFF} and da/dt_{II} measurements on Allvac material with the estimated side crack growth kinetics shown by the blue rectangle and (b) the predicted range for da/dt using Equation B.4 for a small side crack is shown in the orange bracket while the red bracket shows the observed da/dt for the side cracks. Previously measured crack growth rates on the Allvac material is shown for reference [8].

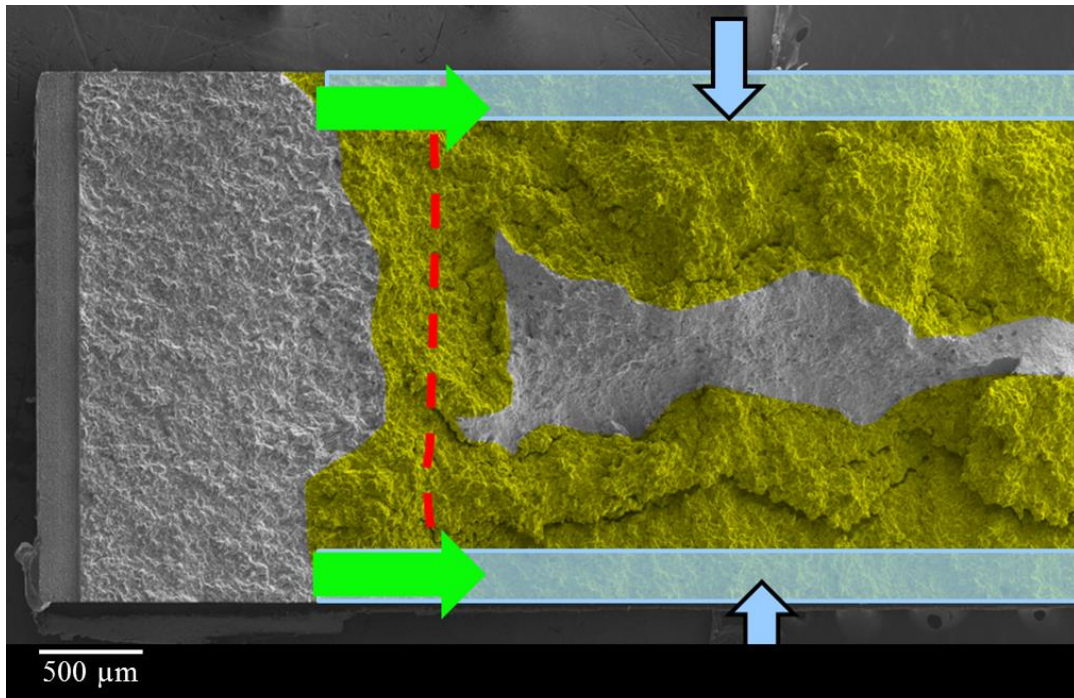
The enhanced crack growth rates associated with chemistry changes due to the shorter side crack geometries may be augmented by bulk charging at the specimen surface that is occurring during the initial portion of the test on the specimen surface. In other words, the charged H would augment the hydrogen produced at the short side-crack tip, leading to enhanced crack growth rates for the side cracking. Such conditions would lead to the following hypothetical sequence to develop the side-cracking morphology. Initially, crack growth is dominated by hydrogen production at the main crack tip and constraint in the center of the specimen, shown in Figure B.7(a). While this is occurring, hydrogen is being produced along the bulk surface away from the crack tip, charging the surface of the specimen, shown in Figure B.7(b). At this stage, the crack growth is similar to that observed in cases where side cracking did not occur and to what is reported in the literature. Eventually, the hydrogen charging along the sides of the specimen (at depths determined by the diffusion modeling in Figure B.5) combined with the more aggressive crack tip chemistry associated with the short side-cracks, leads to more aggressive HEAC along the sides of the crack than at the center of the crack. This occurs despite the increased constraint in the specimen center that gives a higher hydrostatic stress and thus enhanced C_{H_2} . As such, the crack front at either surface out-paces the crack front in the center of the specimen, depicted in Figure B.7(c). At this stage, the more aggressive side crack chemistry couples with redistributed hydrogen from the bulk charging on the specimen surface. The vast majority of crack growth is now occurring along either side of the specimen, with the two crack tips essentially acting independently of each other. The hydrogen in both “crack tip FPZ’s” is supplied simultaneously by the crack tip chemistry associated with the side crack described by the x^2/G crack geometry and by redistributed hydrogen from the bulk charging that has been accruing throughout the test duration, depicted in Figure B.7(d). This expedites the crack growth rate and may lead to the increased crack growth rates on the specimen flanks. Once the two side cracks reach the far end of the specimen, they meet and become one crack again, leading to the intergranular morphology evident at the end of the specimen in Figure B.1.



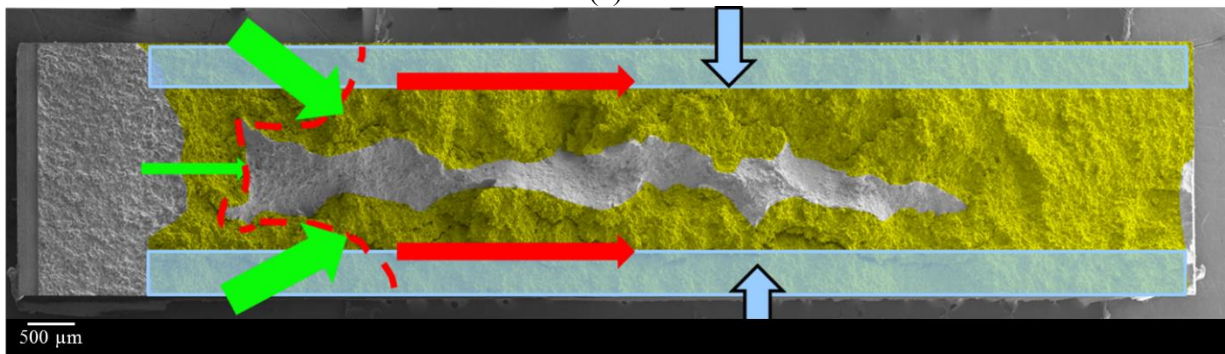
(a)



(b)



(c)



(d)

Figure B.7: Proposed mechanism for the progression from (a) mode (I) crack growth dominated by constraint at the specimen center to (d) side cracking dominated by aggressive crack tip environment at the specimen edges.

This hypothesis is predicated on the fact that lattice hydrogen concentration redistribution can occur over the time-frames relevant to the fracture mechanics tests. That is, the lattice diffusion must be able to migrate to the FPZ of the side crack to enable additional crack growth at such fast crack growth rates. A reasonable test for this hypothesis would be to test a charged SEN(T) specimen under the standard conditions with side masking. If H is charged uniformly through the width of the specimen, this hypothesis would predict that the accelerated cracking would occur for a uniform straight crack front, since the crack growth would no longer be

constrained by the hydrogen diffusion from production sites at the crack tip to the FPZ. As such, a TR1 SEN(T) sample was charged with hydrogen for 95 days at 70°C while cathodically polarized to -1300mV_{SCE} in 0.6M NaCl. The solution was refreshed as necessary to keep the pH of the bulk solution between 6 and 6.4.

The benefit of heating the entire charging environment to 70°C is an increased diffusivity, which can be determined assuming a Fickian Arrhenius temperature dependence:

$$D_{eff}^*(T) = D_{0,eff} \exp\left(-\frac{E_m^{app}}{RT}\right), \quad (B.5)$$

where D_{eff}^* is the effective diffusivity at the temperature, T, $D_{0,eff}$ is a constant, R is the gas constant, and E_m^{app} is the trap-affected activation energy for hydrogen diffusion [12]. E_m^{app} was previously measured twice for aged Monel K-500 to be 38.1 and 41.2 kJ/mol, and for modeling in this project the averaged value of 39.65 kJ/mol was used [12]. With this value and the known D_{eff} values of 5.00×10^{-11} cm²/s and 1.30×10^{-10} cm²/s at room temperature, $D_{0,eff}$ can be solved for and D_{eff}^* is found to be 1.39×10^{-9} cm²/s and 5.35×10^{-10} cm²/s respectively. Hydrogen profile modeling using Dr. Crank's diffusion solution (Equation B.2) shown in Figure B.8 demonstrates the much larger hydrogen concentrations achievable at 70°C than at 20°C .

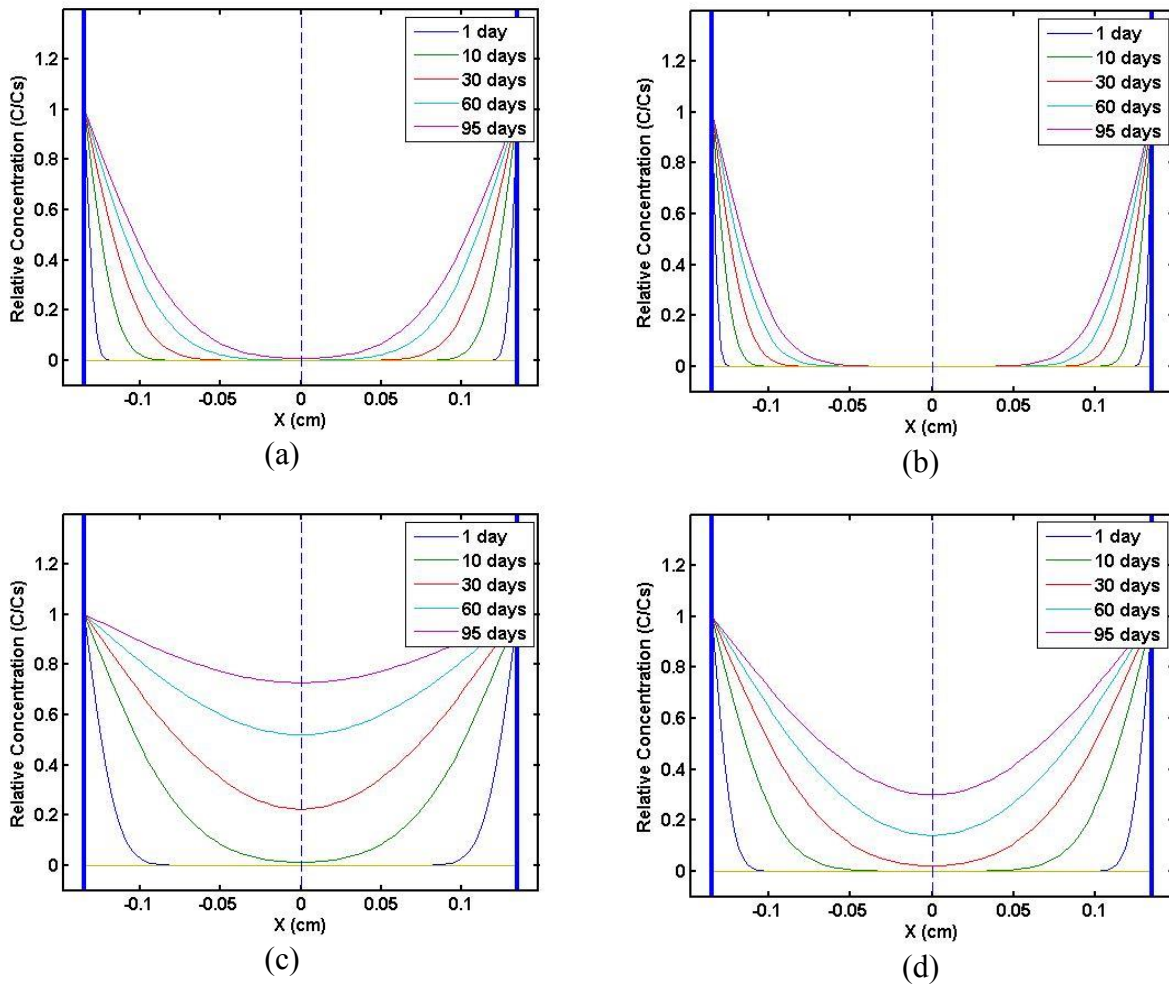


Figure B.8: Hydrogen profile for the charged specimen if it were done at 20°C assuming D_{eff} values of (a) $1.3 \times 10^{-10} \text{ cm}^2/\text{s}$ and (b) $5.0 \times 10^{-11} \text{ cm}^2/\text{s}$ and at 70°C assuming D_{eff}^* values of (c) $1.39 \times 10^{-9} \text{ cm}^2/\text{s}$ and (d) $5.35 \times 10^{-10} \text{ cm}^2/\text{s}$.

Once charged, the specimen was quickly rinsed in deionized water to remove surface salt deposits then painted and tested at $-1000 \text{ mV}_{\text{SCE}}$ as described in sections 2.1-2.4 (testing began within 2 hours after removal from the charging solution, so little outgassing is expected). Testing results are shown in Figure B.9. Measured da/dt_{II} at a K of $60 \text{ MPa}\sqrt{\text{m}}$ are $5.51 \times 10^{-6} \text{ mm/s}$, $1.08 \times 10^{-5} \text{ mm/s}$, and $1.56 \times 10^{-5} \text{ mm/s}$ for the charged TR 1 and uncharged Allvac and TR 2 specimens respectively. Thus, the precharged specimen crack slightly slower than the uncharged specimens, suggesting the increased lattice hydrogen concentration did not affect the crack growth during fracture mechanics testing.

In addition, da/dt_{II} for the charged TR 1 specimen tested at $-1000 \text{ mV}_{\text{SCE}}$, $5.51 \times 10^{-6} \text{ mm/s}$,

was slightly higher than that of an uncharged TR 1 specimen tested at $-950\text{mV}_{\text{SCE}}$, which was given in Section 3.1.2.2 to be $3.44 \times 10^{-6} \text{ mm/s}$. The slight increase in da/dt_{II} observed between the charged TR 1 sample and uncharged TR 1 sample tested at $-950\text{mV}_{\text{SCE}}$ is consistent with the small increase in cathodic applied potential used during the testing of the charged sample; suggesting little to no influence of the charged lattice concentration of H.

These data suggest that redistribution of pre-charged H to the FPZ during the fracture mechanics testing is not sufficient to influence the cracking. This outcome is not fully unexpected as it is not clear why there would be a difference in such redistribution between the masked specimen (no side-cracking) and the unmasked specimens (side-cracking). Specifically, the masked specimen has a 1mm window around the Mode I crack path and this area would be charged similarly as the bold surface of the unmasked specimen; as such, any influence of pre-charging the masked specimen would imply H would have to redistribute from further than 1mm away from the Mode I crack in the unmasked specimen to provide an enhancement that is unique to the unmasked specimen. Redistribution from such long distances during the timeframe of the fracture mechanics test is not reasonable.

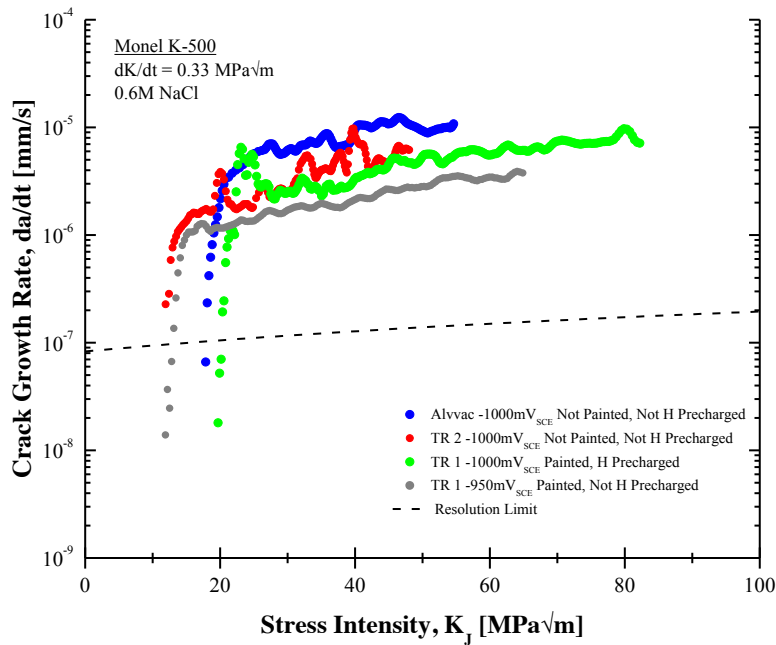


Figure B.9: Fracture mechanics testing da/dt vs K_I results of uncharged Allvac and TR 2 samples and one precharged TR 1 sample at $-1000\text{mV}_{\text{SCE}}$.

B.6 Conclusions

The efforts to understand the accelerated side cracking observed during fracture mechanics testing of several aged Monel K-500 material lots have not illustrated a conclusive mechanism for this behavior. The occurrence of side cracking as well as the side cracking rate appeared to be independent of the applied potential in the $-850\text{mV}_{\text{SCE}}$ to $-1000\text{mV}_{\text{SCE}}$ range. A reasonable hypothesis has been presented to explain the onset of the side cracking behavior in the context of differences in the overpotential for H production between the primary crack tip, the bulk surface, and the short side crack tip geometries. However, experiments on H pre-charged specimens suggest that the redistribution of H to the FPZ during the time-frame of the current fracture mechanics testing is not sufficient to impact the growth rates. Several critical questions remain. First, why the unmasked specimens in previous testing using the same protocol did not exhibit the side-cracking behavior [8]. Second, why the tape/lacquer protection method described in section 2.2 successfully prevented the side cracking from occurring or delayed it long enough to allow for testing protocol completion. This may be related to an influence of a limitation of the bold surface interaction area with the crack tip on the electrochemical conditions; however no such effect is obvious. Despite a lack of conclusive mechanistic understanding of the side-cracking behavior, the uniform crack front observed in all specimens masked according to Section 2.2 and the results presented in Figure B.9 suggest that the masked specimen data used to investigate the metallurgical differences in this study are not compromised by a surface charging effect.